Characterization of the GATE Monte Carlo platform for non-isocentric treatments and patient specific treatment plan verification at MedAustron - Vienna - Austria

Alessio Elia

To cite this version:

Alessio Elia. Characterization of the GATE Monte Carlo platform for non-isocentric treatments and patient specific treatment plan verification at MedAustron - Vienna - Austria. Medical Imaging. Université de Lyon, 2019. English. NNT : 2019LYSEI002 . tel-02283555

HAL Id: tel-02283555

https://tel.archives-ouvertes.fr/tel-02283555

Submitted on 11 Sep 2019

N°d'ordre NNT : 2019LYSEI002

THESE de DOCTORAT DE L'UNIVERSITE DE LYON

opérée au sein de
l'INSA de LYON

Ecole Doctorale N° 160
ELECTRONIQUE, ELECTROTECHNIQUE, AUTOMATIQUE

Spécialité / discipline de doctorat :
Ingénierie pour le vivant

Soutenue publiquement le 08/01/2019, par :

Alessio Elia

Characterization of the GATE Monte Carlo platform for non-isocentric treatments and patient specific treatment plan verification at MedAustron

---

Devant le jury composé de :

Univ. Prof. DI Dr. Dietmar Georg, Medical University of Vienna / AKH Wien	Rapporteur
Univ. Prof. DI Dr. Anders Ahnesjö, Uppsala University	Rapporteur
Dr. Denis Dauvergne, Directeur de Recherche CNRS, LPSC Grenoble	Rapporteur
Dr. Silvia Molinelli, Medical Physicist, CNAO ion beam therapy center	Examinatrice
Dr. Carmen Villagrasa, Cheffe du Laboratoire, IRSN/PSE-STE/SDOS/LDRI	Examinatrice
Dr. David Sarrut, Directeur de Recherche CNRS, CREATIS Lyon	Directeur de thèse
Dr. Loïc Grevillot, Medical Physicist, MedAustron ion beam therapy center	Co-directeur de thèse

L'Institut National des Sciences Appliquées de Lyon

École Doctorale N° 160 : Életronique, Életrotechnique, Automatique
Formation Doctorale : Images Et Systèmes

CREATIS - Centre de REcherche en Acquisition et Traitement de l'Image pour la Santé (UMR5220)

Characterization of the GATE Monte Carlo platform for non-isocentric treatments and patient specific treatment plan verification at MedAustron

Directeur de thèse
Dr. David Sarrut

Co-Directeur de thèse
Dr. Loïc Grevillot

THESE DE DOCTORAT

Alessio Elia

Soutenue le 08/01/2019

To my family

Contents

Abstract

The goal of this PhD is to develop and validate an independent dose calculation method in order to support the intense commissioning work of a Light Ion Beam Therapy (LIBT) facility, and to validate the Treatment Planning System (TPS) dose calculation. The work focuses on proton therapy treatments and is held as a collaboration between the CREATIS laboratory (Lyon, France) and the MedAustron Ion Therapy Center (Wiener Neustadt, Austria).

At MedAustron, in order to exploit a sharp lateral penumbra for the proton beam as well as to improve the accuracy of the TPS dose calculation algorithms, the air gap between the treatment head window and the patient is reduced by moving the patient towards the treatment head. Therefore, non-isocentric treatments have to be accurately taken into consideration during modeling as well as validation phase as moving the target away from the room isocenter may lead to reduced treatment accuracy.

In this study, the parametrization of the proton pencil beam follows the recommendations provided in Grevillot et al. (2011), but including a full nozzle description. Special care is taken to model the pencil beam properties in non-isocentric conditions, including the use of a Range Shifter (RaShi). The characterization of the pencil beam is based solely on fluence profiles measured in air and depth dose profile acquired in water. In addition, the presented model is calibrated in absolute dose based on a newly formalism in dose-area-product presented in Palmans and Vatnitsky (2016). Eventually, a detailed validation is performed in water, for three-dimensional regular-shaped dose distributions. Several parameters commonly exploited in proton dosimetry such as range, distal penumbra, modulation, field sizes and lateral penumbra for proton dosimetry are evaluated for validation purposes.

The pencil beam optics model reached an accuracy within the clinical requirement of 1mm/10% and it is not affected by the complexity of non-isocentric treatments and the use of a RaShi. Ranges are reproduced within 0.2 and 0.35 mm (max deviation) without and with range shifter, respectively. The dose difference in reference conditions is within 0.5%. The 3D dose delivery validation in water was within 1.2% at maximum. The agreement of distal and longitudinal parameters is mostly better than 1 mm.

The obtained results will be used as a reference for the future clinical implementation of the MedAustron independent dose calculation system. As an example of the potential clinical outcome of the presented work, the patient specific quality assurance measurements performed in water have been successfully reproduced within the clinical requirement of 5% accuracy for a few patients.

CHAPTER 1

Introduction

In 2015, about 90.5 million people suffered from cancer [1] and every year, about 14.1 million new cases occur[1] [2]. Cancer causes about 8.8 million deaths which correspond to 15.7% of the human deaths [3]. In children, acute lymphoblastic leukemia and brain tumors are most common[2] and in 2012, about 165,000 children under 15 years of age were diagnosed with cancer [2]. In Austria, about 39,000 people develop cancer every year [4]. Even though men are slightly more affected than women, for both sexes, malignant tumor diseases are the second most common cause of death, preceded by cardiovascular diseases [4]. Under current estimates, two in five people will have cancer at some point in their lifetime [5].

Three main cancer treatment techniques are commonly addressed: surgery, systemic treatment and radiation therapy. The choice upon these three therapies depends on many factors, e.g. the location of the tumor, the stage of the disease and the anamnesis of the patient. Whenever feasible, a complete resection of the tumor results into a curative treatment in most of the cases without considerable damage to the healthy tissues. However, the ability of the malignant cells to metastasize over adjacent sites leads to micro-metastasis which are difficult to detect. Therefore, coadjuvant as well as adjuvant treatments are then necessary to increase the probability of the tumor control. However, systemic treatment and radiotherapy can practically have a negative effect due to non-negligible side effects [6].

New techniques and methods against cancer are constantly under investigations by modern research in order to increase the tumor control probability and to reduce

---

[1] Skin cancer other than melanoma are not considered.

[2] An exception is represented by Africa where non-Hodgkin lymphoma occurs more often compare the brain tumors.

the unavoidable side effects. In this respect, ion therapy played a significant role as a valid alternative since more than 60 years. During this period, remarkable technical improvements as well as clinical outcomes have been achieved in both light[3] and heavy ion beam therapy. In the following, some general considerations are presented as introduction to this manuscript. Unless otherwise stated, the given concepts apply to proton therapy only.

1.1 Considerations for proton therapy

In some extent, proton therapy can be considered as an external beam radiotherapy technique using proton beams. Interest in proton therapy seems to be exponentially increased from 1970 to 2010 [8]. It is commonly stated that proton therapy originates from a Robert Wilson's proposal [9]. Wilson introduces the basic rationale for proton therapy, giving a visionary clinical application of complex physical interactions among particles. In fact, highly conformal treatments of deep-seated tumors rely on the idea that charged particles traveling trough the matter release a maximum of energy at the end of their path (Bragg peak) [10] (more details are available in chapter 2). Despite Wilson's suggestion in the 1946, the first clinical trial is conducted only later, in 1954, when the first patient is treated at the Berkeley Radiation Laboratory [11]. For these pioneeristic treatments, the potentiality of a proton irradiation is still not fully exploited as the energy of the protons is not adjusted in order to generate a Bragg peak at the tumor location.

A few years later, in Uppsala (Sweden), remarkable studies are conducted for the first time [12, 13, 14, 15]. For example in [13] a first use of the spread-out Bragg peak is exploited while in [15], the proton beam is magnetically scanned vertically and horizontally by two sweeping coils with a minimal loss of protons. In 1961, the Harvard Cyclotron Laboratory and the Massachusetts General Hospital establish an important collaboration between physicists and clinicians that improves the treatment technique under several aspects. Thanks to this effective collaboration many important studies are conducted and 9116 patients are treated till 2002, when the cyclotron is shut down [16, 17, 18, 19, 20, 21]. Also Russia starts proton therapy treatments in 1967, in Dubna [22, 23, 24] followed by Japan in 1979 with the first treatments in Chiba [25].

Noteworthy, in all these studies, only accelerators initially built for physics research purposes are exploited as the idea of having a specific center for cancer treatment by protons irradiation was still not an option at that time. According to [26], the first proton therapy center entering in operation is the Center for Proton Therapy in Villigen (Switzerland, 1984) followed by the Clatterbridge Center for Oncology (UK, 1989). The former was equipped by a compact scanning gantry while the latter by a low energy cyclotron in order to treat ocular tumors. Since the 1990, several hospital-based proton therapy facilities start clinical activities worldwide: the Loma

---

[3] In this manuscript, light ion is defined as having an atomic number less than or equal to 10 (neon) [7].

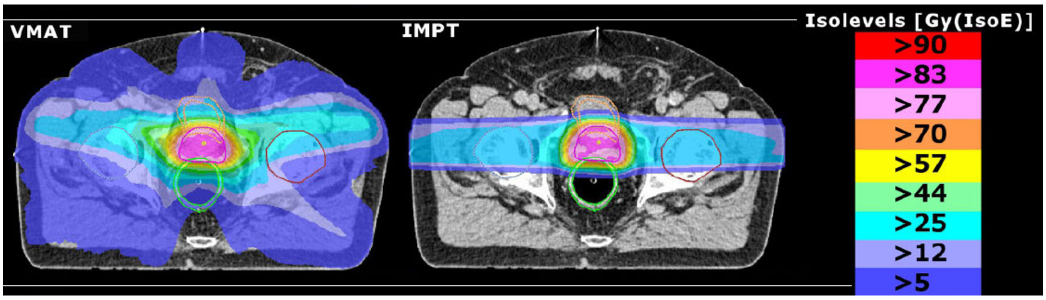

Figure 1.1: example of a comparison between dose distributions obtained with an intensity modulated radiation therapy technique (on the left side) and a proton therapy with active scanning technique (on the right side). Adapted from [29].

Linda University Medical Center in Loma Linda (USA, 1990), the Centre Anoine Lacassage in Nice and the Centre de protonthérapie in Orsay (France, 1991), the Crocker Nuclear Laboratory in San Francisco (USA, 1994) and TRIUMF in Vancouver (Canada, 1995). Many others follows in Germany, Russia, Japan, Italy, China, South Korea, Poland, Czech Republic, Taiwan and Austria. By the end of 2016, a total of 149345 patients have been treated with protons [26].

Over time, cyclotron-based facilities widespread faster than synchrotron-based facilities, or so-called *dual facilities* (more details are available in chapter 3), due mainly to technical difficulties as well as lack of evidence of cost-competitiveness [27]. On the other hand, technological progresses in photon therapy remarkably reduced the adoption of proton therapy. Indeed, advanced techniques such as intensity-modulated photon therapy and volumetric arc therapies [28] well neutralize the superior spatial dose distribution in the patient offered by proton irradiation. However, the relative advantage in sparing normal tissues in proton therapy (see figure 1.1) drastically reduces the risk of radiation-induced secondary cancer [30], especially important in pediatric treatments [31, 32].

With the advancement of irradiation techniques, proton therapy (or light and heavy ion beam therapy in general) resulted to be beneficial for a wide selection of tumors and in some situations can also be used as a supportive therapy that can give an overdose at the end of radiosurgery treatment. Especially suitable are solid non-invasive tumors, typically non-responsive in conventional radiotherapy techniques. Countless clinical and research studies performed worldwide support the rationale of ion therapy in general [33, 34, 35, 36, 37, 38, 39, 40, 41] but it is important to remark that it is not always obvious to address a proton treatment as an optimal choice. When proton beams availability (or cost-competitiveness in other words) comes into play, it is important to take into consideration practical aspects such as the patient's status and/or the patient's needs which might adapt the initially aimed clinical goal. [42, 43, 44, 45].

1.2 Rationale of Monte Carlo applications

Having a superior and advanced technique for cancer treatment such as proton therapy, does not guarantee a successful treatment per se. Unavoidable uncertainties involved in the treatment planning process and in the delivery of the dose are highly responsible of the accuracy and the precision achievable. A significant change in the tumor control probability may be induced by a 7-10% change in dose to the target volume [46]. Therefore, it is essential to assess that the whole curative system[4] is able to deliver a dose to the region of interest within 5% of the prescribed dose [46].

The chain of processes that lead to a successful treatment is generally long and complex. The clinical workflow involves many steps like the patient immobilization and setup, the contour delineation for organs at risk and organs of interest, the diagnostic imaging of the patient and the intra- inter-fractional organ motion, just to cite a few. Each of the steps represents a potential source of error and sometimes, the situation can be even more complex as a single step can be composed by several sub-steps.

As integral part of the clinical workflow, a dose calculation engine must fulfill the accuracy requirements as well. In proton therapy, and in particular in scanned proton therapy, there are basically three classes of dose calculation algorithms [8, 48]: ray casting, pencil beam and Monte Carlo (MC) methods. In general, each of the algorithms used for dose calculation deal with different approximations at different levels. Once an approximation is introduced, it unavoidably leads to uncertainties that must be taken into account. A crucial point in the uncertainties of a dose calculation algorithm is the way how it deals with the tissue heterogeneity of the patient. For example, the ray casting algorithm considers as the smallest element for dose calculation the physical pencil beam and in order to deal with heterogeneity along the field direction it scales the Water Equivalent Depth (WED) of each dose grid calculation point [8, 48]. The modern pencil beam algorithm introduces an improvement of this approach thanks to the sub-spot technique [49]. However, dosimetric uncertainties in the patients may still be possible due for example to marker implants as well as highly heterogeneous media [50]. Nowadays, the pencil beam algorithm entitles the most pragmatic representation of the particle transport in medium [8] and it is clinically used in most of the Treatment Planning Systems (TPSs) exploited for dose calculation. Nevertheless, specific scenarios might lead to lower accuracy of the predicted dose distribution and therefore a higher-accuracy approach is required. At the moment, only MC algorithms are capable to provide a valid alternative to this problem thanks to its non-analytical approach. Despite a higher computational time, a MC calculation can better account for heterogeneity issues of the patient tissue. As a matter of fact, most of the commercial TPSs available nowadays offer alternative MC algorithms for treatment planing (more detailed are presented in chapter 3).

---

[4] It is intended as an entire workflow to which the patient is subjected. It is typically a long chain of processes, starting from the initial evaluation to the medical structure till the final follow-up after treatment.

MC methods applied to proton therapy improve not only the dose calculation accuracy, but also provide useful insights which cannot be obtained otherwise. A deep evaluation of the uncertainties involved in the clinical treatments [51, 52] is a crucial step towards better treatment quality. For instance, a detailed range uncertainties analysis might lead to the reduction of the safety margin applied during planning process and consequently, to lower normal tissue complications [53]. However, even MC methods are affected by unavoidable uncertainties which need to be accounted for. According to [53], typical uncertainties for MC calculations might be either independent of dose calculation, such as patient setup or beam reproducibility, or dependent of dose calculation. With respect to uncertainties dependent of dose calculation, two contributions are mostly addressed [53]: the CT-based patient geometry definitions and the dose algorithm itself. The former involves the scanner calibration as well as the conversion of Hounsfield Unit (HU) into relative stopping power or material composition, while the latter involves mostly the cross-sections uncertainties as well as the implementation of physics models [53].

1.3 Monte Carlo codes in clinical practice

In general, MC methods are exploited by simulation software and toolkit to provide a numerical solution to the problem of the particle transport into the medium. A predefined number of particles are tracked through the patient geometry based on tissue description provided by diagnostic imaging and according to the implemented physics models. General purpose codes like FLUKA [54, 55], Geant4 [56, 57], PHITS [58] and MCNPX [59, 60] are commonly used for dose calculation. In particular, there are also programs which do not necessarily require specific program language skills from the user point of view but serve as interfaces to object oriented toolkit [8]. Remarkably in this respect, are TOPAS [61, 62], GATE [63, 64] and VMCPro [65].

The cited MC codes, can be organized in order to be exploited as MC-based Independent Dose Calculation (IDC) tools [66, 67, 68]. A properly implemented IDC provides useful insights during commissioning work and can support the validation of the TPS [69]. Further, it can help speeding-up all medical physics commissioning work providing data that must be measured otherwise.

Despite their availability and accuracy performances, a full clinical implementation of the cited MC codes is not always feasible in practice, mainly due to their computational time limitation. The reason is also, in some extend, historical as these codes were originally developed for high-energy physics research and therefore not optimized for clinical applications. Only recently, different research groups developed fast multi-purpose Monte Carlo tools for proton therapy [71, 70]. For instance, using multi- and many-core CPU architectures (MCsquare) [70] or GPU calculation (FRED) capabilities [71], in combination with library of pre-computed look-up tables, it is possible to obtain a clinically acceptable compromise between accuracy and calculation time.

An elegant and general guideline for a clinical implementation of a MC code has been presented in [72] but specific issues must be still overcome depending on the type of the chosen MC code and on the type of the beam line used for particle transport. In this respect, modeling the properties of the beam irradiation may still remain a facility-dependent process as presented in detail in chapter 4.

1.4 About this project

In December 2014 an international collaboration between the CREATIS laboratory from the center Leon Berard in Lyon (France) and the MedAustron Ion Therapy Center in Wiener Neustadt (Austria) is started. The collaboration aims at the implementation of the GATE toolkit at the clinical level, according to the MedAustron clinical practice and specifications.

The possibility to establish a clinical workflow based on GATE re-calculation is suggested for the first time in 2011, during a previous PhD project, where a clinical case of a proton treatment was reproduced in GATE for a cyclotron-based facility [73]. In this report, the basic concepts in proton beam therapy (chapter 2) are provided at first. In the third chapter a description of the MedAustron light ion facility is provided with major emphases on the beam delivery system and the TPS. A considerable part of the project was dedicated to the beam modeling of the proton pencil beam, reported in the fourth chapter. In chapter 5, the procedures used at MedAustron for patient treatment verification are described in order to show a direct clinical application of the GATE simulations at MedAustron. The patient treatment verification plans recalculated by GATE represent a first application of GATE as IDC system at MedAustron.

CHAPTER 2

Basic concepts for proton therapy

In this chapter, an introduction to basic physical and biological concepts for proton therapy is given, mostly in comparison to conventional radiation therapy. Sections are oriented to physics, radiobiology and dosimetry, respectively, in order to give to the reader the needed elements for the basic understanding of the presented work.

2.1 Terminology and definitions

Proton therapy uses the most common terminology adopted by the conventional radiation therapy with small but important adaptations. For clarity purposes, we explicitly defined in this report the most used parameters in proton therapy according to the definitions available in the current literature and official reports [8, 7, 74, 75, 76, 77, 78].

2.1.1 Ranges and longitudinal parameters

The term depth-dose profile refers to a dose profile measured along the beam direction. According to the size of the detector compared to the "size" of the beam profile, it is possible to establish two different approaches for measurements. For a so-called *Central Axis Depth-Dose* profile (CAXDD) the depth-dose profile is acquired with a detector smaller than the transverse beam profile. On contrary, an *Integrated Depth-Dose profiles* (IDD) is measured using a large detector along the central axis of the beam. The collected charge is integrated over time.

An important parameter to characterize the depth-dose profiles is the *range*[1],

---

[1] It is sometimes also referred to as "mean range" or "projected range" or "dosimetric range". The "mean

defined as the depth reached by half of the primary protons that are not removed from the beam by nuclear interactions (see section 2.2) [79]. The range of a proton beam (R80) corresponds to the 80% dose level in the distal fall-off of a depth-dose profile and is rather insensitive of the beam energy spread. Different dose levels establish different range meaning. For instance, The *clinical range* (R90) corresponds to the 90% dose level in the distal fall-off of a depth-dose profile. It is also often referred to as “prescribed range” and “depth of penetration” [79]. The term *physical range* (R80) can be addressed to clearly distinguish it from the clinical range [79]. Instead, the term *practical range* (Rp) is defined as the 10% dose level in the distal fall-off of a depth-dose profile. Based on the Rp definition, it is also possible to define the so-called *residual range* (Rres) as:

$$R_{res} = R_p - z \tag{2.1}$$

where z represents the measurement depth.

Another important definition is the so-called *Bragg peak width* which corresponds to the Bragg peak thickness measured at a given dose level [79]. In this report, unless otherwise stated, the Bragg peak width will always refer to the width at the 80% dose level (BPw80). The size of the SOBP defined at the 90% (or also 95%) dose level of the maximum dose it is refereed to as *modulation* (mod90) of a SOBP. In general, the term “distal penumbra” typically refers to the distance between two dose points measured in the distal fall-off of a depth-dose profile. In particular, the distal fall-off between the 80% and 20% dose levels (DP80-20) and between the 90% and 50% dose levels (DP90-50) are frequently used[2]. Finally, the so-called *Treatment Field Length* (TFL) is a parameter defined as the distance between two DP80-20 lengths (2 x DP80-20) proximal to the distal 50% isodose level of the SOBP, and one DP80-20 length (1 x DP80-20) distal to the proximal 90 percent isodose level of the SOBP. Figure 2.1 summarizes the mentioned longitudinal parameters.

2.1.2 Transverse parameters

The term *spot* refers to the primary proton beam fluence in air. The spot size is defined in two transverse directions as the *Full Width at Half Maximum* (FWHM). A transverse-dose profile is a dose profile measured perpendicular to the beam direction while the *field size* is the distance between two dose points measured in the transverse fall-off from each side of the field. Field size at the 90% dose level (FS90) and at the 50% dose level (FS50) are frequently used. The *lateral penumbra* of a transverse-dose profile is the distance between two dose points measured in the transverse fall-off for one side solely. The lateral penumbra between the 80 and 20% dose levels (LP80-20) is a commonly used parameter for transverse profile as well as the 90 and 50% dose levels (LP90-50). The *treatment width* is defined as the distance between two LP80-20 widths (2 x LP80-20) from the 50 percent isodose levels of the transverse-beam

---

range” corresponds to the “average path length”, as defined in ICRU [78].

[2] DP80-20 is also sometimes called “distal dose fall-off (DDF)” [79]

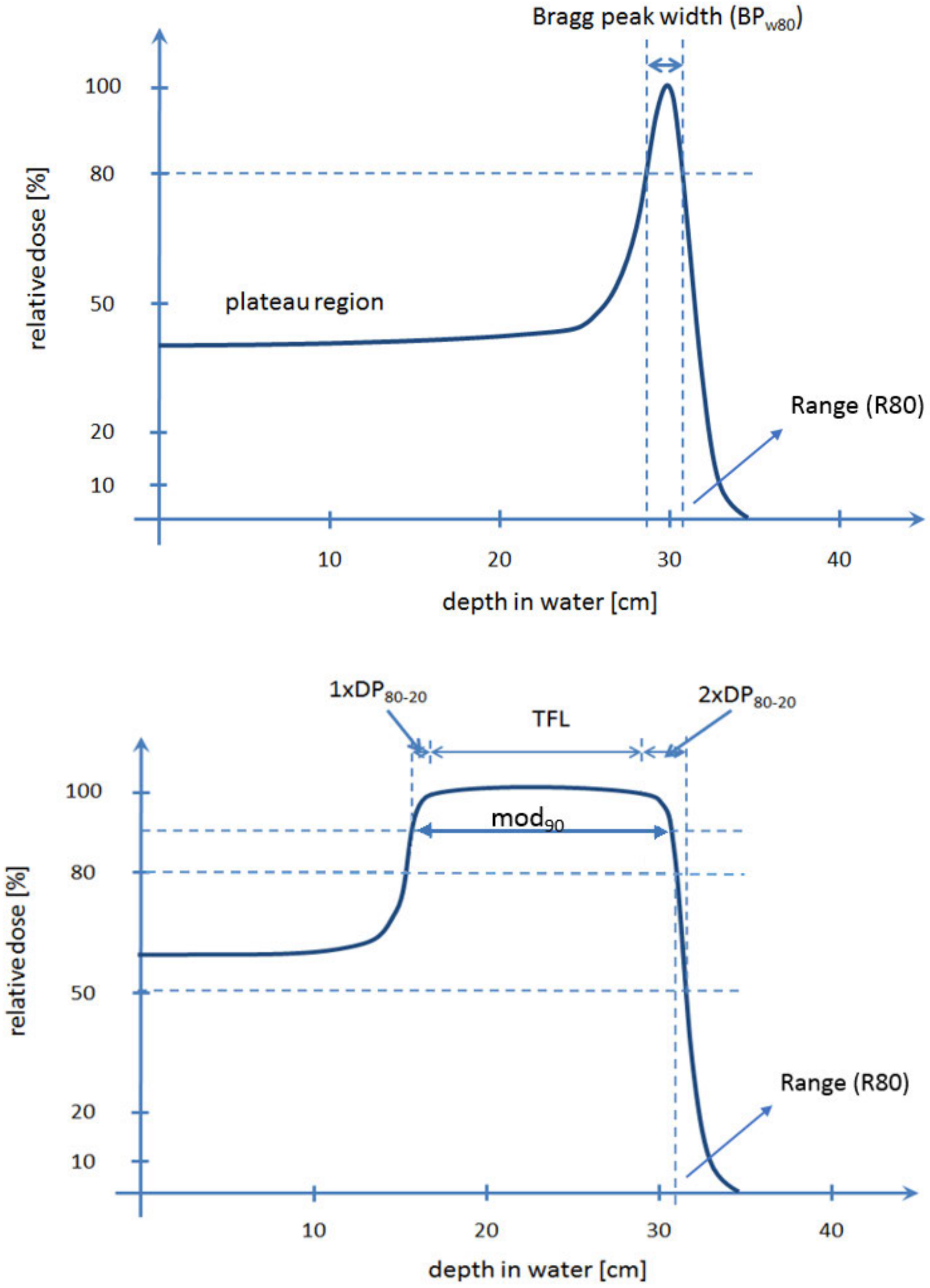

Figure 2.1: depth-dose profile of a pristine 235 MeV proton beam (above) and depth dose profile for a modulated proton beam or SOBP (bottom). For both representations, important longitudinal parameters for proton dosimetry are shown. Adapted from [79].

profile (see figure 2.2). The *field homogeneity* is usually evaluated within a restricted area of the field size, e.g. within 90% of FS90 or the treatment width. The field homogeneity can be calculated using the following formula:

$$H_l = \frac{Max - Min}{Max + Min} \tag{2.2}$$

where Max and Min are respectively the maximum and minimum doses evaluated in the field. *Lateral symmetry* (in percent) is defined as:

$$S_l = \frac{D_1 - D_2}{D_1 + D_2} \tag{2.3}$$

where D_1 and D_2 are the integrated absorbed doses in each half of the field about the central axis in the treatment width. A further parameter is the so-called *Source-to-Axis Distance* (SAD) which corresponds to the distance from the isocenter[3] at which the beam is deviated from the central axis. For horizontal beam lines, it corresponds in theory to the scanning magnets central position relatively to isocenter. For the vertical and gantry beam lines equipped with a 90 degrees bending magnet after the scanning magnet (more details available in chapter 3), both SADs are equal to infinity as the beam is always parallel to the beam axis of propagation. Figure 2.2 summarizes the mentioned transverse parameters.

2.2 Physics of the proton pencil beam

From a classical point of view, the description of the interaction between particles involves two basic parameters: the impact parameter b and the atomic radius a (see figure 2.3-(A)). Roughly, the reciprocal relationship between a and b establishes different interaction types. In particular, are defined [80]:

- *soft collision* for $b >> a$;
- *hard collision* (or *knock-on collision*) for $b \simeq a$;
- *nuclear interaction* for $b << a$.

In case of a *soft collision*, the entire electronic cloud of the target atom is interacting with the Coulomb field of the incident particle, causing excitation or, more rarely, ionization of the target atom [80]. For a *hard collision* a proton interacts with the outer shells of the target atom as well as with inner shell electrons (see figure 2.3-(B)). When inner-shell ionization occurs, this process might be followed by many different processes such as the emission of energetic electrons (δ-ray) as well as the emission of characteristic X-*ray* and a *Auger* electrons [80]. A hard collision with the nuclei of the target atom is also possible (see figure 2.3-(C)). Eventually,

---

[3] The isocenter indicates the reference point of the room around which the beam delivery and PAS systems (see chapter 3) are calibrated.

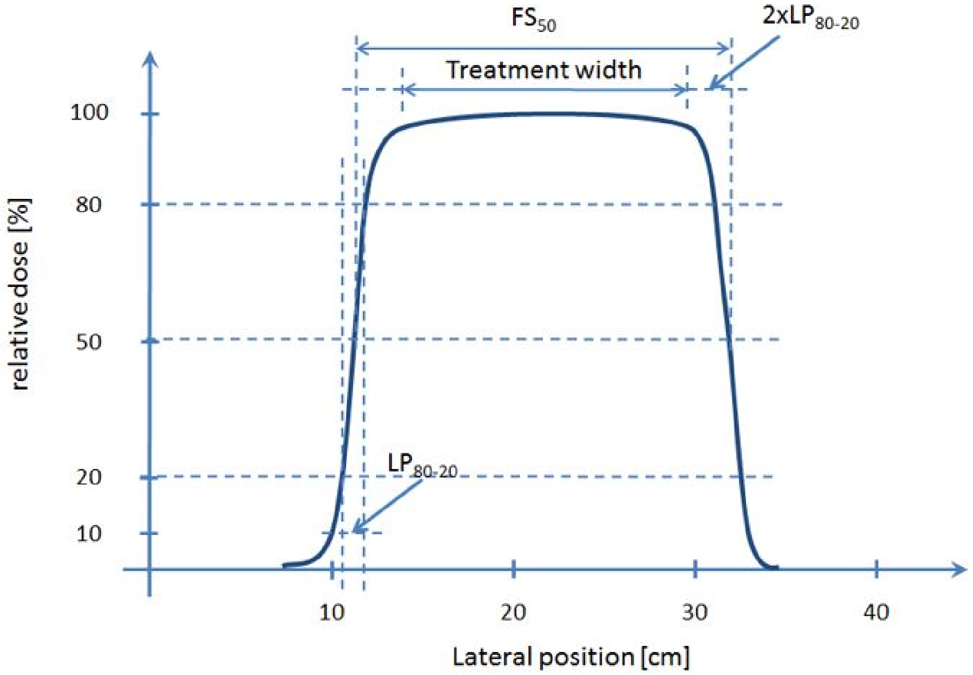

Figure 2.2: example of a transverse-dose profile for a scanned proton beam. The transverse parameters commonly exploited to characterize a scanned proton beam irradiation are emphasized [79].

the condition $b << a$ indicates mostly a *nuclear interaction* i.e. an interaction with the nucleus of the atom[4] (see figure 2.3-(D)). Each type of collision can be classified as *elastic* or *inelastic* collision whether the kinetic energy involved during the process is conserved or not. With respect to the nuclear interactions, it is possible to further discriminate between *non-elastic* and *inelastic* collisions, depending if the final nucleus is the same as the bombarded nucleus [81].

All the peculiarities and important advantages of a proton treatment compared to a photon treatment, deeply rely on physical mechanisms by which a proton interacts with an atom. The table 2.1 provides a summary of the most clinically relevant physical interactions for protons related to their dosimetric manifestation discussed so far [27].

Each of the listed physical processes leads to a specific clinical feature of the pencil beam. To a first-order approximation, protons continuously lose kinetic energy via recurrent inelastic Coulomb interactions with atomic electrons [27]. This approximation, referred to as Continuous Slowing-Down Approximation (CSDA), is fully described by the Bethe-Bloch theory and it is presented in section 2.2.1. On

---

[4] These are the cases where the center-of-mass kinetic energy overcomes the Coulomb potential repulsion.

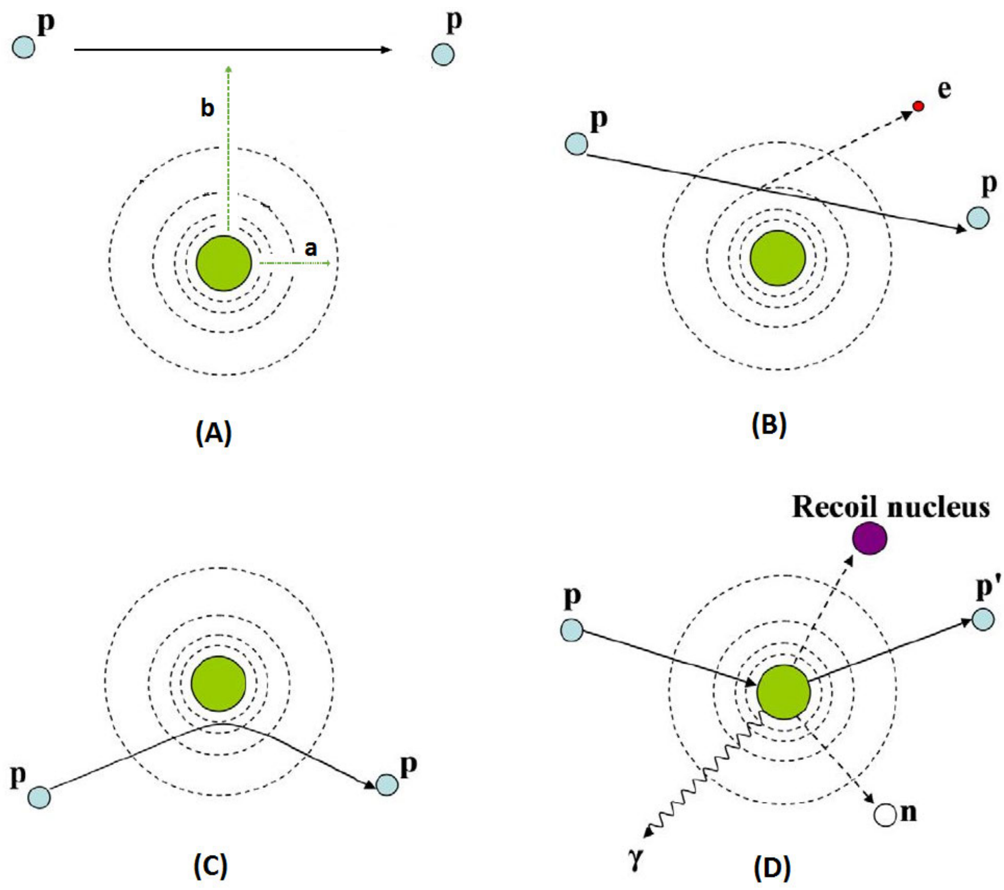

Figure 2.3: illustration of proton interaction processes according to the classical interpretation: (A) representation of a soft collision between an incident proton and target atom where the impact parameter b and the classical atomic radius a are displayed, (B) energy loss via inelastic Coulomb interactions for a hard collision, (C) deflection of proton trajectory by repulsive Coulomb elastic scattering with nucleus (hard collision), (D) removal of primary proton and creation of secondary particles via non-elastic nuclear interaction (p: proton, e: electron, n: neutron, γ: gamma rays). Adapted from [27].

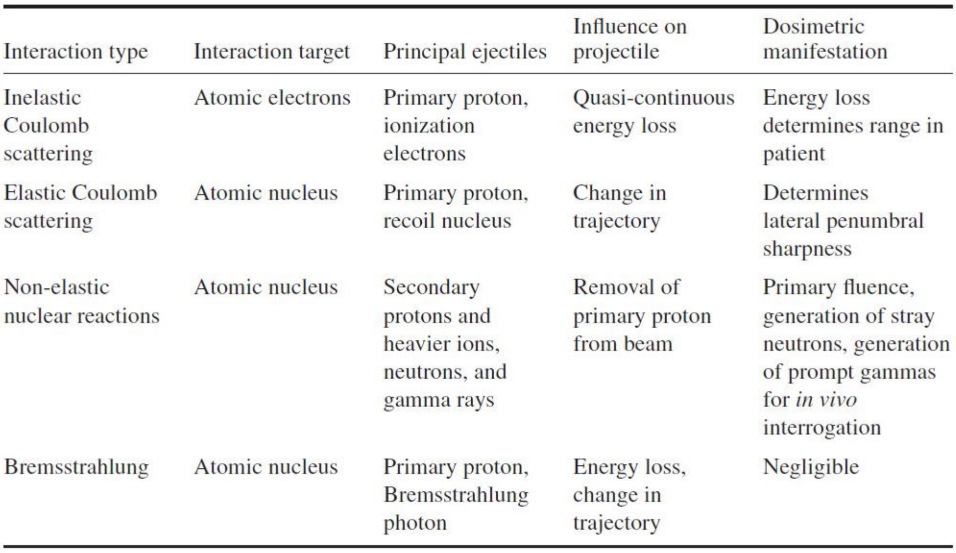

Interaction type	Interaction target	Principal ejectiles	Influence on projectile	Dosimetric manifestation
Inelastic Coulomb scattering	Atomic electrons	Primary proton, ionization electrons	Quasi-continuous energy loss	Energy loss determines range in patient
Elastic Coulomb scattering	Atomic nucleus	Primary proton, recoil nucleus	Change in trajectory	Determines lateral penumbral sharpness
Non-elastic nuclear reactions	Atomic nucleus	Secondary protons and heavier ions, neutrons, and gamma rays	Removal of primary proton from beam	Primary fluence, generation of stray neutrons, generation of prompt gammas for *in vivo* interrogation
Bremsstrahlung	Atomic nucleus	Primary proton, Bremsstrahlung photon	Energy loss, change in trajectory	Negligible

Table 2.1: list of most significant proton interactions related to specific dosimetric manifestation [27].

contrary, the elastic collision with the nuclei[5] does not exhibit a significant role in the energy lost by the incident protons. However, nuclear elastic collisions have a crucial effect on the propagation of the pencil beam in terms of lateral spread (see section 2.2.2) as well as on the net primary fluence of the pencil beam, although in a less relevant way (see section 2.2.3). Non-elastic nuclear interactions are usually less frequent for protons at therapeutic energies as the cross section shows a maximum around 10-50 MeV [73, 81]. Nevertheless, the probability that a primary proton incurs a nuclear interaction shows a strictly increasing monotonic trend with the beam energy[6] (see figure 2.4).

2.2.1 Characterization of the energy loss

The energy loss rate of charged particles, is defined as the ratio between dE and dx, where E is the mean energy loss and x is the depth. The first physically complete theory to describe the so-called *linear stopping power* is attributed to Bohr in 1913 [82]. It is based on the classical approach, exploiting the impact parameter and the momentum impulse of a stationary unbound electron [27]. It is frequently more convenient to express the energy loss rate in terms of the *mass stopping power*, measured in $[\mathrm{MeV} \cdot \mathrm{cm}^2/\mathrm{g}]$:

$$\frac{S}{\rho} = -\frac{1}{\rho}\left(\frac{dE}{dx}\right) \tag{2.4}$$

---

[5] This term is still referring to a hard collision i.e. a scattering process between the incident proton and the target nuclei.

[6] This would not be the case for a thin target where the increasing trend will depend on the range.

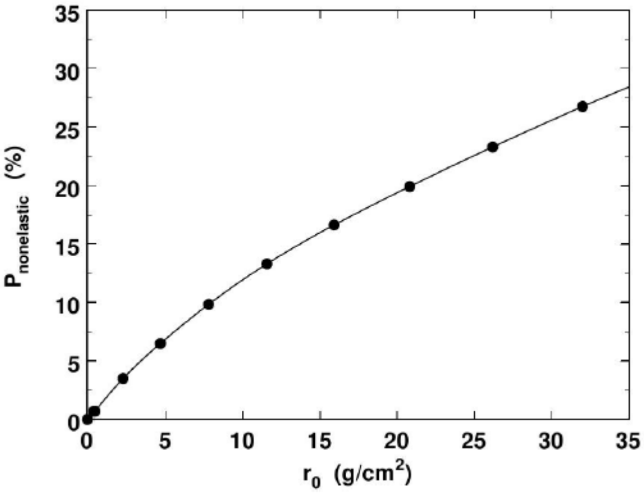

Figure 2.4: probability of non-elastic nuclear interaction as a function of the range [81].

Typically, the mass collision stopping power can be written as sum of three main contributions:

$$\frac{S}{\rho} = -\frac{1}{\rho}\left[\left(\frac{dE}{dx}\right)_{el} + \left(\frac{dE}{dx}\right)_{nuc} + \left(\frac{dE}{dx}\right)_{rad}\right] \tag{2.5}$$

where the term $\left(\frac{dE}{dx}\right)_{el}$ indicates the loss per unit distance due to electromagnetic interactions of the incident charged particle with the electrons of the target (electronic contribution), the term $\left(\frac{dE}{dx}\right)_{nuc}$ corresponds to the loss due to the elastic interactions with the target nuclei (nuclear contribution) and the term $\left(\frac{dE}{dx}\right)_{rad}$ the energy loss due to radiative phenomena (radiative contribution). For protons, the electronic stopping power is the predominant contribution (see figure 2.5). The contribution of the nuclear stopping power becomes important for heavier particles than protons, depending on the incident energy[7]. Radiative energy loss can be neglected for clinical energies where its contribution is even lower than elastic nuclear interactions.

An accurate formula describing the electronic stopping power and accounting for quantum mechanical effects, is attributed to Bethe [84] and Bloch [85]:

$$\left(-\frac{dE}{dx}\right)_{el} = 2\pi r_e^2 m_e c^2 N_A \rho \frac{Z}{A}\frac{z^2}{\beta^2}\left[\ln\left(\frac{2m_e\gamma^2 v^2 W_{max}}{I^2}\right) - 2\beta^2 - 2\frac{C}{Z} - \delta\right] \tag{2.6}$$

where N_A is the Avogadro's number, r_e is the classical electron radius, m_e is the mass of an electron, z is the charge of the projectile, Z is the atomic number of

---

[7] It is the relative speed between the speed of the incident particle and the speed of orbital electrons in the target which establish the importance of the loss due to electromagnetic interaction with the nuclei.

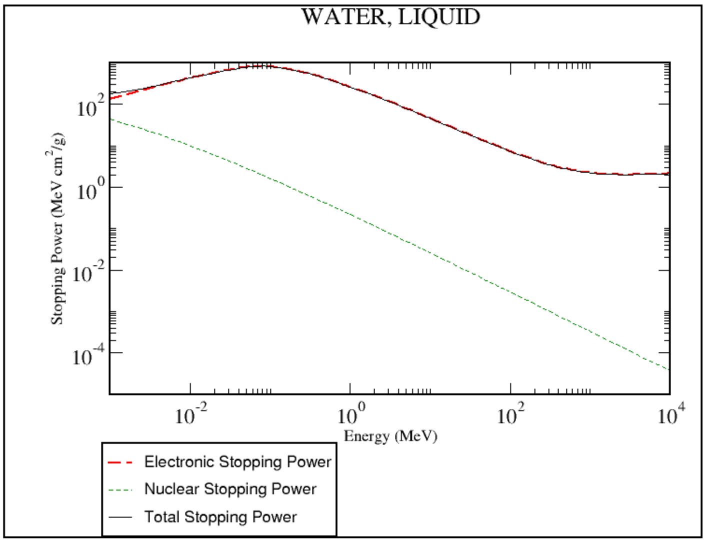

Figure 2.5: total stopping power for protons as a function of protons energy evaluated in water [83].

the absorbing material, A is the atomic weight of the absorbing material and I is the mean excitation potential of the absorbing material. Equation 2.6 revels that the absorber material strongly influences the energy loss rate by the mass density contribution. The strong dependency on the material density ρ justifies the more practical use of the mass stopping power, already introduced in the equation 2.4. In case of compound materials, the *additivity rule* (or Bragg theory) is typically applied. Formally:

$$a = \frac{k}{u} \sum_i \omega_i \frac{Z_i}{A_i} \tag{2.7}$$

where Z_i and A_i represent the atomic and the mass number, respectively, of the i-th element, ω_i a weighting factor, u the atomic mass unit and k is a constant defined as the following:

$$k = \frac{4\pi e^4}{m_e c^2} \tag{2.8}$$

In the formula 2.6 are expressed also two corrections terms[8]: δ which represents the *density correction* arising from the shielding of remote electrons by close electrons which typically results in a reduction of energy loss at higher energies, and the term $2C/Z$ which represent the *shell correction*, important only for low energies where the particle velocity is near the velocity of the atomic electrons [27]. The term W_{max} expresses the maximum energy transferred in a single impact or knock-on impact and is given by:

---

[8] The correction terms are typically negligible at therapeutic energies.

$$W_{max} = \frac{2m_e c^2 \gamma^2 \beta^2}{1 + (\frac{m_e}{M})^2 + \frac{2m_e}{M}\sqrt{1+\gamma^2\beta^2}} \tag{2.9}$$

where, in the limit $M \gg m_e$ can be written:

$$W_{max} \overset{M \gg m_e}{\longrightarrow} 2m_e c^2 \gamma^2 \beta^2 \tag{2.10}$$

It is remarkable to observe in the equation 2.6 how the projectile's characteristic govern its energy loss rate [27]. In fact, the energy loss is proportional to the inverse square of its velocity as well as the square of the ion charge while there is no dependence of projectile's mass [27]. Down to very low energies it is necessary to replace the z term in the formula 2.6 by the effective charge z^*. The z^* term takes into consideration the mean redistribution of the charge and it depends on the energy of the incident particle. It increases with the increase of the incident particle speed in water according to Barkas's formula [86, 87]:

$$z^* = z(1 - \exp[-125\beta z^{-2/3}]) \tag{2.11}$$

Overall, the density of the distribution of the ionization induced by a light ion shows a initial *plateau* at the entrance followed by a sharp increase (due to β^2 decrease) to then rapidly decrease to zero according to equation 2.11.

Another remarkable observation is that the I value can be extracted from penetration depth measurements. Even though the I value has a non-negligible impact, e.g. on particle range calculations, which varies in the millimeter range for different recommended values, it is not well established for all materials. For water, different values are stated in literature ranging from 75 eV to 80.8 eV [78].

The primary protons travel through the medium till they completely neutralize at the end of their path. The final range depends only on the initial energy and on the average energy loss rate in the medium. Therefore, it is possible to express the mean path of a charged particle in the matter by the following approximation:

$$R(E_0) = \int_0^{E_0} \left(\frac{dE}{dx}\right)^{-1} dE \tag{2.12}$$

Statistical fluctuations in the energy loss for every incident particles imply a *spread* in the particles range. This phenomenon is responsible of the so-called *range straggling*, which causes the widening of the Bragg peak depending on the depth (see figure 2.6). Depending on the ion species, the range straggling changes approximately like the inverse of the mass square root (in the tissue it is about 1% of the mean proton range while only 0.3% in case of carbon ions [88]) which also explains why at the same penetration depth, heavier ions show a narrowed Bragg peak.

2.2.2 Characterization of the beam spreading

From a classical perspective, a proton passing close to an atomic nucleus can deflect its original trajectory due to elastic Coulomb interaction. In clinical practice, the

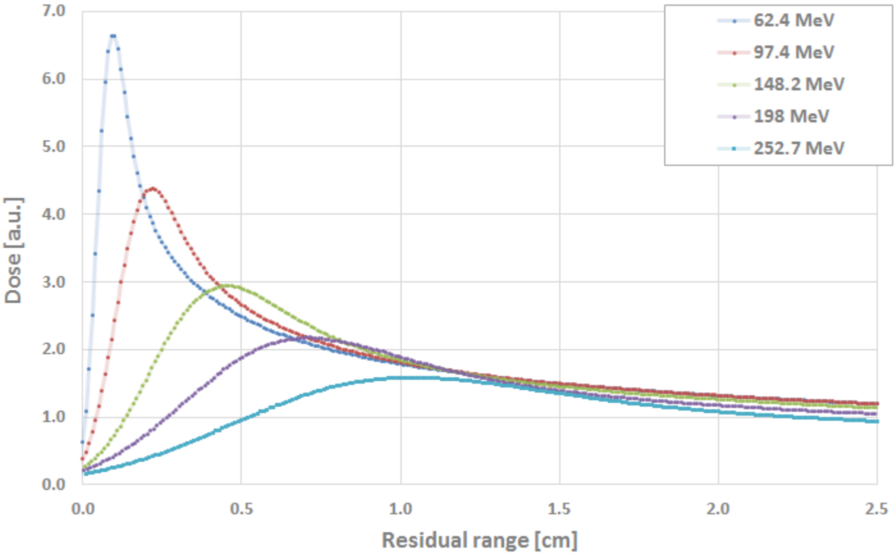

Figure 2.6: example of the range straggling for protons. Energy deposition for five representative clinical energies are calculated in water by GATE/Geant4 [56, 57, 63, 64] and plotted as a function of the residual range (see equation 2.1). It is remarkable that the widening of the Bragg peak width increases due to the range straggling phenomena and the maximum dose is reducing according to the formula 2.16 for a fix fluence.

elastic Coulomb scattering does not remarkably contribute to the energy loss which is typically within 0.1% of the total energy loss [89]. However, this process is clinically very important as it characterizes the lateral beam spread. If the number of Coulomb scattering increases, e.g. the target material is thick enough, it is convenient to consider the mean scattering angle resulting from many single scattering collisions. Indeed, according to Molière theory [90], the *Multiple Coulomb Scattering* (MCS) can be characterized as a consequence of several events of scattering with a deflection from the incident direction due to small highly probable angles. If the probability of having high deviations is neglected, the distribution due to the scattering of small angles (less than 10°) is known to have a nearly Gaussian shape [91] with a single scattering tail (*core* region [92]). Different formalism are available in literature to characterize the standard deviation of the core distribution [91]. A common definition is a later development of the Highland's equation originally stated in [93]:

$$\sigma_\theta[\text{rad}] = z\frac{14.1[\text{MeV}]}{p\beta c}\sqrt{\frac{\Delta x}{L_{rad}}}\left[1+\frac{1}{9}\log_{10}\left(\frac{\Delta x}{L_{rad}}\right)\right] \tag{2.13}$$

where z is the charge, L_{rad} is the so-called radiation length[9] of the target material and Δx is the thickness of the absorber material. Large angle single scattering

---

[9] Defined as the distance in which the electron energy is reduced by a factor 1/e due to radiative loss.

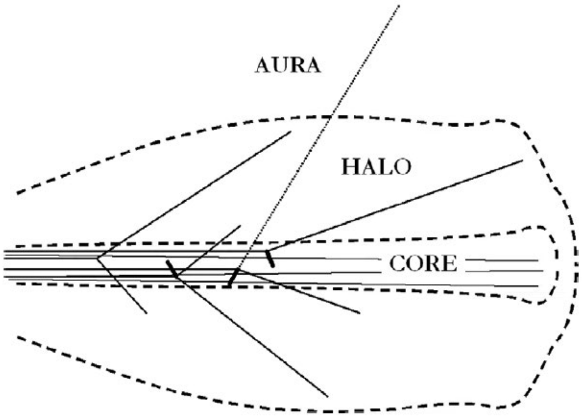

Figure 2.7: representation of the dose regions for a proton pencil beam proposed in [92].

events, although rare, cause distortion of a single tail Gaussian distribution, characterizing the outer envelop of the core, so-called *halo* [92] (see figure 2.7). In order to take into account this effect it is possible to exploit the Gauss-Rutherford approximation to correct the central Gaussian part [71] or trying to describe the beam profile as sum of two (or more) Gaussian contributions [49, 94]:

$$F(r) = \frac{(1-\omega_1)}{2\pi\sigma_1^2}\exp\left(\frac{-r^2}{2\sigma_1^2}\right) + \frac{\omega_2}{2\pi\sigma_2^2}\exp\left(\frac{-r^2}{2\sigma_2^2}\right) + ... + \frac{\omega_n}{2\pi\sigma_n^2}\exp\left(\frac{-r^2}{2\sigma_n^2}\right) \quad (2.14)$$

where r is the radial distance from the central beam axis and $\omega_i \in [0,1]$ represents a weighting factor. It is difficult to identify a specific contribution to the halo dose region as its characterization depends upon electromagnetic elastic as well as nuclear elastic, nuclear inelastic and non-elastic scattering events [92]. The halo radius is proved to be about one-third of the beam range [92] and even though it is a low dose contribution spread over a large area, it may still lead to significant errors in dose calculation (these aspects will be described in more detail in chapter 4).

With respect to the lateral spread briefly described in section 2.2.2, equation 2.13 provides a quick justification concerning three remarkable aspects:

- the scattering angle increases significantly with the depth;
- low energetic beams scatter more than high energy beams;
- heavier ions scatter less than lighter ions.

In figure 2.8 are illustrated the cited behaviors.

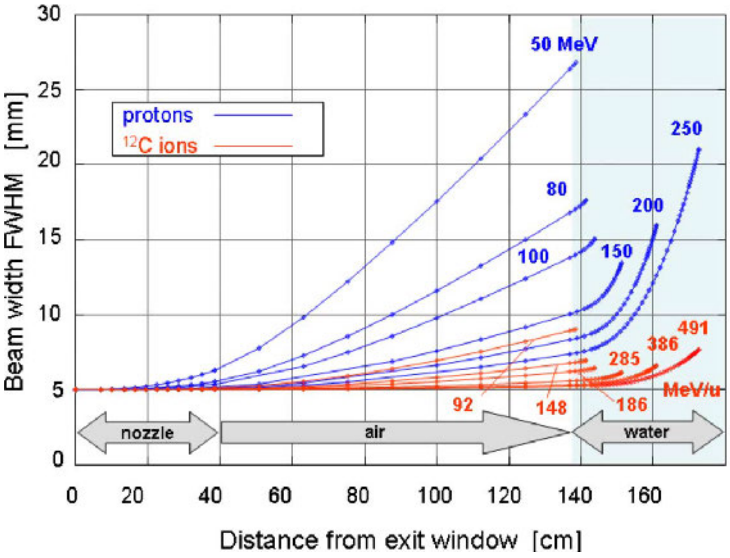

Figure 2.8: simulation of a proton and a carbon ion beam at different energies and through different materials. The simulation is initialized for a fixed FWHM at the source level and it shows the different lateral beam spread behavior as a function of the depth [95].

2.2.3 Dosimetric influence of nuclear effects

To better understand how dosimetry is affected by physical mechanisms it is possible to consider the following definition:

$$D = \sum_i \int_E \Phi_i(E,x)(S_i(E)/\rho)dE \tag{2.15}$$

The term $\Phi_i(E,x)$ in the equation 2.15 represents the fluence of any charged particles of species i for a mono-energetic beam imprinting on a material of density ρ. The equation 2.15 is valid in charged-particle-equilibrium (CPE) conditions and it links the energy lost in the medium by an ensemble of incident charged particles to the absorbed dose by means of the mass stopping power i.e. (mostly) inelastic Coulomb collisions. The fluence $\Phi(E,x)$ is characterized by nuclear reactions which affect the initial fluence, according to:

$$\Phi(E,x) = \Phi_0 \exp[-N\sigma_t(E)\Delta x] \tag{2.16}$$

where Φ_0 is the initial fluence, $\sigma_t(E)$ is the total removal cross section for nuclear reactions and N is the atomic density of the considered material of thickness Δx. The entire IDD is affected by this process as the primary protons are removed from the Bragg peak and the energy is rather displaced in the plateau of the core or transferred to the halo region. In water, the process leads to the production of the emission

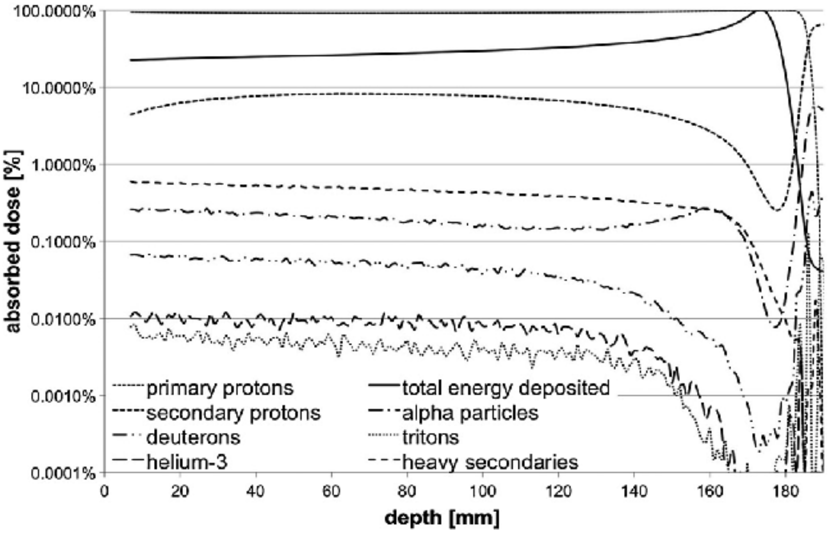

Figure 2.9: IDD for a proton beam of 160 MeV in water. The primary protons, together with the secondaries protons, the alpha particles and the heavy secondaries (A>4) account for the largest contribution on the deposited dose (>99.9%). The remaining dose is shared between deuteron, helium-3 and triton [96].

of secondary particles such as protons (which represent the biggest contribution, up to 10% depending on the energy [96]), deuterons, tritons, alpha particles or heavier ions (see figure 2.9). The secondary particles are mostly forward emitted respect the direction of the primaries which cause the so-called *build-up* effect in the plateau region [96]. Noteworthy, nuclear interactions within the patient are responsible of the production of neutral particles (mostly neutrons) which characterize the *aura* region of the dose distribution (see figure 2.7). Nuclear interaction with the passive elements as well as typical treatment head components, presented in chapter 3, also contributes to characterization of the aura region which therefore may vary depending on the treatment head design.

2.2.4 Beam quality and LET

For protons, the residual range can be used as a beam quality index, according to TRS-398 [77] and ICRU-78 [75] even though this may not be sufficient to correlate fully with spectra information [7]. From a physics point of view, the beam quality index is used in reference dosimetry protocols (see section 2.4). From a biological point of view, the beam quality (or radiation quality) is related to the effectiveness of an irradiation assessed in terms of a wanted effect. The reasons why different radiation qualities may obtain different responses by the tissue rely on the concept of the *ionization density* [97]. The ionization track of different incident radiations (see figure 2.10) changes depending on the quality of the radiation itself. The quantity

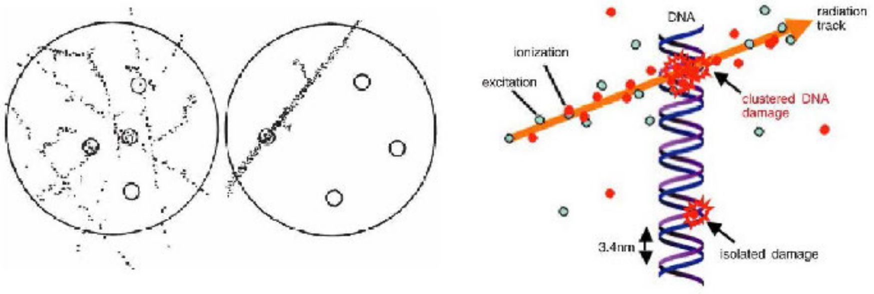

Figure 2.10: on the left, ionization density tracks from a low-LET (a-left) particles and a high-LET particles (b-left). On the right, the ionization density track compared to a DNA chain [98].

Linear Energy Transfer (LET) characterizes this idea. The LET is often expressed in [MeV/mm] (or keV/μm) and it is defined as:

$$L_{\Delta} = \left(\frac{dE}{dl}\right)_{\Delta} \tag{2.17}$$

where dE is the mean energy loss due to collisions with energy transfer less than some specified value Δ and dl is the distance traversed by the particle. In other words, LET is an expression of the so-called *restricted stopping power* i.e. the energy locally imparted by collisions from a charged particle among the path without considering the secondary electrons with energy (expressed in eV) bigger than Δ. Practically, equation 2.17 does not differ from equation 2.6. On the other hand, the dependency on the terms z^2 explains the connection between the amount of the ionization along the track and the LET value for a particular radiation quality. The table 2.2 reports some LET values for different incident charged particles at different depth and it numerically describes this concept. For instance, looking at table 2.2 it is possible to notice LET values less than 15 keV/μm for carbon ions at depth of about 15 cm in water. On the other hand, looking at the last 30 mm of the path in water, the LET is increasing up to 112 keV/μm. The reason why a LET value higher than 20 keV/μm can be so effective in terms of microbiological damage is related to the mean energy deposited to the tissue (about 100-200 eV) within a volume comparable to the size of a strand of human DNA (about 2.5 nm in diameter) which causes about 4-5 ionizations (see figure 2.10) [99]. On the other hand, increasing too much the ionization per unit length does not necessarily increase the effectiveness of the radiation damage. This is the case of the region above 150 KeV/μm where the ratio dRBE/dLET becomes negative (see figure 2.12), resulting in the so-called *overkill.*

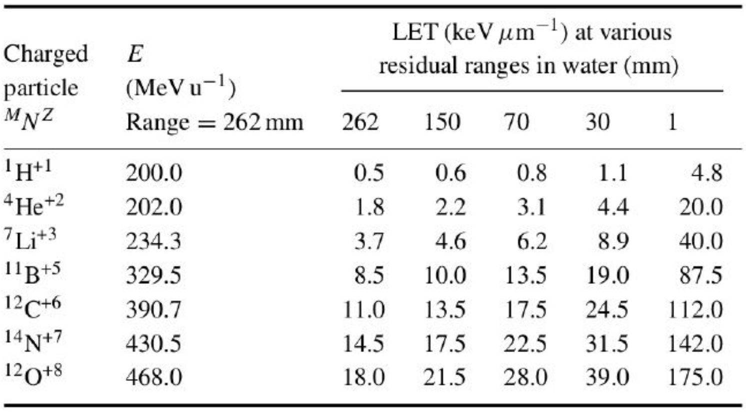

Charged particle $^{M}N^{Z}$	E (MeV u^{-1}) Range = 262 mm	LET (keV μm^{-1}) at various residual ranges in water (mm)				
		262	150	70	30	1
$^{1}H^{+1}$	200.0	0.5	0.6	0.8	1.1	4.8
$^{4}He^{+2}$	202.0	1.8	2.2	3.1	4.4	20.0
$^{7}Li^{+3}$	234.3	3.7	4.6	6.2	8.9	40.0
$^{11}B^{+5}$	329.5	8.5	10.0	13.5	19.0	87.5
$^{12}C^{+6}$	390.7	11.0	13.5	17.5	24.5	112.0
$^{14}N^{+7}$	430.5	14.5	17.5	22.5	31.5	142.0
$^{12}O^{+8}$	468.0	18.0	21.5	28.0	39.0	175.0

Table 2.2: some LET values in function of the depth at different energies for 7 nuclear species [99].

2.3 Radiobiological aspects

A radiation therapy treatment aims to the death[10] of the tumor cells which can be induced if the DNA incurs enough damages. As the DNA molecule is crucial for the cell survival, a complex repair mechanism is in place. The cell repair capability can be expressed in terms of the ratio between the α coefficient and the β coefficient which appear in the following linear-quadratic expression [98]:

$$F(d) = \exp[-\alpha d - \beta d^2] \tag{2.18}$$

The formula 2.18 expresses the fraction of the surviving cells after an irradiation of a given dose d and it links the delivered dose to the observed biological effect. Often, no specific information on the absolute values of α and β for the tissue under consideration is available. However, the sensitivity to the radiation of the tissue under consideration can be described by the α/β ratio [97]. By mean of the α/β ratio, the same clinical effect as with 2 Gy per fraction, considered as the "reference" scheme fractionation, can be retrieved for a non-conventional fractionation [97]. A weighting factor, defined from the ratio between the test fractionation scheme d' and the "reference" fractionation scheme d, can be derived from the following equation:

$$D[1 + d/(\alpha/\beta)] = D'[1 + d'/(\alpha/\beta)] \tag{2.19}$$

where D and D' are the total doses in the two fractionation scheme, respectively [97]. In the absence of more specific information, common values considered for the α/β ratio are 10 and 3 Gy for early and late responding tissues, respectively [97]. The importance of introducing a fractionation scheme is demonstrated for radiation

---

[10] Intended also as clonogenic death.

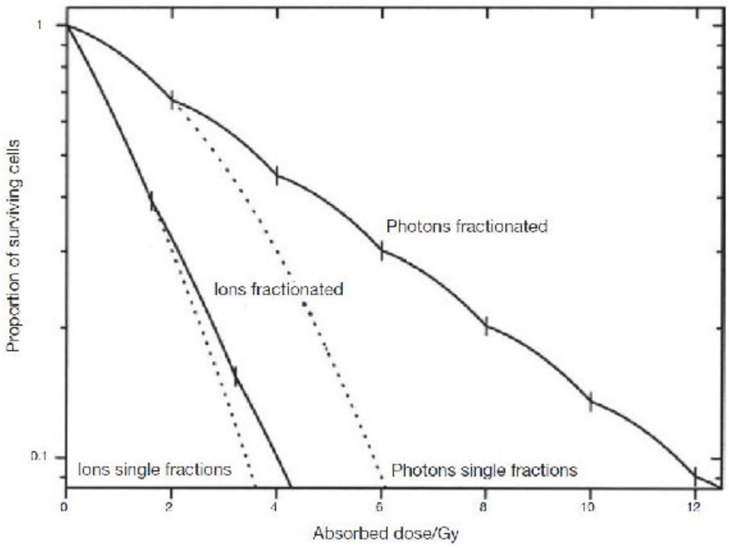

Figure 2.11: proportion of surviving cells as a function of the absorbed dose. Single (dashed line) and fractionated (continued line) doses are shown for low LET radiation (photons) and high LET radiation (ions) [97].

at low LET while the effect is much smaller for high LET irradiation (see figure 2.11) [97].

In general, we can distinguish three main types of damage to the DNA molecule: *Single Strand Breaks* type (SSB), easily reparable, *Double Strand Breaks* type (DSB), reparable in probability terms, and complex damages also known as *multiple-clustered damages* which lead to cell death with very high probability. The DNA damage can be *directly* induced or *indirectly* induced, meaning that the damage is induced by a chemical reaction between the DNA molecule and the free radical produced by the H_2O radiolysis [100]. Typically, high-LET (carbon ions) radiation is classified as directly ionizing radiation, meaning that DNA damages are directly induced. On contrary, low-LET radiations (photons, protons) induce indirect damages since they mostly exploit the H_2O radiolysis.

In order to better understand how physical information is connected to radiobiological response such as the cells death, important parameters such as the *Relative Biological Effectiveness* (RBE) and the Oxygen Enhancement Ratio (OER) are introduced.

2.3.1 Relative Biological Effectiveness

For historical reasons, the conventional radiation therapy represents in some extent a reference for particle therapy. On the other hand, a direct comparison in radiobiological terms between ions and photons would be possible only taking into account

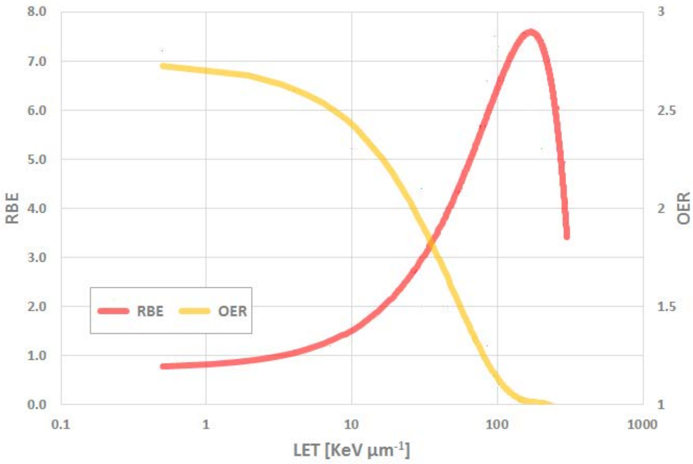

Figure 2.12: the RBE and the OER plotted as a function of the LET. Based on fast-neutron data from [102].

the different radio-biological response for a certain absorbed dose. This connection is typically complex and, even for single biological system or effect, it depends on several factors such as the fractionation scheme, the radiation quality and the level of oxygenation and temperature of the irradiated tissue [97]. Therefore, weighting factors are introduced to account for the different elements which may lead to the same biological effect of the tissue under consideration.

In clinical practice, it is recommended to report the prescribed RBE-weighted absorbed dose, still expressed in Gy, rather than the physical absorbed dose. The RBE concept is commonly used to quantify differences in biological effectiveness of different radiation qualities and it is defined as a ratio, between the "reference" absorbed dose D_γ (typically ^{60}Co [101]) divided by the dose D of the intended irradiation which results in the same biological effect:

$$RBE = \frac{D_\gamma}{D} \tag{2.20}$$

The RBE is influenced by many parameters as for example the LET (see figure 2.12). This dependency is rather important as it increases the effectiveness of the radiation at the very distal part of the SOBP (for protons, RBE up to 1.7 in the distal fall-off) [103] keeping at the same time a rather modest effectiveness in the proximal part of the dose distribution. In clinical practice, recommendations provided by ICRU and IAEA reports are usually followed and a constant value of 1.1 is applied entirely over the SOBP for proton irradiation [75, 97, 104]. On the contrary, the situation is particularly complex for ion beams as the RBE has a strong dependence in the position within the treatment beam [97]. Specific biological models are needed to characterize the biological response of the cells in case of ion radiation [98, 105, 106, 107, 108, 109]. In such a case, RBE values vary between 1.06 and 1.32 for the entrance region (LET = 13.3 keV/μm) and 2.00 and 3.01 for the Bragg peak region (LET = 77 keV/μm) [110].

2.3.2 Oxygen Enhancement Ratio

The oxygen level in the tissue is an important parameter which affects the biological response of tissue. In hypoxia condition, i.e. oxygen level low, the biological system is much less sensitive to low-LET irradiation compared to the situation when the oxygen level is higher (anoxia condition). Indeed, concentration of oxygen directly influences the production of free radicals, typically very reactive with DNA chains [100]. In other words, the higher the amount of oxygen in the tissue, the higher the number of DNA damages achievable. This explains why the re-oxygenation of the tumor cell is particularly important in case of indirectly ionizing radiation. The property of enhanced efficiency of the radiation depending on the amount of oxygen present in the tumor is know as *oxygen effect*. Monitoring the oxygen level in the tissue, allows to limit the required amount of dose to produce a wanted radiobiological effect. The ratio between the required dose for a known biological effect in hypoxia condition and the dose required to produce the same effect in anoxia condition defines the so-called *Oxygen Enhancement Ratio* (OER).

Considering low-LET radiations, hypoxic cells are about 2-3 times more resistant compared to the well oxygenated cells [97, 100] and even a low percentage of them can make the tumor resistant to radiation therapy (radio-resistant tumor) [97] On the other hand, the OER reduces when the LET increases (see figure 2.12) meaning that the radio-resistant tumors are better controlled by treatments with high LET radiation.

2.4 Proton dosimetry formalism

Common practice in proton dosimetry as well as in photon and electron dosimetry, is to calibrate the ionization chambers (IC) in standard laboratory with a reference beam quality. Since the IC is always used in a measurement which deviates from the reference, proper correction terms must be taken into account. Typical corrections are due to the temperature, the air pressure, the polarity and the recombination effect as well as factors related to the radiation quality. In more specific terms, the absorbed dose $D_{W,Q}$, measured at the reference position z_{ref} can then be expressed as [77]:

$$D_{W,Q}(z_{ref}) = M_Q N_{W,Q_0} k_{Q,Q_0} \tag{2.21}$$

where M_Q is reading of the measurement corrected for quantities independent from the radiation quality. More precisely, this term can be explicitly written as:

$$M_Q = M_Q^{'} \prod_i k_i \tag{2.22}$$

where with k_i is indicating any general correction due to the different conditions from the calibration under reference conditions in the standards laboratory. Typical corrections in this respect are [77]:

- $k_{T,P}$ factor to correct the response of an IC according to the temperature and pressure deviations from the temperature and pressure values of the IC in the standards laboratory;
- k_{sat} factor to correct the response of an IC for the lack of complete charge collection due to ion recombination;
- k_{pol} factor to correct the response of an IC for the effect of a change in polarity of the polarizing voltage applied to the chamber;
- k_{leak} factor to correct for leakage currents;
- k_s factor to correct for the stem effect;
- k_h factor to correct the response of an ionization chamber for the effect of humidity if the chamber calibration factor is referred to dry air.

The term N_{W,Q_0} in the formula 2.21 represents the calibration factor established in a standard laboratory with a radiation of quality Q_0 while the term k_{Q,Q_0} takes into consideration the irradiation of quality Q, different from the Q_0 used for calibration. One approach to determine the k_{Q,Q_0} factor is to measure it directly [111, 112]. Whenever this approach it is not possible, it is necessary to estimate the k_{Q,Q_0} factor by either analytical or numerical methods. Indeed, the k_{Q,Q_0} factor can be analytically expressed as [77]:

$$k_{Q,Q_0} = \frac{(\overline{S}^{W}_{air})_Q (W_{air})_Q}{(\overline{S}^{W}_{air})_{Q_0} (W_{air})_{Q_0}} p_{Q,Q_0} \tag{2.23}$$

where $\overline{S}^{W}_{air}$ indicate the mean stopping power ratio between water and air, according to the Spencer-Attix theory [113] while the term W_{air} describes the mean energy lost to create a pair of charges in air. The term p_{Q,Q_0} in the formula 2.23 describes the perturbation factor due to the detector itself [77, 114]:

$$p_{Q,Q_0} = \frac{p_Q}{p_{Q_0}} = \frac{[p_{cav} \cdot p_{cel} \cdot p_{dis} \cdot p_{wall}]_Q}{[p_{cav} \cdot p_{cel} \cdot p_{dis} \cdot p_{wall}]_{Q_0}} \tag{2.24}$$

every p_i term takes into account specific perturbations induced by the particular IC used for the measurement [77]:

- p_{cav} includes the correction due to the response of an IC for effects related to the air cavity. In particular, this term takes into consideration the electron fluence in the cavity which is different from that in the medium in the absence of the cavity [77];

- p_{cel} includes the correction for the effect of the central electrode during in-phantom measurements in high-energy photon (including ^{60}Co), electron and proton beams [77];
- p_{dis} includes the correction for replacing a volume of water with the detector cavity when the reference point of the chamber is taken to be at the chamber centre. It is the alternative to the use of an effective point of measurement of the chamber, P_{eff}. For plane parallel ionization chambers this correction is not required [77];
- p_{wall} includes the correction due to the response of an IC for the non-medium equivalence of the chamber wall and any waterproofing material [77].

With respect to the p_{eff} factor, which indicates the effective point of measurement of an IC, it is important to remark that for a radiation beam incident from one direction, p_{eff} is shifted from the position of the centre towards the source. The applied distance depends on the type of beam and chamber [77]. For instance, for plane-parallel ionization chambers p_{eff} is usually assumed to be situated in the centre of the front surface of the air cavity [77].

2.5 Conclusions

The basic physical and biological concepts for the light ion beam therapy as well as common terminology used in clinical practice have been presented. The Bethe-Bloch theory describes the energy lost by the protons traveling through the medium. The dependency of the stopping power to basic physical quantities such as the electric charge of an ion as well as the speed of the ion, explains the general shape the depth dose profile and the generation of the Bragg peak. The Molière theory instead, gives a mathematical description of the MCS which is responsible of the widening of the beam in depth and it characterizes the scattering of the lateral penumbra. For proton irradiation, the higher ionization density (or higher LET values) compared to photons, provides a justification of higher RBE values. For protons, the RBE is commonly fixed at 1.1 over the entire SOBP, according to clinical recommendations. Despite the weighting factor of 1.1 is often subject of discussion in the scientific community, it is clinically used in the majority of centres in the USA and Europe [97]. More complicated approaches must be faced for ion therapy in general, where it is necessary to exploit a biological model to characterize the complicated response of the cells to radiation. Noteworthy, high LET radiation shows low OER values, which justifies the rationale of ion therapy applied to radio-resistant tumors. The formalism for proton dosimetry does not differ considerably from the formalism applied to conventional radiation therapy. However, it is important to retrieve and to apply consistent correction factors in order to take into account the different beam quality as well as perturbations in the measurements introduced by the detector.

CHAPTER 3

The MedAustron Ion Therapy Center

The MedAustron Ion Therapy Center (MedAustron), built in Wiener Neustadt (Austria), started its clinical operations in December 2016. The aim of the facility is not only to treat cancer but also to perform advanced research studies in particle therapy. It is designed as a dual-particle facility, meaning that both proton and carbon ion irradiation are available for clinical treatments. As of July 2018, about 25 patients per day are treated with protons while the commissioning activities for the carbon beam are conducted. A total of about 1200 patients treated per year should be reached at full clinical operations [115].

The MedAustron project is based on the European experience of other dual facilities. At the time of writing this manuscript, only 4 dual-facilities are currently operating in Europe: the Heidelberg Ionenstrahl Therapiezentrum (HIT) (Germany), the Marburg Ionenenstrahl Therapiezentrum (MIT) (Germany), the Centro Nazionale di Adroterapia Oncologica (CNAO) in Pavia (Italy) and MedAustron. In this chapter a technical overview of the MedAustron facility is given.

3.1 The MedAustron Particle Therapy System

The MedAustron Particle Therapy System (MAPTS) is the medical integrated system of the entire facility. It is composed by several sub-system which act independently and in a synchronized matter. A detailed description of the MAPTS is out of the scope of this work but it is worth to mention important components such as the MedAustron Particle Accelerator (MAPTA), including the Dose Delivery System (DDS) and the Patient Alignment System (PAS) with major emphasis to the beam delivery part (section 3.1.1).

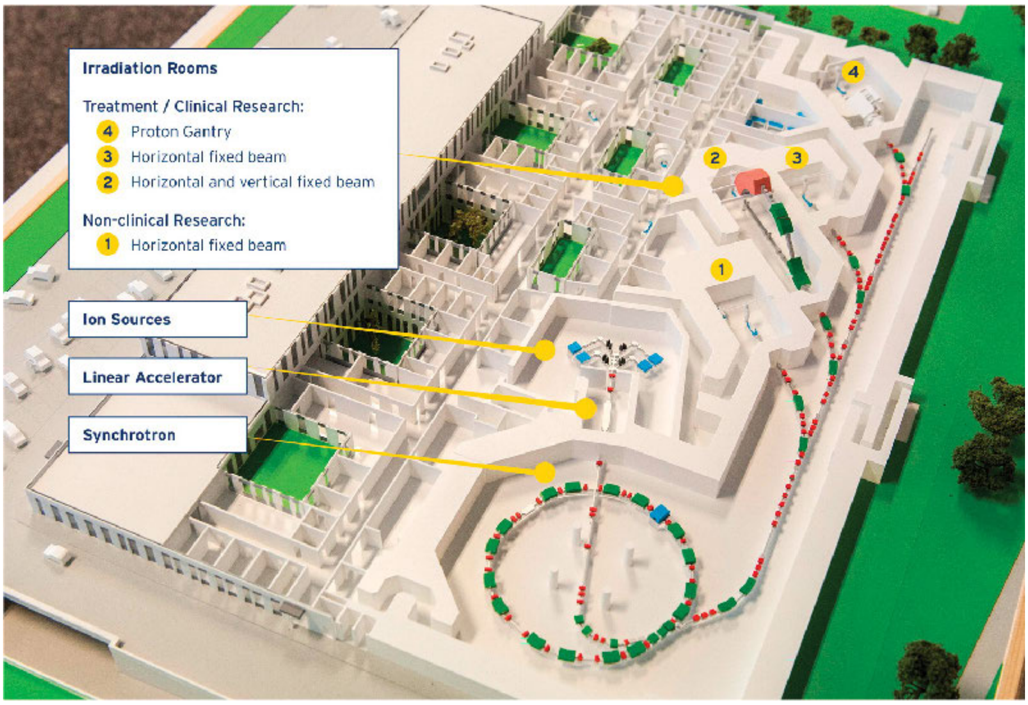

Figure 3.1: layout of the MedAustron Ion Therapy Center [115] including the four irradiation rooms.

The MAPTS supplies in total four irradiation rooms (IR). Three rooms (IR2 - IR4) are dedicated to patient treatments and one (IR1) to non-clinical research (NCR) where protons up to 800 MeV can be delivered (see figure 3.1). Both protons and carbon ions are deliverable in every room except for IR4 as it is equipped with a proton gantry[1]. IR3 is supplied by a horizontal beam line solely while in IR2 a vertical beam line is available in addition.

Noteworthy, a unique PAS developed within a cooperation between MedAustron, Buck Engineering and Consulting GmbH in Reutlingen (Germany) and medPhoton GmbH in Salzburg (Austria), is installed in each of the IR. The PAS consists of a ceiling-mounted robot equipped with table mounted imaging ring system made of an X-ray source (60-120 kV) and a flat panel detector (see figure 3.2). A large variety of couch movements are allowed at 7 degrees of freedom. An additional translation is offered by the linear axis which facilitates the movement of the patient towards the treatment head, at reduced air gap. The imaging system mounted directly on the couch permits an on-line imaging registration for the fine tuning of the patient positioning [116]. The non-isocentric treatment technique is routinely used at MedAustron and it has to be carefully performed as the PAS accuracy may

---

[1] The gantry has been developed in collaboration with the Paul Scherrer Institut (PSI) in Villigen (Switzerland).

Figure 3.2: picture of the ceiling-mounted robot used at MedAustron . An independently movable X-ray source and a flat panel detector (imaging ring) are mounted directly on the couch. The imaging ring system allows patient imaging before the irradiation for imaging registration purposes. The linear array which allows for translation movements is emphasized.

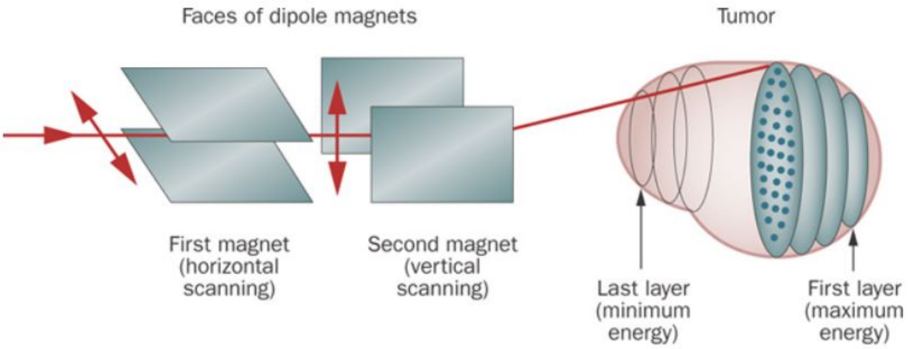

Figure 3.3: sketch of the active technique used at MedAustron for proton scanned treatments [118].

be reduced away from the isocenter. Further, as moving the patient away from the isocenter is not an usual clinical practice, it requires additional commissioning work[2]. On the other hand, non-isocentric treatments improve the dosimetric accuracy if the range shifter is used (more details are presented in chapter 4).

Last but not least, the package open-radART covers part of the software component of the MAPTS, providing the user interface medical-wise. It is composed by several routines which provide different functionalities. For instance, it handles patient data via the Oncology Information System (OIS) and the Patient Study Record (PSR), it interprets the DICOM prescription provided by the Treatment Planning System (TPS), it defines treatment steps (patient movement, imaging acquisition, passive elements movement, irradiation, etc..) via the Treatment Operation Editor (TOED), it reads the instructions provided by the TOED and it consequently interacts with the PAS as well as the MAPTA.

3.1.1 The Beam Delivery System

The Beam Delivery System (BDS) consists of two main parts: a synchrotron-based system inspired by the PIMMS design [117] and the treatment head. Treatments are delivered using the quasi-discrete spot scanning technique, implemented for dynamic beam delivery [75]. The tumor is subdivided into slices i.e. regions of the tumor volume reached by particles of the same energy (energy layer). Each slice is then scanned over the transverse plane to the beam direction (see figure 3.3).

In the clinical rooms, proton beams are available at 255 different energies in a range between 62.4 and 252.7 MeV (range in water from 3 to 38 cm with 1 mm steps till 18.8 cm and 2 mm steps otherwise) [119]. Out of the 255 available energies, subsets of regularly spaced energies are used depending on the requirements:

---

[2] The non-isocentrics positions need to be commissioned as well as the isocentric position. Increasing the degree of freedom for patient positioning results in additional commissioning work, meaning that every measurement performed at isocentric position needs to be repeated for every non-isocentric position.

Energy number	Energy value [MeV/n]	Category
1	62.4	Major, Key, Calibration
11	72.4	Major
21	81.3	Major, Calibration
41	97.4	Major, Key, Calibration, Verification
61	111.6	Major
81	124.7	Major, Calibration, Verification
101	136.8	Major
121	148.2	Major, Key, Calibration, Verification
141	159.0	Major
160	169.3	Major
170	179.2	Major, Calibration
180	188.7	Major
190	198.0	Major, Key, Calibration, Verification
200	207.0	Major
210	215.7	Major
220	224.2	Major, Key, Calibration
230	232.6	Major
240	240.8	Major
250	248.8	Major
255	252.7	Major, Key, Calibration

Table 3.1: summary of the sub-categories for the energies deliverable by the BDS. In total, 255 energies are available in order to provide ranges in water between 3 cm and 18.8 cm with 1 mm steps and with 2 mm steps between 18.8 cm and 38 cm. Out of the 255 available energies, subsets of regularly spaced energies were used depending on the requirements: 20 major energies, 5 key energies, 9 calibration energies and 4 verification energies.

- 20 major energies used for accelerator tuning, baseline data acquisition and TPS beam modeling;
- 5 key energies as representative set of the 255 for any baseline data measurement;
- 9 calibration energies used for DDS and TPS calibration;
- 4 verification energies to verify the beam model with RaShi.

The presented classification is summarized in detailed in table 3.1. Some of the most important BDS parameters are also summarized in table 3.2. As already mentioned, the BDS is designed in such a way that heavier particles than proton

Parameter	**Value**
Particles available	p, C^6
Particles foreseen	He^{2+}, Li^{3+}, Be^{4+}, B^{5+}, O^{8+}
Energy range	60 - 250 MeV for p 120 - 400 MeV/u per C^{6+}
Carbon Range	3 - 27 g/cm^2
Proton range	3 - 38 g/cm^2
Dose rate	2 Gy/min per liter of H_2O
Particles per spill	10^{10} for p 4×10^8 for C^{6+}

[a] isocenter measurements

Table 3.2: main BDS specification.

can be also accelerated and delivered. Currently, the facility is approaching the commissioning phase for carbon ions in a range from 120 to 400 MeV/u (from 3 to 27 cm in water) [115] and potentially He^{2+} Li^{3+} Be^{4+} B^{5+} as well as oxygen ions could also be taken in consideration in future.

The MedAustron Particle Therapy Accelerator

The MedAustron Particle Therapy Accelerator (MAPTA) can be summarized into the following parts (see figure 3.4):

- the ion sources
- the Low Energy Beam Transfer (LEBT) line
- the linear accelerator (LINAC)
- the Medium Energy beam Transfer (MEBT) line
- the synchrotron
- the High Energy Beam Transport (HEBT) line.

For the production of protons, MedAustron uses one of the three Electron Cyclotron Resonance (ECR) sources that can provide in principle different types of particles by simply changing the gas and the setting of some parameters, such as the power of the radio frequency (RF) or the electrodes extraction potential. From the sources, the beam is transported towards a Radio Frequency Quadrupole (RFQ) from the LEBT line. At the end of the LEBT, a fast electrostatic deflector allows only a pulse of beam (typically 30 us) to enter the RFQ. The beam energy is 8 keV/u after the sources and 400 keV/u after the RFQ. After the LEBT the beam is injected

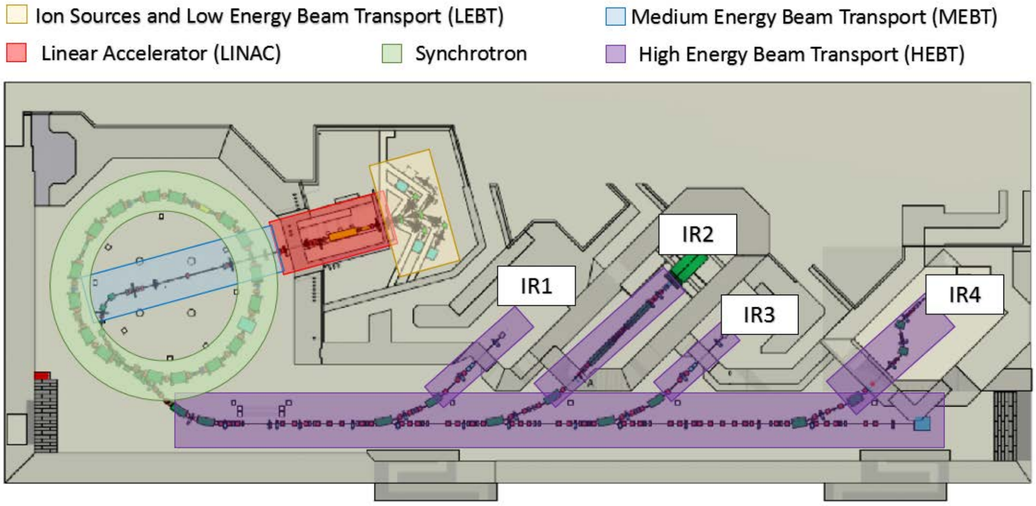

Figure 3.4: scheme of the MAPTA and its beam transport lines.

into the RFQ cavity. Here the beam is longitudinally accelerated and transversely adjusted in order to “bunch the beam” (*bunching* process) for injection into the LINAC. The energy achieved after the LINAC is 7 MeV per nucleon. Eventually the particles are sent against a stripping sheet that converts molecules H_3^+ into protons or $^{12}C^{4+}$ to $^{12}C^{6+}$. The ions H_3^+ and C_6^{4+} have the same charge to mass ratio, which implies the same settings for the LINAC and the beam line before the stripping foil. In order to avoid temperature variations and thus drift of resonance frequencies of the LINAC, it is necessary to keep it in operation even when no beam is accelerated. The LEBT fast deflector allows the beam to pass only once the synchrotron is ready (5 Hz frequency of synchronization). The MEBT is the next line and transports the beam from the stripping sheet to the synchrotron. Before entering to the synchrotron a degrader (a metal plate with holes of different sizes) might be inserted in order to reduce the transmission. In particular four degrader settings are available: 100%, 50%, 20%, and 10% transmission, corresponding to 0%, 50% 80% and 90% of beam intensity degradation respectively. With MAPTA in clinical mode, only commissioned degraders can be applied[3].

In the synchrotron-ring (approximately 25 m in diameter) the protons are accelerated from 7 MeV/u up to about 250 MeV/u . The particles circulate inside a high vacuum chamber and are kept within a quasi-circular trajectory by means of 16 dipoles whose task is to partially deflect the particles from their trajectory (see figure 3.5) . The ring is also equipped with correcting magnets including quadrupoles and sextupoles, which are responsible for the beam focusing, defocusing or correct higher order chromatic effects. The actual acceleration is achieved by a RF cavity while the extraction is driven by a betatron and a specific optic setting. A single

---

[3] Currently, 20 and 10% for the horizzontal beam line and 20% solely for the vertical beam line.

Figure 3.5: picture of some of the MAPTA components taken at the beam extraction section. It is possible to see part of the synchrotron (left side) and of the HEBT (right side). The dipoles and quadrupoles are colored in green and orange respectively.

synchrotron cycle, consisting of injection, acceleration, extraction time (*spill* time, typically 5 s) and time to return to initial conditions, lasts about 10 seconds at regular intervals.

The extraction from the synchrotron is performed spill by spill by means of the so-called *slow extraction* method [117] and the particles are then guided towards the IR through the HEBT. In the HEBT there are several beam diagnostic instruments, such as Scintillating Fibers Harps (SFX). Noteworthy is the magnetic chopper consisting of 4 magnets in-charge of interrupting the beam transport in case of interlock. The four chopper magnets are powered in series and polarized in order to bypass a dump, allowing the irradiation in the room only when they are turned on. If the magnets are turned off, the beam will not be diverted and will stop completely on a dump. The response time of the chopper is less than 300 μs.

The treatment head

To ensure patient safety as well as to perform an online-treatment beam diagnosis, each of the four beam lines is equipped with two dose-monitoring systems: the Dose Delivery System (DDS) and an Independent Termination System (ITS). The DDS used at MedAustron is based on the CNAO design [120] and it contains several beam monitors which are dynamically monitoring and controlling different beam parameters such as the beam position, the beam spot size and the number of particles released for each spot. A schematic overview of the entire treatment head design is shown in figure 3.6. Even though the ITS and DDS are two completely independent systems the DDS is divided into two independent parts, BOX1 and BOX2 [121]. In case of error, e.g. high discrepancies between the counts of the integral chambers or beam position errors greater than 2.3 mm, the DDS triggers an interlock to the

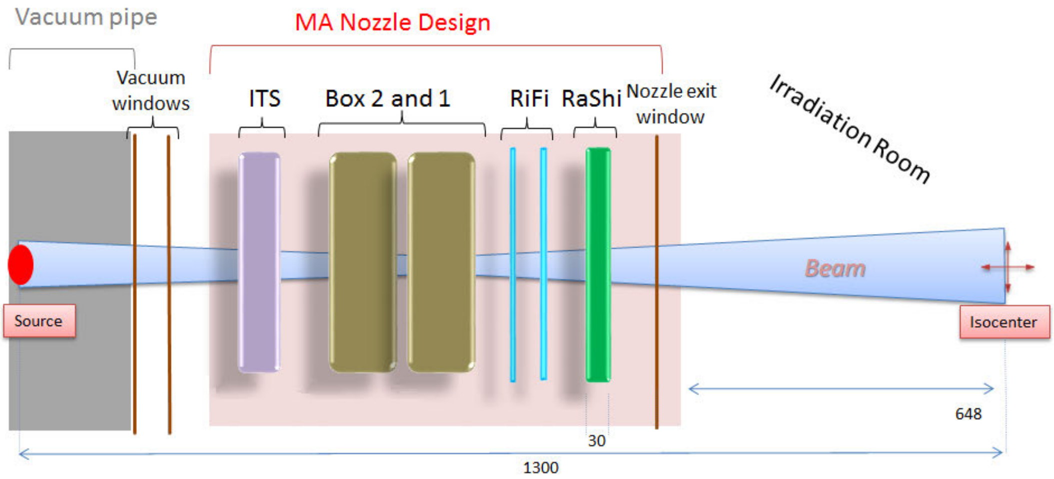

Figure 3.6: schematic illustration of the MedAustron treatment head (nozzle). It contains a double foil vacuum window, the Independent Termination System (ITS) box, Dose Delivery System (DDS) boxes, and the nozzle exit window. The passive elements, two Ripple Filters (RiFis) and the Range Shifter (RaShi) are also shown.

security system that activates the magnetic chopper.

Specific magnets so-called *scanning magnets*, move continuously the beam from spot to spot over every single slice (quasi-discrete scanning) with a speed which is beam energy dependent (370 m/s at maximum for protons at 62.4 MeV) and with a precision of mostly better than 1 mm. As soon as the entire slice is irradiated, the energy of the particles is decreasing in order to move to the next proximal slice. Unlike the passive technique where scatters and compensators are interspersed between the nozzle and the patient, the active technique avoids exposing the patient to unwanted doses due to the secondary spectra.

The passive elements such as Ripple Filters (RiFi) and Range Shifter (RaShi) are directly integrated into the treatment head design (see figure 3.7). The first are polymethyl methacrylate (PMMA) slabs that have triangular section slats of 2.0 mm thick [122]. Generally, for carbon ions, two RiFis are used orthogonal to the other in order to obtain a grid that shapes the Bragg peak increasing the Bragg peak width. For protons this is not necessary in general even though there might be situations where one RiFi is used. The RaShi is used both for carbon ion and for proton irradiation in case the target is located to very shallow depths, not reachable at the minimum energy.

3.2 The treatment planning system

A Treatment Planning System (TPS) is commonly used in clinical practice to calculate different dose configurations under specific constraints. The operating TPS

Figure 3.7: picture of the MedAustron passive elements (RiFi (a) and RaShi (b)). The passive elements are mounted in the treatment head (nozzle) in each of the beam line and are moved either in or out automatically by the RTSS whether required.

at MedAustron is RayStation[4] (RS) (RaySearch Laboratories, Stockholm, Sweden) which can provide a proton and carbon ions treatment plan with active scanning delivery (pencil beam scanning or PBS). RS supports different dose calculation engines but two in particular are of interest for the scope of this work: the pencil beam algorithm and the MC-based dose engine. The former, is extensively used in proton dose calculation [49, 48, 94, 123, 124, 125, 126, 127, 128] while the latter is implemented by the RaySearch Laboratories[5] to offer a higher accuracy approach to the user, despite a higher computational time [128]. The two dose engines are characterized by important similarities as well as substantial differences. For instance, both methods share the material characterization and the basic beam data for the beam model characterization[6]. Moreover, both algorithms compute on the fly the energy loss according to a simplified version of the equation 2.6 while the energy straggling is modeled as a Gaussian distribution (Bohr approximation) [128]. To better understand the differences, it is important to analyze the approximations which are applied by the two algorithms in order to describe the physics of the proton pencil beam. More details are presented for the pencil beam algorithm and for

---

[4] Version 6.1 was considered for this manuscript.

[5] As already mentioned in chapter 1, most of the commercial TPSs available nowadays offer alternative MC algorithms for treatment planning due to higher accuracy achievable compare to the standard pencil beam algorithm. However, although the basic idea is common to all the systems, the specific implementation might differ very much from vendor to vendor and it is not always easily accessible.

[6] The dose calculation performed by the TPS relies on the parameters provided by the beam model. For instance, the effective energy spectrum and the phase space characterization.

the MC dose engine in section 3.2.1 and 3.2.2, respectively.

3.2.1 The pencil beam algorithm

In the pencil beam method, the proton fluence is subdivided into a “large number of closely spaced mini-beam” [128], referred to as pencil beam. The phase space parameters are transported along the central axis of each of the pencil beam accounting for the energy loss, the MCS and the non-elastic nuclear scattering [128]. The energy loss is computed dynamically according to the formula 2.6 without correction terms considered and with a different formalism [128]. The energy loss in compound is computed according to the elemental composition (additivity rule), presented in section 2.2.1. Together with the Molière’s description for the MCS, the energy loss provided by the Bethe-Bloch formulation implies the transport of the core for the pencil beam [92, 128, 129]. In this framework, the pencil beam algorithm incurs into lower accuracy in dose prediction whenever the core of the pencil beam deviates from a Gaussian distribution. This is usually the case when the elastic scattering at large angle as well as non-elastic nuclear interactions are taken into consideration. To better account for the halo region contribution, RS uses a second Gaussian approach where the standard deviation is evaluated as:

$$\sigma^2 = (\sigma^{NS}_{corr})^2 + (\sigma^{MCS})^2 \tag{3.1}$$

where σ^{NS}_{corr} is the standard deviation of the Gaussian fit used for non-elastic nuclear scattering events based on look up tables [49] and experimentally corrected [128] while σ^{MCS} represents the standard deviation of the Gaussian fit applied to the core distribution (see equation 2.13). With this technique, the pencil beam algorithm satisfied the required 5% of acceptance level in absolute dose down to the FS of 4x4 cm^2 [128]. However, as the PB algorithm is neglecting the lateral inhomogeneities within the area of the spot fluence, the technique might suffers from reduced accuracy. A partial solution to this problem, is to divide the spot into a finite number of sub-spots [128]. Nevertheless, the 5% of tolerance level might be exceeded depending of the magnitude of the air gap[7], the presence of a RaShi, the angle of incidence for the pencil beam and shallowness of the target [128, 130].

Finally, the dose for each voxel is evaluated by summing up all the dose contribution for each j-th spot and for each e-th energy layer as described from the following equation [128]:

$$D(x, y, z) = \sum_e \sum_j K_e(E) w_{ej} d_{ej}(x, y, z) \tag{3.2}$$

where $K_e(E)$ is the energy dependent dose monitor calibration in number of protons, w_{ej} represent the meterset weight for j-th spot at the e-th layer and the term

---

[7] Intended as the distance between the nozzle exit window and the surface of the water phantom.

$d_{ej}(x,y,z)$ is defined as:

$$d_{ej}(x,y,z) = \sum_{k=1}^{N}(w_k \Phi_{ejk}^{MCS} IDD_{ejk}) + \Phi_{ej}^{NS} IDD_{ej} \tag{3.3}$$

where k is the index running on the number of sub-spot, Φ_{ejk}^{MCS} and Φ_{ejk}^{NS} is the fluence evaluated by Gaussian fit for MCS and non-elastic scattering events respectively. In particular, the standard deviations for the MCS and non-elastic scattering events are given by the Fermi-Eyges formalism with Rossi scatter power [128]. The IDD term represents the integrated depth dose determined from superposition of MC pre-calculated mono-energetic IDDs [128].

3.2.2 The Monte Carlo dose engine

The MC dose engine implemented in RS is not supported by any common MC toolkit [128] and it simulates the transport of the particles through the medium by the mechanism of the so-called random hinge method[8] [128]. Despite higher computational time, the transports take into account the energy loss, the energy straggling phenomenon, the MCS and the non-elastic nuclear interaction in a more accurate way compare to the pencil beam algorithm. However, the MC dose engine is optimized for clinical application, therefore particular effort is taken to enhance speed performances. As a consequence, considerable approximations are applied. For instance, a detailed transport is considered for primary and secondary protons solely, while for heavy secondaries (deuterons and alpha particles) only the energy loss in CSDA approximation is simulated. Further, no neutral particles as well as δ-ray are directly transported but considered in the energy balanced solely [128]. Finally, the energy loss and the non-elastic scattering is computed at every transversal voxel of the dose grid, while the MCS and the energy straggling phenomenon are evaluated per each random hinge till a minimum energy of 30.7 MeV is reached [128].

3.3 GATE and its role at MedAustron

As already introduced in section 1.3, an Independent Dose Calculations (IDC) becomes a necessary tool for all those cases where it is important to perform accurate dose calculation and it is highly recommended in clinical practice. The MC dose engine implemented in the TPS offers a valid alternative to the fast pencil beam algorithm and it can partially overcome many of the limitations presented in section 3.2.1. However, although the MC dose engine uses a different algorithm for dose calculation, it exploits the same beam model and some of the parametrizations as well as approximations. Therefore, a complete independent dose calculation engine which independently provides accurate dose calculation is still desirable and recommended in clinical practice.

---

[8] For a detailed description of the random hinge method the reader can refer to [128]

At MedAustron, the Geant4 Application for Emission Tomography (GATE) code has been selected as independent MC dose calculation tool. The tracking of a predefined number of particles (or histories) is repeated thousands of times according to the central limit theorem. The energy deposited by each particle is evaluated in each voxel in the user defined geometry, based on CT input, directly imported in the simulation. In this approach the best knowledge in terms of physics is available to the user which, on the other hand, must be aware about the accuracy limitations involved, as already presented in section 1.2. GATE offers a set of scripted commands to facilitate the access to the different capabilities of Geant4, which is the calculation engine. It is completely open source and is developed and maintained by the international OpenGate collaboration[9]. GATE is suitable for a large number of applications [63] and it represents a potential IDC for proton therapy as extensively discussed during a prior PhD project [73]. A specific source type dedicated to the scanned ion beam beam delivery technique is available in GATE and successfully implemented for a cyclotron-based proton facility [73]. Nevertheless, a specific characterization of the physical properties of the pencil beam still remains an unavoidable process which depends on the particular features of the delivery system. These aspects are a crucial part in the context of the presented work and they will be discussed in detail in chapter 4. Finally, a well benckmarked MC system built in-house can potentially save beam time for specific experiments as well as allows study of peculiar situations which are not experimentally feasible otherwise [8]. For instance, at MedAustron, GATE provides support to the medical physics group concerning the evaluation of IDD correction factors, the spot size prediction for the therapy accelerator group and the calibration in number of particles of the beam monitors unit of the treatment head. Noteworthy, at the time of writing, GATE is approaching its validation phase as supporting tool for the patient specific quality assurance (PSQA) protocols at MedAustron, as presented in detail in chapter 5.

3.4 Conclusions

The MedAustron Ion Therapy Center successfully concluded its commissioning phase of the first proton clinical room (IR3) in 2016. In the same year, the facility started its clinical activities and by the end of 2017 about 100 patients were treated. In this chapter, the MATPS has been presented as well as a description of the acceleration processes through the different components of the beam line. A detailed description of the treatment head has been given. The main dose calculation engines used by the TPS at MedAustron were introduced. Two algorithms have been presented: the pencil beam algorithm and the MC-based dose algorithm. The latter, although characterized by higher accuracy compared to the pencil beam algorithm, shares several input parameters as well as basic beam data for the characterization of the beam model. An independent MC based tool can provide an

---

[9] http://www.opengatecollaboration.org/

independent validation of the dose calculation performed by the TPS. GATE has been shown as potential candidate for IDC. However, a detailed characterization of the pencil beam must be developed to account for the MedAustron specifications, with particular emphasis to the non-isocentric treatments as well as the calibration of the BDS.

CHAPTER 4

Characterization of the MedAustron proton beam fixed line

In this chapter is presented a Monte Carlo beam modeling method developed in GATE for the MedAustron fixed beam line where clinical constraints are fulfilled at isocentric and non-isocentric positions. Compared to the current literature, the proposed model includes a full description of the nozzle geometry and is calibrating according to a new dose-area-product formalism used for the first time in clinical applications [131]. A detailed validation is performed in 3D, for different cubic targets in water, including non-isocentric conditions and the use of a range shifter.

The proton beam optic is parametrized at the nozzle entrance considering the correlation between beam spot size and divergence (beam emittance). Measurements of the FWHM in air are used as reference. The energy spectrum is modeled in order to reproduce the measured depth dose profile in water. The relationship between number of particles and dose-area-product measured in reference condition, needed for beam monitor calibration in terms of reference absorbed dose to water, is determined. Typical longitudinal parameters (range, distal penumbra and modulation) and transverse parameters (field sizes and lateral penumbra) for proton dosimetry are evaluated. The work presented in this chapter was submitted in similar form to Medical Physics journal on July 2018 [132]. Compared to the submitted paper, the version here contains more details, figures and explanations.

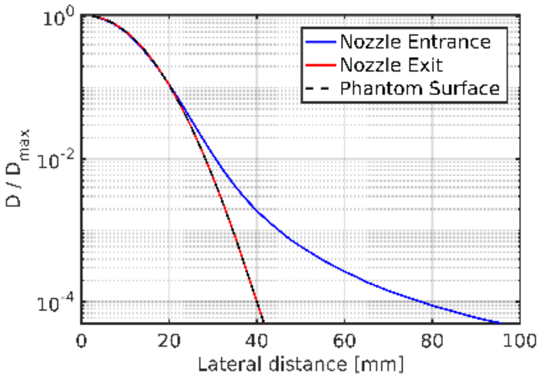

Figure 4.1: simulations of a 62.4 MeV proton beam where the source was positioned at three different positions: nozzle entrance, nozzle exit and at the phantom surface. The source positioned at the nozzle entrance allows the characterization of the beam halo due to the secondary spectra produced by the nuclear inelastic scattering in the nozzle.

4.1 Introduction

For proton beam delivery, the air gap between the nozzle exit window and the patient can enlarge the lateral penumbra, as well as lead to lower accuracy of the pencil beam algorithm, especially if the Range Shifter (RaShi) is considered [49, 130]. One possible solution to reduce the air gap in clinical practice is to move the patient towards the nozzle exit. Monte Carlo (MC) simulation tools are often used for independent dose calculation as they can provide useful insights that cannot be obtained otherwise [72, 133, 134, 135]. However, any independent dose calculation engine should be carefully characterized and validated before its implementation in clinical applications. Typical characterization of a proton beam can be performed based on measured depth dose curves, spot maps measured at different air gaps and dose measurements in reference condition [69, 124, 136]. In the literature, different methods for proton pencil beam modeling have been proposed depending on the type of the MC code and on the characteristics of the beam line [72, 69, 136, 137, 138, 139]. For active scanning systems, accurate simulations of a proton pencil beam require a deep understanding of the pencil beam optics properties as the correlation between proton position and angular spread (beam emittance) cannot be neglected a priori [72]. Omitting the simulation of the nozzle geometry allows an empirical modeling of the pencil beam with an additional reward in computational time [136, 137, 139]. Nevertheless, this approach requires additional corrections [49, 140] to account for large-angle single scattered primary and secondary particles produced in the nozzle components [74, 94, 136] (see figure 4.1). In this work, we provide a beam model of the MedAustron fixed beam lines using a full nozzle modeling approach that will be used as a reference for future independent dose calculation.

Particular attention is given to the modeling and the validation of the pencil beam properties in non-isocentric conditions as routinely exploited for patients treatments at MedAustron since December 2016. In addition, we exploit the Dose-Area-Product (DAP) formalism [131] for absolute dose calibration in terms of delivered protons, differently from the traditional Monitor Unit (MU) calibration [139, 141, 142]. The three-dimensional dose distribution simulated in water is carefully validated in terms of ranges, distal penumbra, modulation, field sizes and lateral penumbra, evaluated for different cubic targets in water, including non-isocentric conditions and the use of a range shifter (RaShi).

4.2 Material and method

The proposed MC beam model is based on analytical functions with parameters values derived from experimental measurements data. A short description of the MedAustron beam delivery system including the nozzle design is reported in section 3.1.1. Section 4.2.1 describes the experimental data acquired at MedAustron during its commissioning phase. The data are split into two sets: one set used for the beam model parametrization and one set for validation. Section 4.2.2 describes the MC setup and the beam modeling method while section 4.2.3 and section 4.2.4 are dedicated to the absolute dose calibration and validation procedure, respectively. In the following, the nomenclature summarized in table 3.1 will be used.

4.2.1 Experimental data

Experimental data used for beam modeling were acquired during medical physics commissioning activities. Part of this data consist of spot profiles acquired in terms of FWHM at seven air gaps using the Lynx scintillating screen (IBA-dosimetry). Measurement positions will be referred to as follows: ISD+20cm, ISD0, ISD-20cm, ISD-30cm, ISD-40cm, ISD-50cm and ISD-58cm where the ISocenter to Detector surface (ISD) with negative value is towards the nozzle (reduced nozzle-to-patient-entrance air gap). Additional spot maps were acquired at ISD0, ISD-30cm, ISD-40cm, ISD-50cm and ISD-58cm when the RaShi was in place for 4 verification energies. The uncertainties on the spot size and position measurements were 0.2 mm respectively. Further data consist in depth dose profiles acquired in water at isocenter using the water phantom MP3-PL (PTW, Freiburg) with the Bragg peak chamber TM 34070 (electrode diameter of 81.6±0.2 mm). Further, the MP3-PL was aligned at ISD-50cm when measurements using the RaShi were acquired for the 4 verification energies. The uncertainties of the range in water were varying from 0.3 mm to 0.6 mm, depending on the depth [143]. With respect to beam monitor calibration in reference condition (see section 4.2.3), absorbed dose to water was measured in a uniform single-layer of 12x12 cm^2 for 9 calibration energies applying IAEA TRS-398. Dose values were acquired using an ionization chamber TM 34001 (Roos-type, electrode diameter of 15.6±0.2 mm) placed at 1.4 cm in depth for ener-

Purpose	Measurement description	Measured parameters	Measurement parameters
beam optics modeling	spot map	Source Axes Distance, FWHM in air	20 major energies per 7 air gaps
energy spectra modeling	depth dose profile for a pristine Bragg curve	range in water, integrated depth dose profile	20 major energies at isocenter
beam optics residual evaluation with RaShi	spot map	FWHM in air	4 verification energies, 5 air gaps, with RaShi
depth dose residual evaluation with RaShi	depth dose profile single spot	range in water, integrated depth dose profile	4 verification energies measured at non-isocentric position with RaShi
beam model dose calibration and residual evaluation in 2D	dose in reference condition for scanned fields	Dose Area Product	9 calibration energies
beam model final validation in 3D	3D dose distribution in water	field size, lateral penumbra, modulation, dose	3 boxes measured at isocenter, 1 box measured at non-isocentric position with RaShi

Table 4.1: summary of experimental data used for generation of the MC beam model and for its validation.

gies up to 97.4 MeV and at 2.0 cm depth for larger energies, up to 252.7 MeV. DAP to water was derived by multiplying the absorbed dose to water with the product of the constant spot spacing $\Delta x\ \Delta y$ as described in Palmans and Vatnitsky [131]. The same measurement technique used for beam monitor calibration was used to validate the dose in reference condition. Three dimensional cubic-shaped dose distribution measurements were performed in water using 24 ionization chambers TM 31015 (PinPoint type with measuring volume 0.03 cm^3 and radius 1.49 mm, PTW, Freiburg) characterized in proton beam [144]. The 24 PinPoints were mounted in a holder (3D Detector Block) attached to the moving mechanism of the MP3-PL water phantom, allowing a quasi-three dimensional verification of delivered dose distributions [143]. In order to acquire transverse dose profile, the 24 PinPoints were mounted on a linear holder positioned perpendicularly to the beam direction (see figure 4.2). The measurement resolution for the transverse profile available with this method was 2 mm. Box6(0,0,6), box8(0,0,15), and box10(0,0,25) were delivered at isocenter where the notation boxN(0,0,Z) stands for a cubic dose distribution with an N cm side-length and its center placed at the water equivalent depth Z. A fourth box, the box6(0,0,5), was delivered for non-isocentric conditions (ISD-50cm) using a RaShi. Table 4.1 summarizes the measurements performed and their purposes.

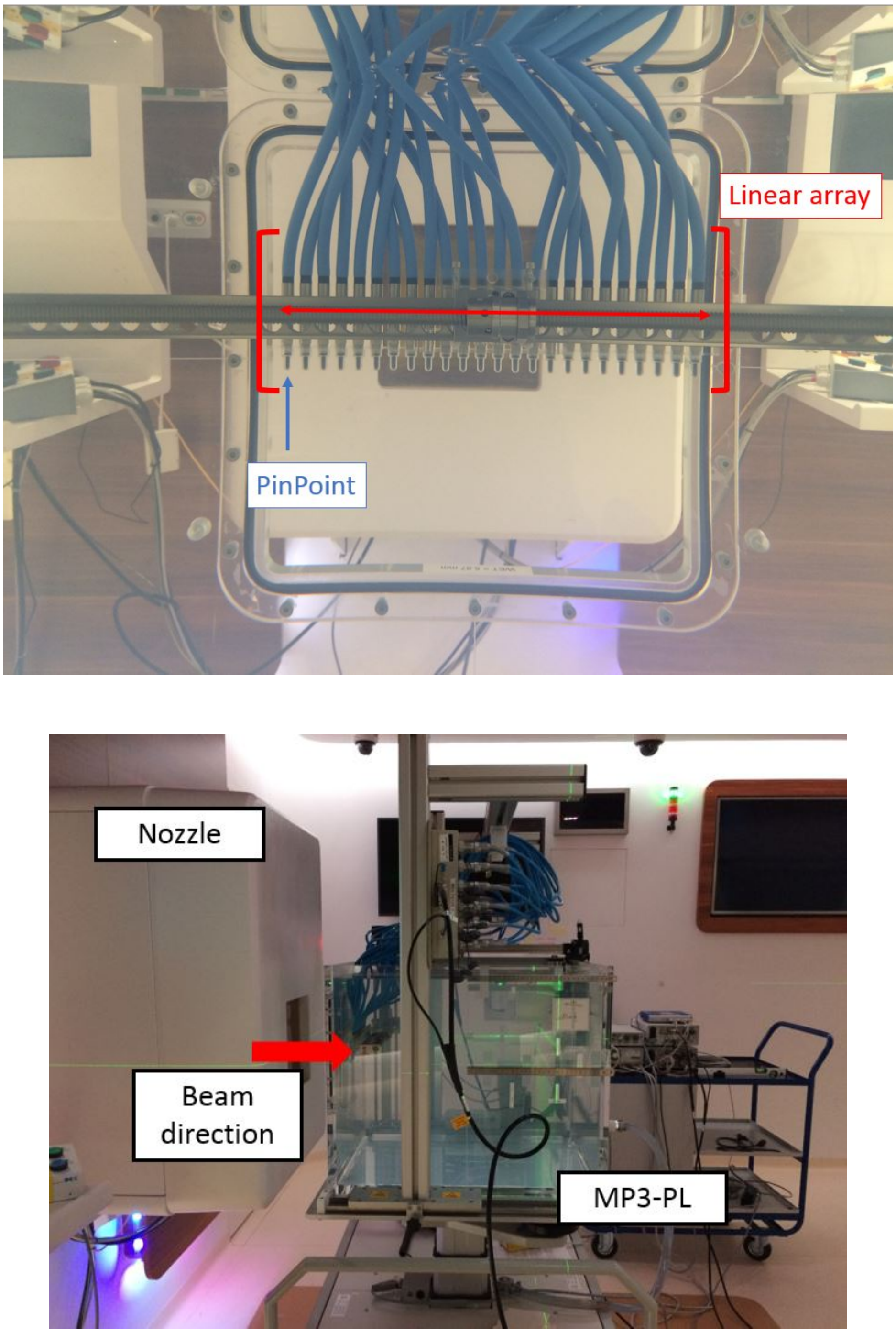

Figure 4.2: pictures of the 1D linear array holder (above) for the 24 PinPoint mounted on the mechanical arm of the water phantom MP3-PL (PTW, Freiburg) aligned at ISD-58cm for acquisition of the transverse dose profile.

4.2.2 Monte Carlo modeling method

GATE v7.2 [63, 64] built with Geant4 v10.02 [56, 57] was used. The classification reported in table 3.1 was applied. This work was supported by in-house routines developed in python v2.7 [145], root v5.34 [146] and specific open-source tools provided by the CREATIS laboratory[1] [2].

Treatment head modeling

The nozzle design implemented in the simulations follows the description presented in section 3.1.1. The terminal part of the synchrotron and the window of the vacuum pipe were included in the geometry of the nozzle as shown in figure 3.6. Both DDS and ITS were taken into account. Passive elements, such as RaShi and RiFi, were also placed in the nozzle and inserted when required. A detailed modeling of the elemental part such as the integral chambers were based on technical drawings and specifications. Wherever possible, the distance to the room Isocenter (ISO) of the single component of the nozzle was measured by means of a laser tracker AT402 (Leica). Modeling was restricted to elements within the beam path. Calculated (and confirmed by measurements) total WET of the entire nozzle is 2.4 mm.

Geant4/GATE physics-list

The selection of the employed physics models in GATE/Geant4, referred to as physics list, is a crucial step. Several recommendations are available in the literature and evolved over the years with Geant4 versions: binary cascade [147, 148], precompound [149], Bertini or Precompound [150]. Depending on the specific physics builder selected in GATE, it is possible to switch between the different physics model of Geant4. During independent studies performed in-house the low-dose envelope simulated in water for the QGSP and QBBC builders respectively, was compared to measured transverse dose profile at different depths and for four energies (61.9, 123.5, 186.9, 250.3 MeV) [151]. The QBBC physics-builder [152] uses the binary cascade and the Bertini models depending on the particle type and energy range. QGSP allows the activation of a specific physics model (either Bertini or binary cascade). With respect to the MCS, the Wentzel and the Urban models [153, 154] were tested to characterize the proton pencil beam propagation in air.

Geant4/GATE parameters-list

A sensitivity study on the basic parameters such as the *step limiter*, the *tracking cut* and the *production cut* were performed following indications available in [149]. A main cylinder with 50 cm in radius, 40 cm in depth and made of G4_WATER was positioned with the circular face at center of the Gate world made of air. The

---

[1] https://www.creatis.insa-lyon.fr/rio/vv

[2] https://public.kitware.com/open-regate/index.php/Main_Page

depth dose profiles were scored in different sub-cylinders defined every 5 cm radius. Number of primaries used for these simulations was set at 10^5 while the energy spread was set to 0.1 MeV. Tracking cut, production cut and step limiter were changed systematically in order to understand their impact on our results. A dedicated analysis was performed concerning the water ionization potential I_w. Three values 75, 78 and 81.77 eV were tested for four energies (61.9, 123.5, 186.9, 250.3 MeV). R80 values were evaluated from depth dose profiles and compared to the measurements.

Modeling the beam optics

Seven phase space scoring planes (PhS) were used to study the optics of the pencil beam propagating through air. The PhSs were placed at seven different positions according to the Lynx positions described in section 4.2.1. At this step, energy spread was set to 0 MeV. Number of primary protons was set to 10^5 in order to achieve a repeatability of independent runs of less than 0.2 mm. An initial set of spot size, beam divergence and beam emittance was selected according to independent analytical beam transport simulations in vacuum at the source position. These parameters were estimated at 1.3 m upstream the isocenter, i.e. at the nozzle vacuum window entrance, to produce a spot of 4 mm FWHM at ISO in vacuum. The relative uncertainty of these initial parameters was estimated to be 20%. The spots were assumed to be symmetric and identical in the horizontal and vertical planes. An iterative process was run in order to optimize the spot sizes (σ_x and σ_y plane), the divergences (σ_θ and σ_ϕ), and the emittances (ϵ_x and ϵ_y) for both planes independently. All corrections were performed respecting the following constraint:

$$\epsilon_{x,\theta}^{source} \leq \pi\sigma_x\sigma_\theta \tag{4.1}$$

where $\epsilon_{x,\theta}^{source}$ is the emittance for the horizontal plane at the source position, σ_x is the standard deviation of the Gaussian function characterizing the spot size in the horizontal plane in mm and σ_θ is the standard deviation of the Gaussian function characterizing the divergence in the horizontal plane evaluated in mrad. The equivalence in equation 4.1 is reached at the position referred to as *waist position*, where the spot size in vacuum is the smallest possible. An analogous constraint was used also for the vertical plane. The current methodology available in literature showed limitations in describing the pencil beam optic properties directly at the nozzle entrance. A linear interpolation of the spot size measurements after the nozzle cannot back-procject the optical properties at the nozzle entrance. Alternatively, the characterization of the source can be seen as an optimization problem. Increasing, the spot size at the source position directly affects the spot size at the isocenter with a linear correspondence (to first approximation). The initial divergence affects the spot size variation over the distance. In general, corrections on this parameter are very limited due to the intrinsic limitation introduced by equation 4.1 as well as their small values (always lower than 1 mrad). With such small values for the divergence, the scattering in air is the predominant effect, especially at low energies. Nevertheless, at higher energies, it was possible to appreciate how increasing the divergence

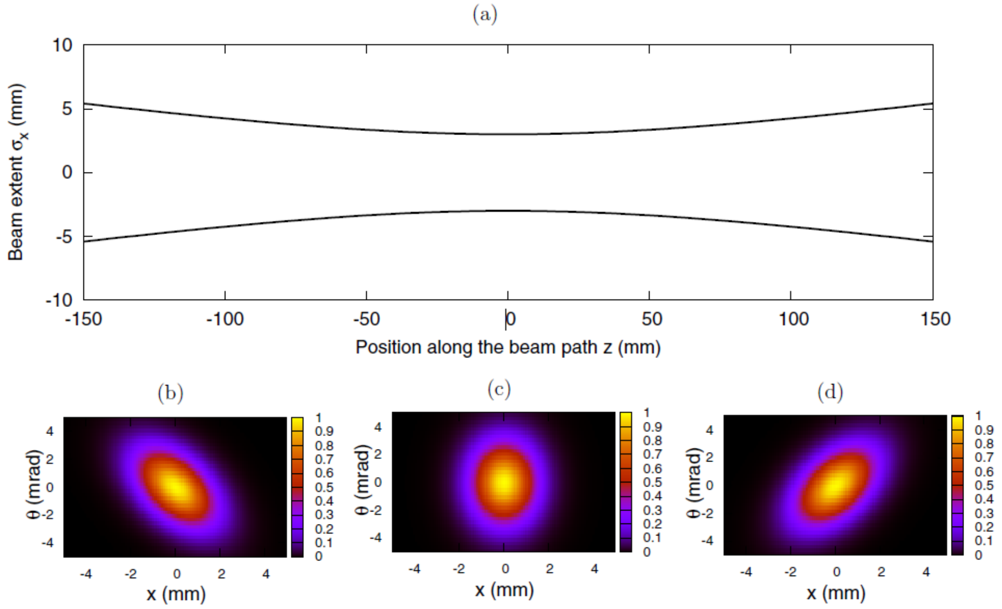

Figure 4.3: characterization of the pencil beam optical properties. In (a) is shown the propagation of the spot size as a function of beam path in vacuum. In (b), (c) and (d) is shown the correlation between beam size and divergence (phase space) at three different positions. In this case, the condition of symmetrical emittance is verified in $z = 0$, corresponding to the waist position [137].

of a converging beam produces a smaller spot size very close to the nozzle and a larger spot size for increasing air gaps. Corrections on the initial emittance mainly influence the rotation of the elliptic phase space along the beam axis, moving the beam waist position (see figure 4.3). The beam optics parameters were iteratively adapted to minimize (whenever possible, down to 0.2 mm) the differences between measured and simulated FWHM at non-isocentric positions for the horizontal and for the vertical plane. The tolerance of 1 mm in absolute deviation and 10% in relative terms was considered for the five key energies (62.4, 97.4, 148.2, 198, 252.7 MeV) in all the positions, according to clinical practice at MedAustron. Eventually, the beam parameters (spot size, beam divergence and beam emittance) were described over the full clinical energy range by a n-th order polynomial fit to the five key energies, with n from 1 up to 8 depending on the specific parameter. Residuals between simulated and measured spots were evaluated for 20 energies measured at 7 different air gaps. In total, 280 residuals evaluations were performed at this phase of the study in absolute and relative terms. Same residuals evaluations were performed on 4 verification energies with RaShi at 5 air gaps.

Tuning the depth dose curves

Depth doses were scored in a water box simulating the water phantom. To reproduce the experimental setup described in section 4.2.1, a scoring region with a cylindrical shape of 4.08 cm radius was defined. A scoring resolution of 0.1 mm in depth was set. Parameters of the MC simulations being tuned were the mean energy E and the energy spread dE. Energy properties were estimated by an iterative procedure to match MC simulations with measurements in terms of R80 and the BPW80. Other parameters have been evaluated such as R90 and Rp defined as the 90% and 10% dose level, respectively, in the distal fall off of a depth dose profile, according to section 2.1. To improve the agreement between simulations and measurements, two main steps were performed. First, the mean energies required by the simulations to reproduce the measured ranges were adjusted until reaching an agreement better than 0.3 mm. Second, the energy spread adjustments were performed in steps of 0.1% of the mean energy values for each energy. The adjustment of the energy parameters has been performed on the 20 major energies simulating 10^6 primary protons. Residuals evaluation was performed in terms of R80, Rp, R90, BPW80 for the same energies with RaShi and water phantom aligned at ISD-50cm.

4.2.3 Beam model dose calibration

In order to calibrate in absolute dose the MC simulations it is necessary to know the number of the delivered particles. This means that it would be possible to re-scale the simulated number of particles in order to match the measured DAP at reference condition:

$$\frac{N_{delivered}}{N_{GATE}} = \frac{DAP_{meas}(z_{ref})}{DAP_{GATE}(z_{ref})} \tag{4.2}$$

However, the delivered number of particles is not known *a-priori*. One possibility is to correlate the measured DAP at reference condition and the delivered number of particles $N_{delivered}$ exploiting the MC simulations itself [131]:

$$N_{delivered}(E) = \frac{DAP_{meas,W}(z_{ref})}{d_W(S^{\rho}_{el}, \Phi_z) \cdot A} \tag{4.3}$$

The numerator of the equation 4.3 is the experimentally determined DAP in water at the reference depth z_{ref} over the area A. In general, the term $d_W(S^{\rho}_{el}, \Phi_z)$ represent the "mean stopping power" per incident proton evaluated in water by any dose engine and it is characterized as follow:

$$d_W(S^{\rho}_{el}, \Phi_z) \cdot A = \frac{\sum_i \int (S_{el,i}(E)/\rho)_W \Phi_{z,i}(E) dE}{n} \tag{4.4}$$

The $(S_{el,i}/\rho)_W$ term represents the mass electronic stopping power of water for ion species i and $\Phi_{z,i}(E)$ is the fluence differential in energy of that ion species at

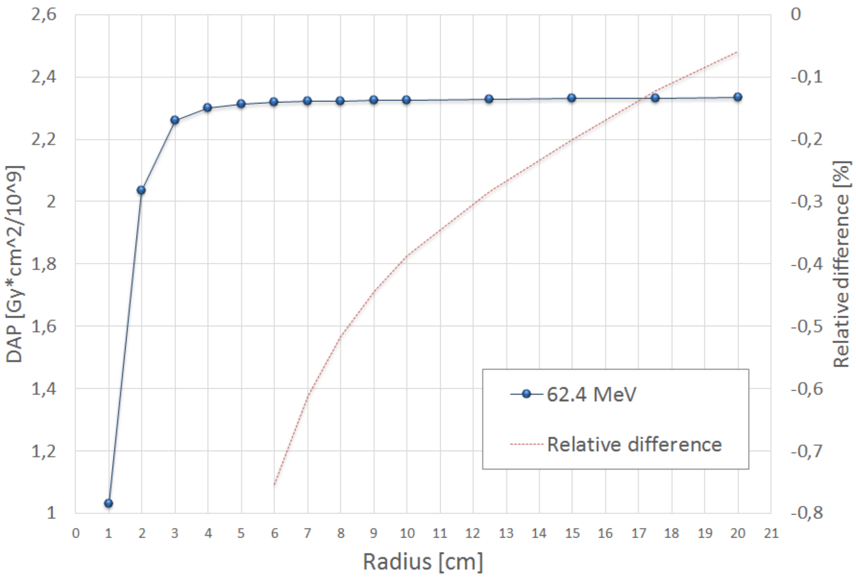

Figure 4.4: the DAP for a 62.4 MeV proton pencil beam plotted as a function of the chamber radius. Less than 1% differences relative to the section of the full water phantom is observed in the collected dose between a chamber of 7 cm radius and the maximum radius of 20 cm.

the reference depth $z = z_{ref}$. The key point of this approach is to calculate by a dedicated MC simulation the $d_W(S_{el}^{\rho}, \Phi_z)$ term for a known number of protons n, as described by equation 4.4. Therefore, a single pencil beam was simulated and scored in a cylindrical volume of 7 cm radius, sufficiently large to encompass all the charged particles of the radiation field over the full clinical energy range (see figure 4.4). Electrons were omitted from the tracking by specifying a large production cut of 5 mm (meaning that electrons with an energy range lower than 5 mm in the current medium are not directly simulated; their energy is considered deposited locally). Energy deposited was scored without discriminating between primary or secondary particles. A resolution of 1 mm in depth was used. Depending on the energy, two main reference depths were considered: 1.4 cm in the energy range between 62.4 MeV and 97.4 MeV, and 2 cm from 97.4 MeV up to the maximum energy value (252.7 MeV) (see section 4.2.1). These correspond to the reference depths used at MedAustron.

4.2.4 Beam model validation

A final validation was performed in terms of 3D dose distribution in water for the four 3D dose cubes of different dimensions simulated in water with 1.8×10^8 particles. The local dose deviations from measurements were calculated for different positions of the 3D holder according to the following formulas:

$$\bar{\Delta}^{GATE} = \frac{1}{N}\sum_{i}^{N}\frac{(D_i^{GATE} - D_i^{meas})}{D_i^{meas}} \tag{4.5}$$

$$\bar{\Delta}_{ABS}^{GATE} = \frac{1}{N}\sum_{i}^{N}\frac{|D_i^{GATE} - D_i^{meas}|}{D_i^{meas}} \tag{4.6}$$

where N is the number of the PinPoints used for the measurements, D_i^{meas} is the dose measured for the chamber i and D_i^{GATE} is the dose calculated by GATE. For the evaluation of $\bar{\Delta}^{GATE}$ and $\bar{\Delta}_{ABS}^{GATE}$, the 3D holder was placed in a region were at least the 95% dose level was reach (target region). Wherever possible, an additional evaluation was performed for a proximal dose region (plateau region), where a dose level within 60% and 95% was reached. Dose values measured by chambers located where the dose gradient is higher than 0.04 Gy/mm were excluded from the analysis. Transverse profiles were selected at the center of the SOBP and analyzed in terms of FS50 and LP80-20 of the dose profile. Furthermore, distal parameters such as R90, R80, Rp, MOD90, and DP80-20 were analyzed.

4.3 Results and discussion

We report the obtained results following a similar structure of section 4.2.2. A dedicated section for the beam source modeling residuals (spot sizes and depth dose profiles) including absolute dose evaluation. A specific section is assigned to the independent validation of the beam model with emphasis on 3D dose distributions. Unless otherwise stated, deviations in the subsequent sections always refer to differences between simulated and measured values.

4.3.1 Beam modeling residuals

Geant4/GATE physics-list

The physics builder QBBC was selected as suggested from the results reported in [151]. The simulated transverse dose profiles for all the physics builders were in a good agreement with the measured data. From the analysis of the tails, the QBBC physics builder has shown slightly better agreement with measurements than QGSP when binary cascade solely was activated. Inferior agreement was achieved with the Bertini model activated. Many details concerning the obtained results are reported in the following study [151]. With respect to the MCS models selection, recommendations provided in [155] were followed. According to [155], the Urban model has shown increased limitations compare to the Wentzel model for very thick targets of different materials close to the particle range. Therefore, the option 4 of the electromagnetic process (EMZ) available in GATE/Geant4 was activated in order to use the Wentzel model for the description of the MCS.

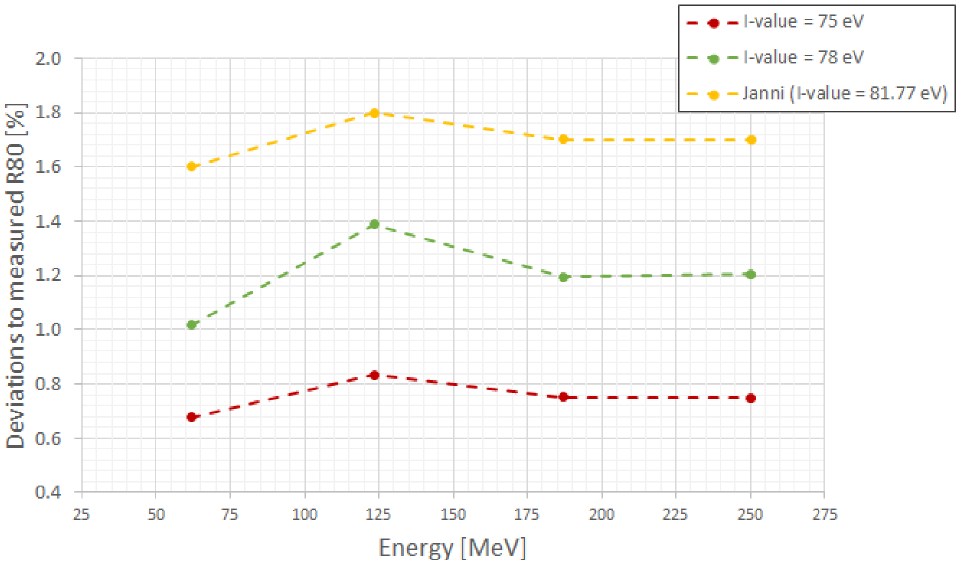

Figure 4.5: deviations in terms of R80 obtained for different I-value

Geant4/GATE parameters-list

For I_w = 78 eV an average deviations of 1.2% was found (see figure 4.5). Best and worst mean agreement, 0.7% and 1.7%, were obtained for I_w = 75 eV and for I_w = 81.77 eV, respectively. Despite the best agreement obtained with I_w = 75 eV, the value I_w = 78 eV was selected. Using I_w = 78 eV would require a reasonable additional tuning of the nominal energy values during the modeling process of the depth dose curves. In addition, this particular value is a good compromise between ICRU recommendations [156], tabulated values reported in [89], and considerations available in [7].

Optic residuals

The optimal optical beam model parameters found, resulted in a 99% pass rate of the clinical 1mm/10% requirement. As expected, the largest deviations of 1.8 mm (7.2%) and 1.7 mm (6.9%) were obtained for 62.4MeV at ISD+20cm in the vertical and horizontal planes, respectively (see figure 4.6). In fact, the accuracy of the MCS model implemented in Geant4 is mainly driving the agreement in FWHM as the scattering is the most predominant effect for this energy and position. On the other hand, this combination of energy and position is not clinically relevant in proton therapy. If a RaShi is considered, a systematic deviation from the measured spot size was observed (see figure 4.7). This behavior is attributed to an overestimation of the MCS [155]. However, observed deviations are within clinical tolerances for all the analyzed energies (maximum deviation was 10% at ISD0 for 97.4 MeV).

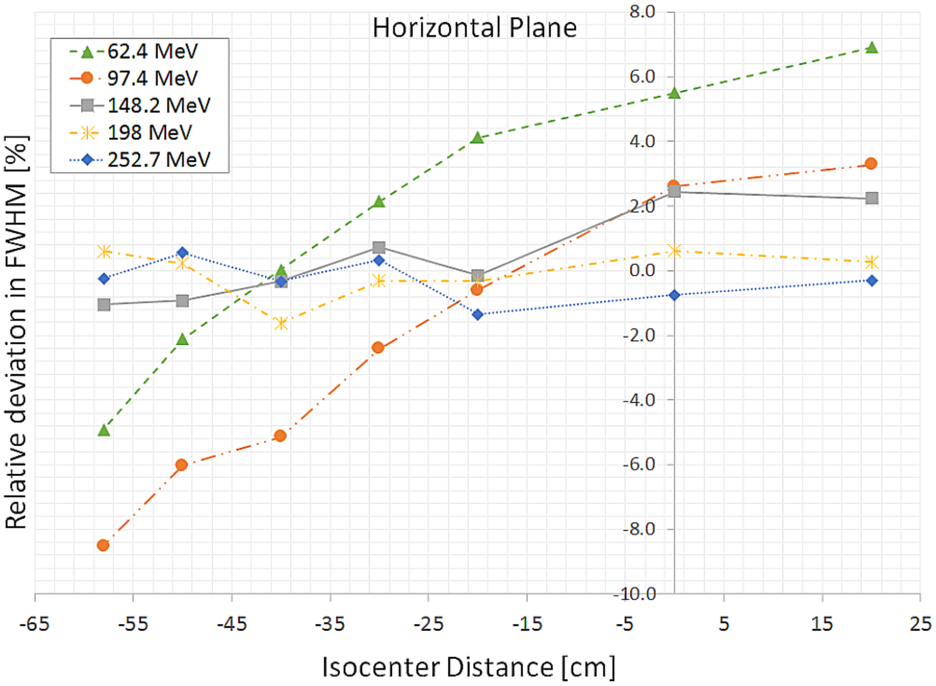

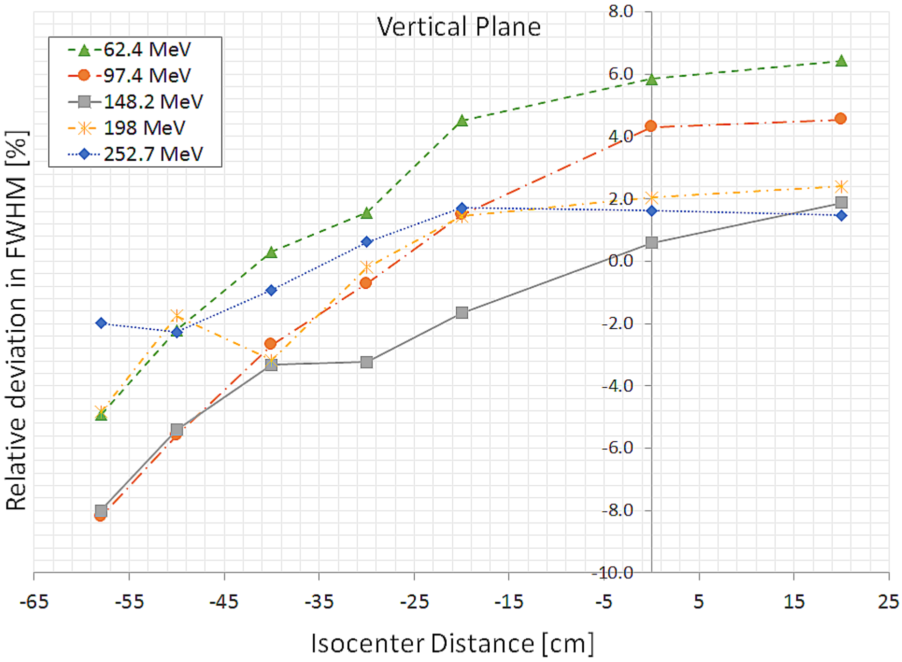

Figure 4.6: relative deviations in FWHM for 5 key energies at 7 air gaps for horizontal (above) and vertical (below) plane.

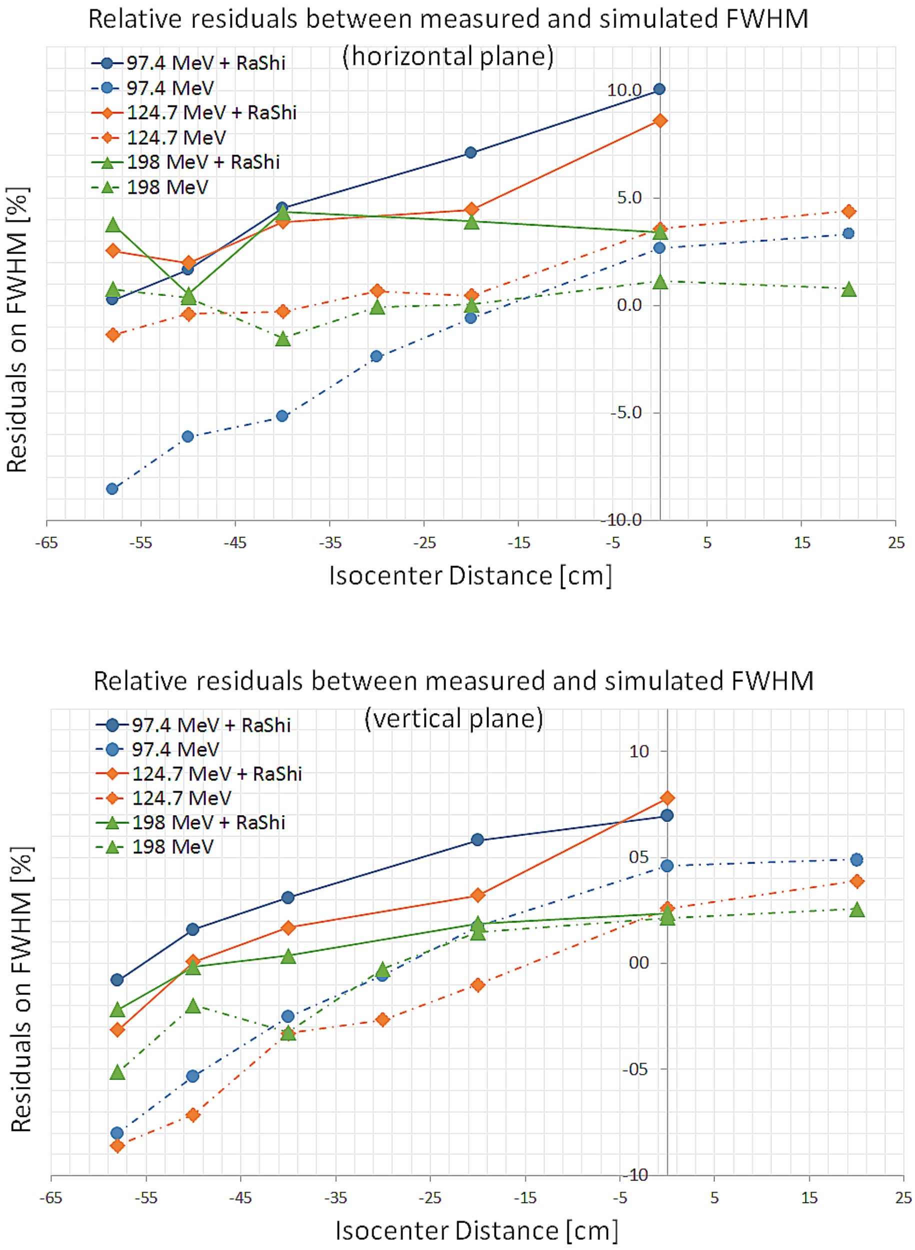

Figure 4.7: relative deviations in FWHM for 5 key energies at 7 air gaps for horizontal (above) and vertical (below) plane.

Depth dose residuals

Regarding depth dose profiles in water for open beam configuration, for all analyzed energies, the MC simulation reproduced the shape of the depth dose profiles measured in water accurately (see figure 4.8(a)). Integral dose normalized at the first measurement point, showed an agreement always within 1% (see figure 4.8(b)). Deviations always within 0.2 mm were found in terms of ranges as reported in figure 4.8(c). Absolute deviations in BPW80 were on average within 0.1 mm which corresponds to a relative deviation of about 3% (see figure 4.8(d)). Maximum absolute deviation observed was 0.3 mm (6%) at 169.3 MeV. Obtained deviations for depth dose profiles in water at ISD-50cm with RaShi in R80, R90 and Rp were never higher than 0.35 mm while mean integral dose deviations as well as the average peak-to-plateau differences were better than 0.4% (see figure 4.9).

Dose calibration results

For clarity, we report in table 4.2 the results of the beam model calibration in absolute dose, obtained by the simulation described in section 4.2.3. Differences between our calculated “mean stopping power” and ICRU stopping power data for the same proton residual range at the measurement depth were found up to 10.4% for a mono-energetic beam, with an expected energy dependent behavior. Indeed, ICRU stopping power data are provided for mono-energetic pencil beams, while the “mean stopping power” needs to account for the loss of primary protons as well as includes the nuclear secondaries at the measurement depth which is achieved by MC simulation. Our results are in agreement with Laitano et al. [157] and Gomá et al. [158]. The number of incident proton at nozzle entrance is used to normalize the DAP values. Deviations from the reported stopping power values may be found if the primary proton loss becomes large at reference depth (see figure 4.10). In this study, less than 1% and 0.54% proton loss was found at the phantom entrance and at the nozzle exit, respectively. The contribution of the nozzle to the primary fluence loss is in agreement with the 0.58% found by Grassberger et al. [136].

Dose evaluation in terms of DAP is shown in figure 4.11. A mean agreement of -0.1% between simulated DAP and measured DAP was found (maximum deviation observed is -0.5% at 62.4 MeV). The comparison to measured DAP is an internal consistency test of the correct implementation of the MC calculated values of the “mean stopping power” per incident proton. Indeed the MC results are used to establish the number of proton from DAP measurements; this calibration is then used to determine the DAP for a given number of protons and then compared with MC. The residuals shown in figure 4.11 are the result of the fitting of the calibration curve as we have observed before.

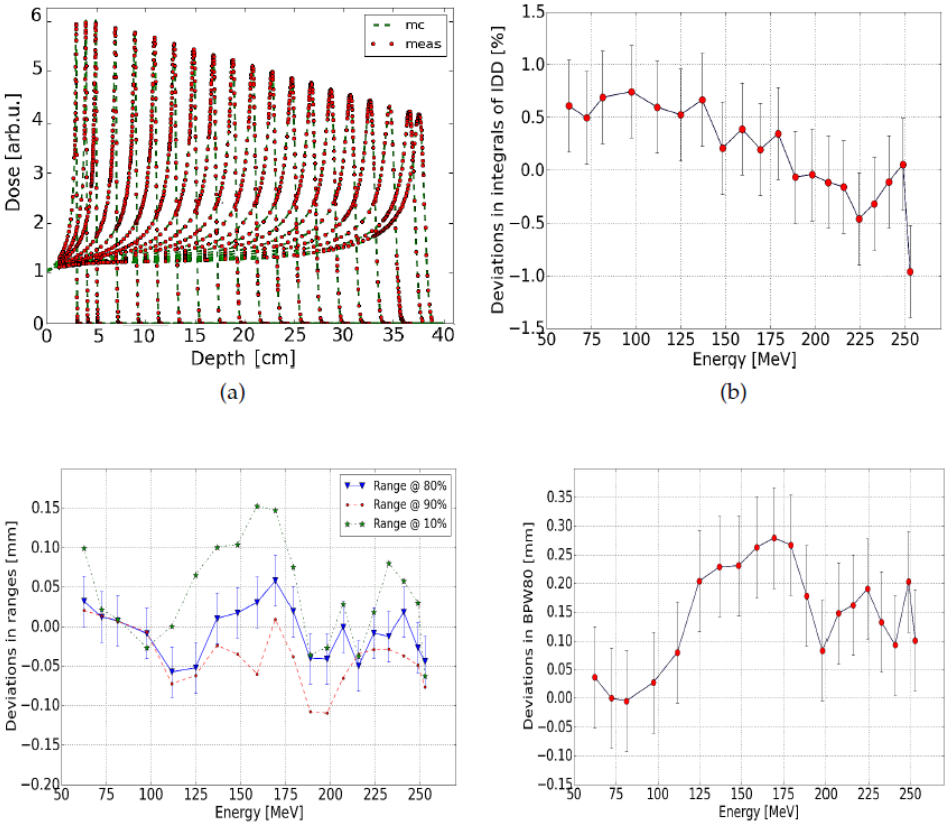

(a) (b)

(c) (d)

Figure 4.8: In figure 4.8(a) depth dose profiles simulated in water compared to measured profiles for 20 energies are shown. For this comparison, energy values deposited in the cylindrical volume representing the Bragg peak chamber of 4.08 cm radius was used. In figure 4.8(b) relative deviations between simulated and measured integral doses are shown. In figure 4.8(c) absolute deviations between simulated and measured ranges are shown while in figure 4.8(d) absolute deviations of Bragg peak width values at 80% dose level are reported. Error bars always correspond to the standard deviation. For sake of clarity, in figure 4.8(c) error bars are reported for only one set of deviations.

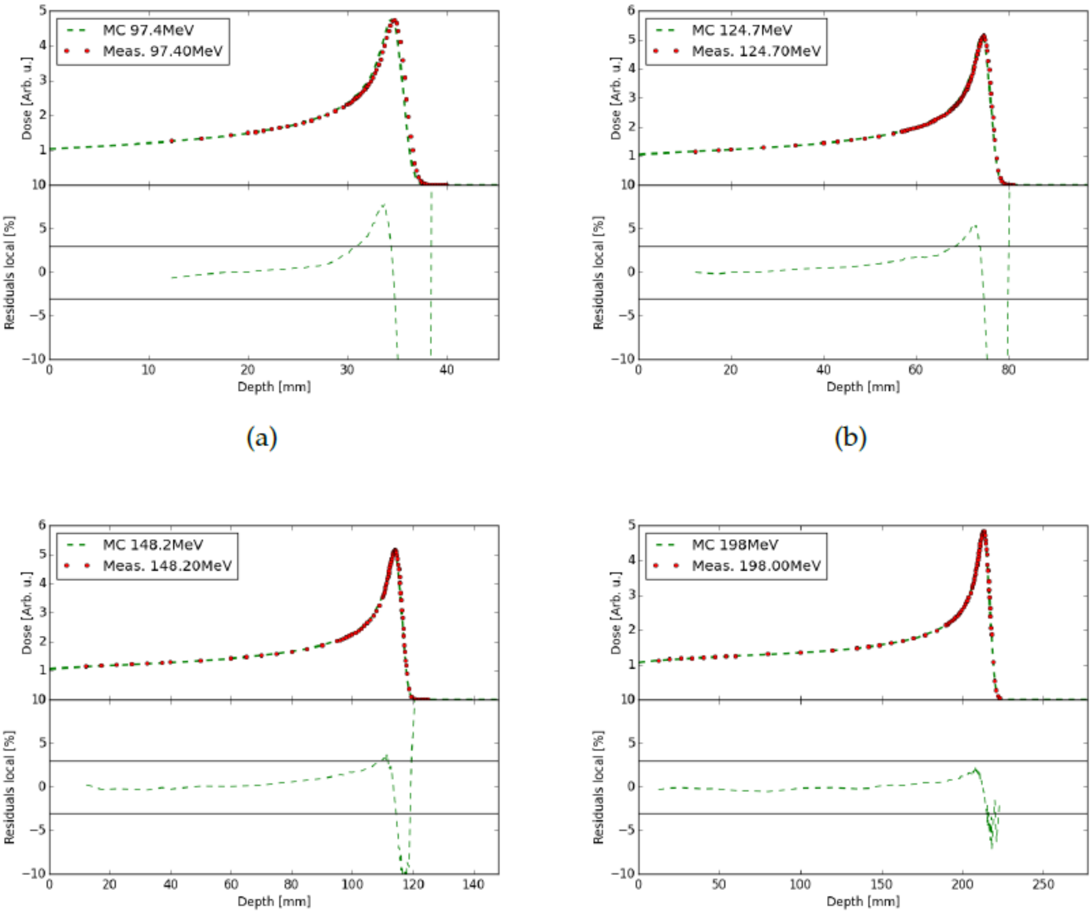

(a) (b)

(c) (d)

Figure 4.9: agreement between measured and simulated depth dose profiles in water with water phantom aligned at ISD+50cm with RaShi. Deviations are normalized at the reference position of 20 mm in depth.

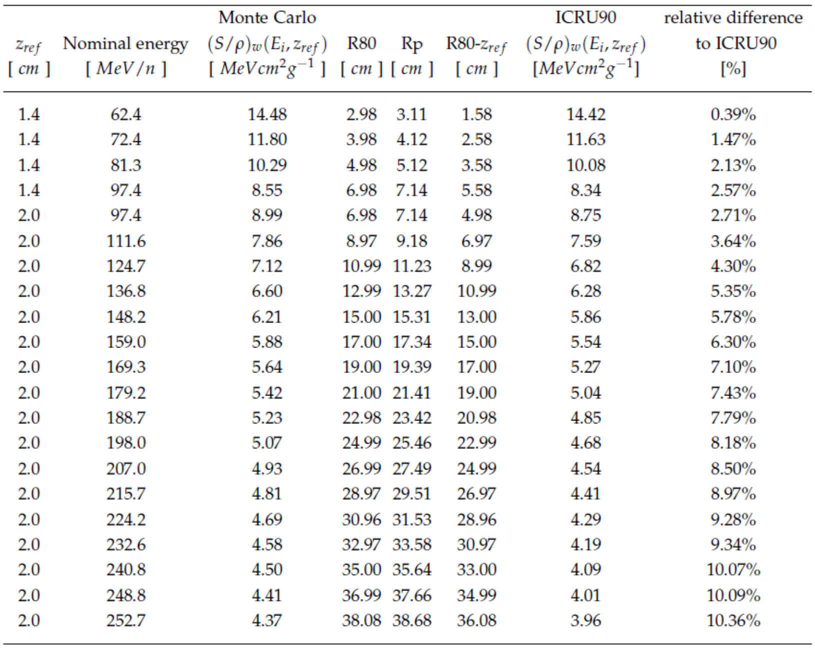

z_{ref} [cm]	Nominal energy [MeV/n]	Monte Carlo $(S/\rho)_w(E_i, z_{ref})$ [$MeVcm^2g^{-1}$]	R80 [cm]	Rp [cm]	R80-z_{ref} [cm]	ICRU90 $(S/\rho)_w(E_i, z_{ref})$ [$MeVcm^2g^{-1}$]	relative difference to ICRU90 [%]
1.4	62.4	14.48	2.98	3.11	1.58	14.42	0.39%
1.4	72.4	11.80	3.98	4.12	2.58	11.63	1.47%
1.4	81.3	10.29	4.98	5.12	3.58	10.08	2.13%
1.4	97.4	8.55	6.98	7.14	5.58	8.34	2.57%
2.0	97.4	8.99	6.98	7.14	4.98	8.75	2.71%
2.0	111.6	7.86	8.97	9.18	6.97	7.59	3.64%
2.0	124.7	7.12	10.99	11.23	8.99	6.82	4.30%
2.0	136.8	6.60	12.99	13.27	10.99	6.28	5.35%
2.0	148.2	6.21	15.00	15.31	13.00	5.86	5.78%
2.0	159.0	5.88	17.00	17.34	15.00	5.54	6.30%
2.0	169.3	5.64	19.00	19.39	17.00	5.27	7.10%
2.0	179.2	5.42	21.00	21.41	19.00	5.04	7.43%
2.0	188.7	5.23	22.98	23.42	20.98	4.85	7.79%
2.0	198.0	5.07	24.99	25.46	22.99	4.68	8.18%
2.0	207.0	4.93	26.99	27.49	24.99	4.54	8.50%
2.0	215.7	4.81	28.97	29.51	26.97	4.41	8.97%
2.0	224.2	4.69	30.96	31.53	28.96	4.29	9.28%
2.0	232.6	4.58	32.97	33.58	30.97	4.19	9.34%
2.0	240.8	4.50	35.00	35.64	33.00	4.09	10.07%
2.0	248.8	4.41	36.99	37.66	34.99	4.01	10.09%
2.0	252.7	4.37	38.08	38.68	36.08	3.96	10.36%

Table 4.2: summary of the "mean stopping power" calculated according to equation 2 for monoenergetic beam that have a projected range equal to the value of R80-z_{ref} of the modeled beam in water. The energy is provided at the nozzle entrance as well as the fluence of incident protons. The last two columns shows the ICRU90 stopping power for mono-energetic protons with the same projected range and the difference of those values from the "mean stopping power" per incident proton calculated here to illustrate the importance of taking the loss of primary protons and the production of secondary charged particle into account.

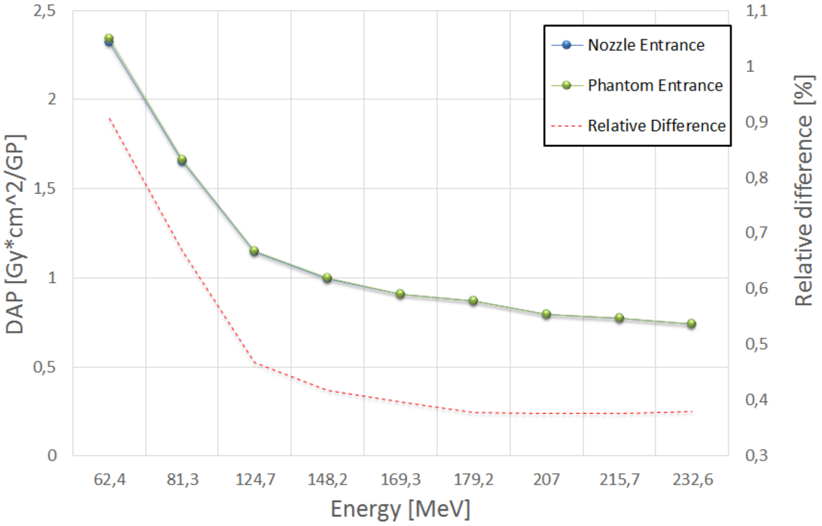

Figure 4.10: DAP calculated considering a 7 cm scoring radius for two different fluence, at the nozzle entrance and at the phantom entrance. Proton lost at the phantom entrance is up to 1% at 62.4 MeV.

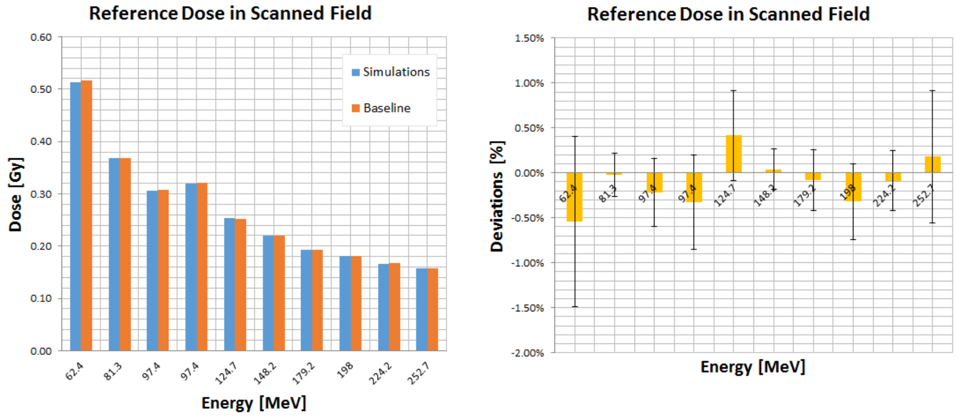

Figure 4.11: absolute and relative deviations in terms of DAP normalized to the delivered number of proton for a 2D scanned field 12x12 cm^2 and measured at the reference position of 14 and 20 mm in depth (depending on the energy). The error bar represents the standard deviation on the dose value calculated in the range of 1 mm from the reference position.

Box type	FS50 [mm]	LP80-20- [mm]	LP80-20+ [mm]
Box6(0,0,6)	0.3 (0.4%)	-1.0 (-11.4%)	0.0 (0.1%)
Box8(0,0,15)	0.3 (0.3%)	-0.2 (-2.4%)	-0.2 (-2.0%)
Box10(0,0,25)	0.1 (0.1%)	0.3 (1.1%)	0.2 (2.1%)
Box6(0,0,5) ISD-50cm+RaShi	1.0 (1.2%)	-0.4 (10.3%)	0.2 (-2.4%)

Box type	R80 [mm] (%)	R90 [mm] (%)	Rp [mm] (%)	MOD90 [mm] (%)	DP80-20 [mm] (%)
Box6(0,0,6)	0.0 (0.0%)	0.1 (0.0%)	-0.7 (-0.7%)	-1.0 (-1.5%)	-0.6 (-24.7%)
Box8(0,0,15)	0.0 (0.0%)	0.0 (0.0%)	-0.4 (-0.2%)	1.3 (1.4%)	-0.5 (-14.0%)
Box10(0,0,25)	-0.1 (0.0%)	-0.2 (-0.1%)	-0.4 (-0.1%)	2.1 (1.7%)	-0.5 (-9.0%)
Box6(0,0,5) ISD-50cm+RaShi	0.5 (0.6%)	0.7 (0.9%)	-0.2 (-0.2%)	0.8 (1.3%)	-0.5 (-16.0%)

Table 4.3: Deviations in water for the 3D dose distributions analyzed in terms of transverse parameters (above) and distal parameters (below) in absolute and relative terms. The LP80- 20- and the LP80-20+ are referring to the LP80-20 evaluated for the negative and the positive distance, respectively, from the center of the transverse dose profile.

4.3.2 Beam model validation

The agreement with measured transverse beam profile was mostly better than 0.4 mm. The FS50 and the LP80-20 agreed in average by 0.4 mm and -0.1 mm respectively. For the FS50, a maximum deviation of -1.0 mm (-11.4% in relative terms) was observed for the shallower target (95% dose level within 3 and 8 cm range) when the RaShi was used. Deviations for R80 and R90, initially found never higher than 0.2 mm, increase up to 0.5 mm and 0.7 mm respectively when a RaShi was used. A spread of 1.3 mm was found in the evaluation of the MOD90 over all the boxes, with a maximum deviation of 2.1 mm for the deepest target (95% dose level within 22 and 30 cm range). The DP80-20 was -0.3 mm in average with a maximum deviation of -0.6 mm. Evaluation in terms of distal as well as lateral parameters is summarized in table 4.3.

With respect to the dose analyzed according to equation 4.5 and equation 4.6, an initial dose difference of +2.7% was found in average. This dose difference was found consistent for all boxes and independent of the position (proximal or SOBP), air gap, box size and use of range shifter. Therefore a rescaling factor of -2.7% was applied. The reason for the systematic difference of about 2.7% initially observed in the 3D delivery is currently not fully understood. Part of the difference can be explained by differences between planned and effectively delivered number of particles. This contribution was found of 0.5% at maximum for middle energies but further studies are currently ongoing. Small inaccuracy in the characterization of the spray and halo regions may also have an impact. After rescaling, the largest deviation was

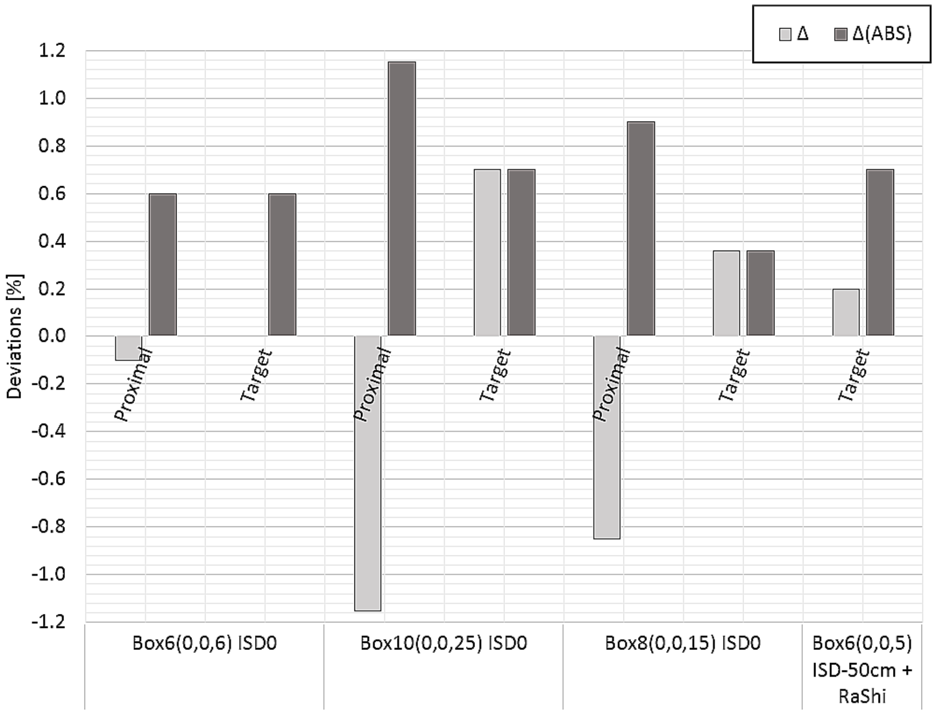

Figure 4.12: Local dose deviations evaluated according to equation 4.5 and equation 4.6 after rescaling of -2.7%.

-1.2% at the proximal position for the box10 (see figure 4.14). The beam model accuracy was not affected by the different air gaps or the use of the range shifter, which are known to be complex situations for conventional pencil beam algorithms. A maximum deviation of -0.2% was found in the SOBP for the non-isocentric box6 with RaShi. All the analyzed three-dimensional cases are shown in figure 4.13 and figure 4.14.

The presented analysis suggests the tendency of the MC simulation to slightly underestimate the dose in the plateau and to slightly overestimate the dose at the target.

4.4 Conclusions

A full nozzle beam modeling method for active scanning proton pencil beam has been proposed and validated for GATE/Geant4. This beam modeling method starts at nozzle entrance in order to take into consideration the spectra of secondary particles produced in the nozzle. The calibration of the beam monitors is based on a new formalism in dose-area-product and has been implemented for the first time. In addition, special care was taken in order to model the beam optics properties within

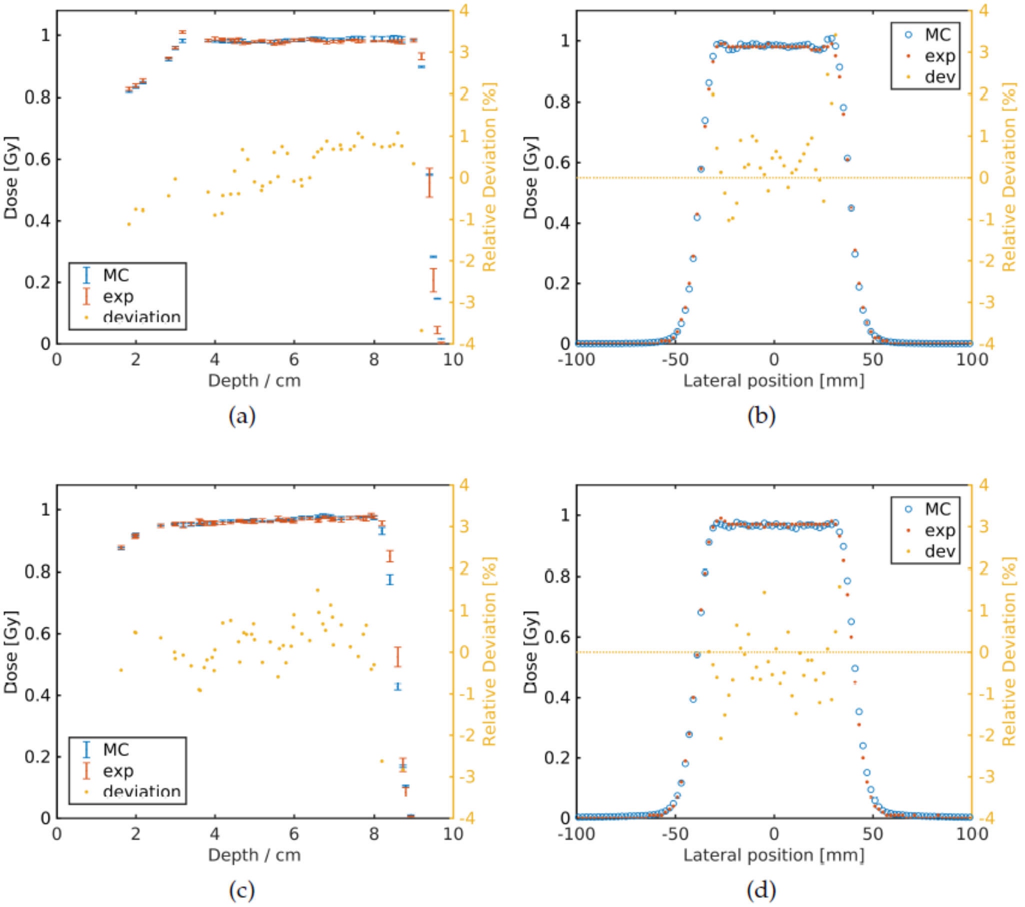

Figure 4.13: Longitudinal (a) and transverse (b) dose profiles for Box6(0,0,6) and longitudinal (c) and transverse (d) dose profiles for the Box6(0,0,5) placed at ISD-50cm with RaShi compared to measured data.

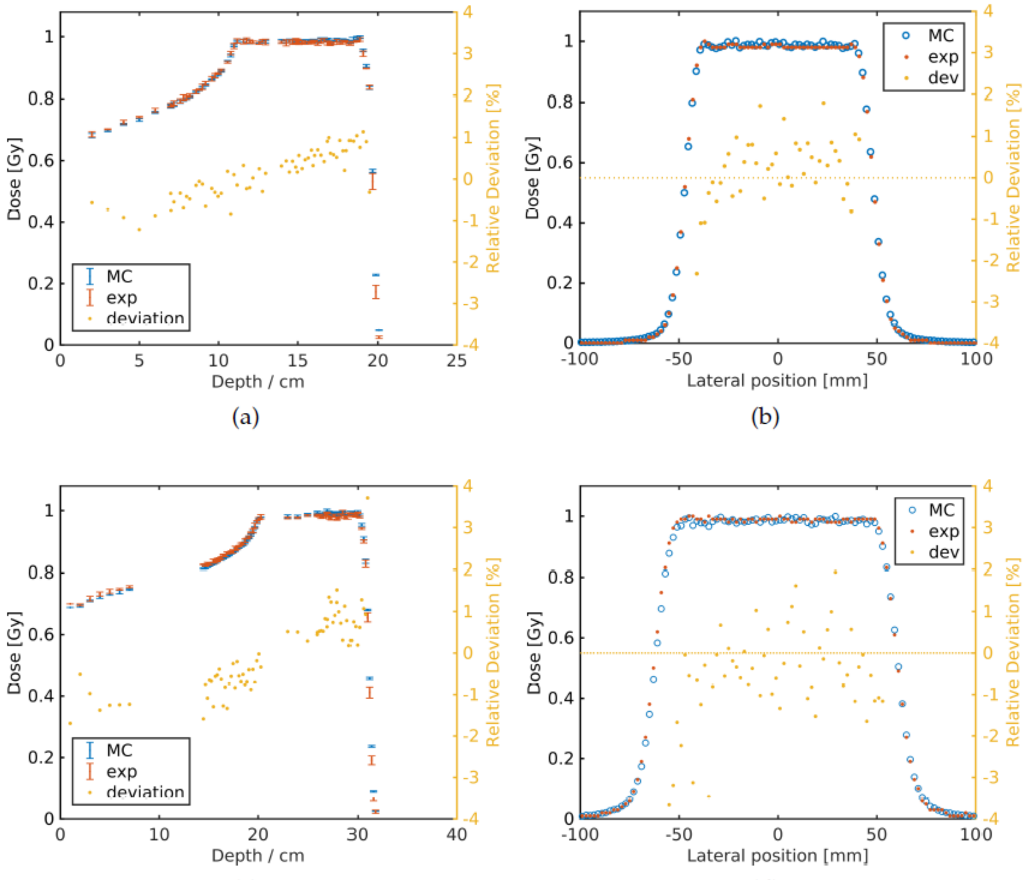

(a) (b)

(c) (d)

Figure 4.14: Longitudinal (a) and transverse (b) dose profiles for Box8(0,0,15) and longitudinal (c) and transverse (d) dose profiles for the Box10(0,0,25) compared to measured data.

clinical specifications at reduced air gaps, in order to support non-isocentric treatment delivery as routinely performed at MedAustron. The beam model provided in this manuscript is able to match spot FWHM values at isocenter and clinically relevant non-isocenteric positions in air within clinical requirements of 1 mm, 10%. Ranges are reproduced within 0.2 and 0.35 mm (max deviation) without and with range shifter, respectively. The dose difference in reference conditions is within 0.5%. Three-dimensional delivery was fully characterized by the evaluation of the dose at the target, dose in the plateau and typical parameters such as FS50, MOD90, DP80-20, LP80-20, R80, R90 and Rp. The agreement of distal and longitudinal parameters is mostly better than 1 mm. The detailed characterization of the pencil beam offered by GATE and the implementations of the full nozzle design in our simulations makes our calculations accurate, even in complex situations such as the non-isocentric patient positioning in presence of range shifter. The MC beam model has been validated based on commissioning measurements and will be inserted as a tool in clinical routine for independent dose calculation.

CHAPTER 5

Towards the implementation of GATE for independent dose calculation

The characterization of the physical properties of the proton pencil beam presented in chapter 4 represents the very first step towards the implementation of an IDC tool. After validation, also presented in chapter 4, it is important to move towards more clinical cases, in order to spot capabilities and limitations of the proposed model in a more clinical context. Eventually, the IDC needs to be properly integrated in the clinical workflow. For instance, the IDC should be interfaced to the treatment planning system (TPS) in order to easily exchange all the needed patient information in terms of DICOM files. In this respect, the workflow from the clinically commissioned TPS to the Geant4-based GATE MC dose calculation engine is presented in this chapter. An overview concerning the Patient Specific Quality Assurance (PSQA) performed at MedAustron is presented at first. Many details concerning the dosimetric specification and/or calibration of the detectors are presented in [144, 151]. Details concerning the commissioning of the equipment are available in [143].

5.1 Introduction

In a LIBT, a proper set of QA protocols guarantees not only the accuracy and the functionalities of the beam delivery system, but also ensures the safety of the clinical treatments. For particle therapy treatment, the plan verification (or PSQA), is usually performed for each beam delivered to the patients. The active delivery offers a highly conformal dose deposition to the target. As this technique is very sensitive to the treatment delivery uncertainties, the patient-specific plan verification is highly recommended in particle therapy and it must be inserted within the QA program. Although a direct verification of the delivered dose to the patient still represents a gold standard, a PSQA is typically performed in water, according to specific techniques which might differ from centre to centre. For instance, a PSQA measurement can be performed in a dedicated water phantom equipped with ICs as well as by mean of a 2D ion chamber array detector or by film measurements. The 2D ion chamber array detector provides, in addition to absolute dose measurements, 2D dose-distribution information [160]. The use of the 2D ion chamber array detector for PSQA is particularly suitable for irradiation at different beam angle (gantry irradiation). Film measurements are instead used to obtain planar dose distributions [161]. The method used at MedAustron is based on water phantom measurements, described in detail in section 5.2.1.

Currently, the PSQA protocol is the only possibility to check that the treatment plan can be delivered within clinical tolerances and it is legally taken into consideration. However, PSQA measurements performed in water (see section 5.2.1) cannot provide any input regarding the dose accuracy in the patient. Further, it necessarily requires considerable beam time that could be used for treatment otherwise. If properly implemented and validated, the IDC can provide a considerable support in this respect. The validation of the treatment plan calculated at the TPS could be performed directly via IDC, without even requiring a PSQA measurement. On the other hand, the implementation of an IDC into the clinics, requires a careful validation at every step of the clinical workflow.

In this chapter, major emphasis is given to GATE as an independent dose calculation tool implemented for proton therapy planning verification in water. The purpose is to illustrate the steps which are required for the clinical implementation of GATE into the clinical workflow used at MedAustron. In addition, it is important to remark that in order to substitute the TPS patient verification with the IDC, we must guarantee that the IDC can match the measured data with, at least, the same accuracy of the TPS.

5.2 Material and method

In clinical practice, several techniques exist to perform a patient specific quality assurance, depending for example on the preferred equipment [160, 161, 162, 163, 164]. At MedAustron, the 3D detector block (described in section 4.2.1) equipped with 24 PinPoint is implemented for PSQA according to the shared experience of GSI, HIT and CNAO [151, 165]. The methodology as well as the measurements are described in section 5.2.1 respectively. The dedicated MC workflow to reproduce the PSQA in GATE is described in section 5.2.2.

5.2.1 PSQA at MedAustron

Once the clinical plan is approved by the radiation oncologist, the medical physicist proceed with the preparation of the PSQA at the TPS (RayStation). The experimental setup reproduced at the TPS consists in an homogeneous water box with a scoring grid of 2 mm voxel size. A gap of 24.2 cm is inserted in the TPS to position the water box in order to consider the alignment of the MP3-P at ISD-40cm in the IR. The TPS calculates the dose distribution in the water phantom according to the treatment plan. For the calculation, the same machine parameters as for the clinical plan are used. Typical parameters are the number of layers, number of spot, the spot spacing distance, energy layer distance, and the spot weight. It is crucial to use the same calculation settings as well as the same number of particles for each irradiation of the clinical plan in order to spot eventual errors as well as interlock during the delivery.

After calculation, the TPS allows the user to export the DICOM DOSE file of the PSQA. At MedAustron, a specific python tool which allows the user to extract the dose in specific points of the dose distribution was developed [151]. The tool facilitates the extraction of dose values in a wanted position of the water phantom (see figure 5.1) [151]. The dose for each of the 24 PinPoint is saved in a dedicated file (PSQA init-file) together with the coordinates of the position chosen for the measurement. The PSQA init-file is then used as input to a software (PlanVerificator v1.0) which is interfaced to the equipment during the measurements and it remotely moves the detector at the wanted position [151]. The PlanVerificator software facilitates the measurement acquisition, the dose comparison between TPS and measured values and the creation of clinical PSQA reports [151]. The corrections briefly described in section 2.4 are automatically taken into consideration and applied on-line during measurements.

The technique used at MedAustron for treatment plan verification follows a similar approach as the one described in section 4.2.2 with respect of the three-dimensional regular-shaped dose distribution in water exploited for validation of the MC beam model. The 3D water phantom is the MP3-P water phantom (PTW, Freiburg) is mounted directly on the couch (see figure 5.2). The alignment is performed automatically by the PAS which takes advantage of a tracking camera on the floor to perform corrections. The reference in the alignment process is represented by the laser system of the IR.

The 3D block is moving according to a specific reference system build upon longitudinal, vertical and lateral coordinates (A,B,C) with respect to the beam direction. If needed, the holder can be rotated by 90° and be used for vertical beam line irradiation with corresponding rotation of the reference system. The 3D block is manually aligned according to the lasers of the IR (see figure 5.2). The ionization chambers are supplied by two PTW-10004 MULTIDOS 12-channel electrometers, a control unit and a ComServer. The two 12-channels Multidos electrometers provide a fix high voltage supply of +400 V. A Control Unit (TBA Control Unit) controls the

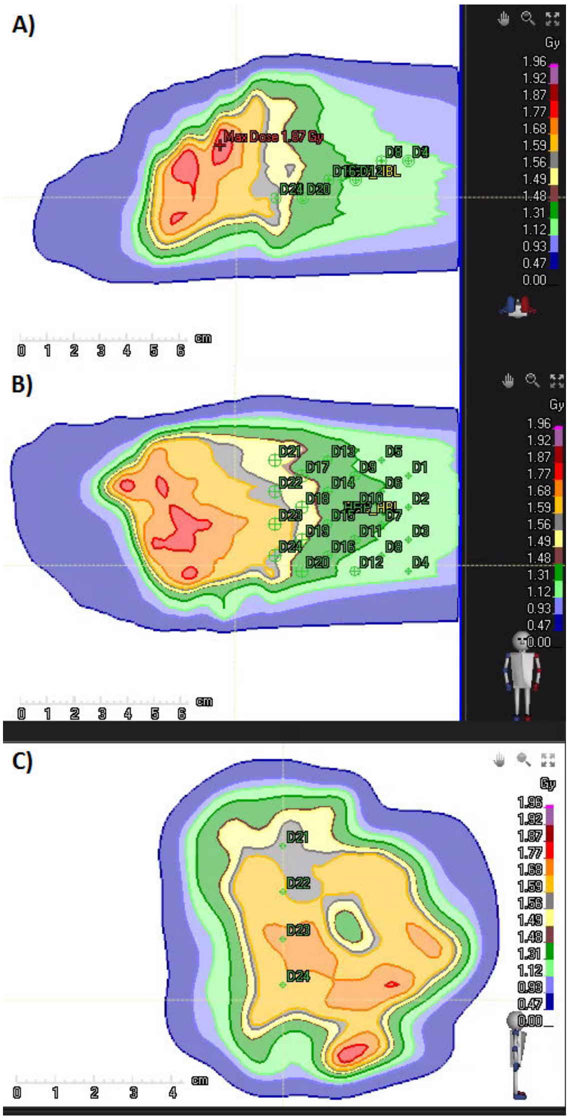

Figure 5.1: example of a PSQA preparation at the TPS. In A) B) and C) the transversal, coronal and sagittal view of the dose distribution calculated by the TPS, respectively. The 24 PinPoint of the 3D detector block is displayed in each view. For each of the IC, the TPS provides the dose values to be compared to the measurements and the values for the dose gradient in Gy/mm.

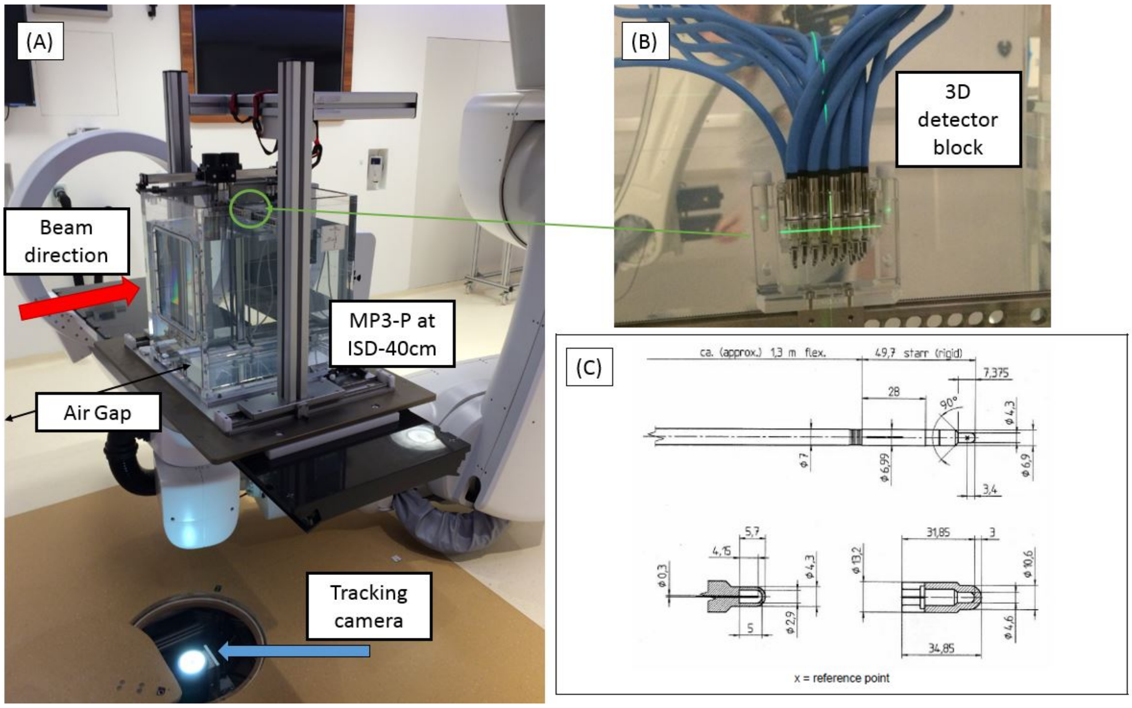

Figure 5.2: picture of the setup used at MedAustron for PSQA measurements (A). The MP3-P is mounted on the in-room couch and moved by the PAS system. In (A) is also visible the tracking camera on the floor responsible of millimetrical correction. In the picture (B) the 3D block holder with the 24 PinPoint chambers in place aligned to the in-room laser system [166]. The technical drawing of a PinPoint chamber PTW TM31015 is reported in (C) [167].

moving mechanism that positions the 3D detector block in the water phantom. The resolution of the system is 0.1 mm in the three dimensions. The PinPoints mounted in the 3D block are placed in such a way to avoid shadowing effect between each other during the irradiation (see figure 5.2). The volume of the PinPoint chambers is designed to provide quasi-punctual measurements at high resolution, with 0.03 cm^3 of sensitive volume for a radius of 1.45 mm and a length of 5 mm, as reported in figure 5.2-(C) [167].

In order to choose an optimal position for the 3D block during the preparation of the PSQA at the TPS, it is important to take into consideration the dose gradient for each of the PinPoint. For the evaluation of the PSQA, the following definitions are introduced:

$$\bar{\xi}^{TPS} = \frac{1}{N}\sum_{i}^{N}\frac{(D_i^{meas} - D_i^{TPS})}{D_{MAX}^{TPS}} \tag{5.1}$$

$$\bar{\xi}^{TPS}_{ABS} = \frac{1}{N}\sum_{i}^{N}\frac{|D_i^{meas} - D_i^{TPS}|}{D^{TPS}_{MAX}} \tag{5.2}$$

$$\xi_i = \frac{(D_i^{meas} - D_i^{TPS})}{D^{TPS}_{MAX}} \tag{5.3}$$

where the N is the total number of PinPoint chamber considered for the measurement, D_i^{meas} and D_i^{TPS} is the measured and planned dose respectively, and D^{TPS}_{MAX} is the maximum planned dose over the entire dose distribution of one irradiation. The acceptance criteria for the tested plan is defined as the following:

$$\begin{gathered}\bar{\xi}^{TPS} \pm SD(\bar{\xi}^{TPS}) \leq 5\% \pm 5\% \\ \bar{\xi}^{TPS}_{ABS} \pm SD(\bar{\xi}^{TPS}_{ABS}) \leq 5\% \pm 5\% \\ \xi_i \leq \pm 7\%\end{gathered} \tag{5.4}$$

where the term SD indicates the standard deviation. The deviations observed at the i-th position which has a dose gradient higher than 0.04 Gy/mm are not considered as a small inaccuracy in the positioning of the IC would results in a high uncertainty in dose. These points are excluded from the analysis. Variation up to 7% on one single chamber is tolerated as described by the last equation of the criteria 5.4. However, the average on the agreement between measured and calculated dose must fulfill the 5% requirement. If the acceptance criteria is not fulfilled, the medical physicist should investigate the reasons of discrepancy and consider several options like re-planning.

5.2.2 The workflow concept

The concept of the workflow used to re-produce the PSQA verification with GATE is represented in figure 5.3. The workflow of figure 5.3 is a high-level description for any plan recalculation with GATE. Each step of the workflow relies on several subprocesses which are characterized and implemented at MedAustron in the context of this PhD, as described in the following.

TPS level

At this level the treatment plan is prepared at the TPS. Via export of the DICOM files, all the important patient-specific information are stored. In general, DICOM RT objects collected from the TPS and needed by the GATE simulations are:

- RT IMAGE: it contains data related to the CT of the patient;
- RT PLAN: it contains a description of the plan to be delivered;

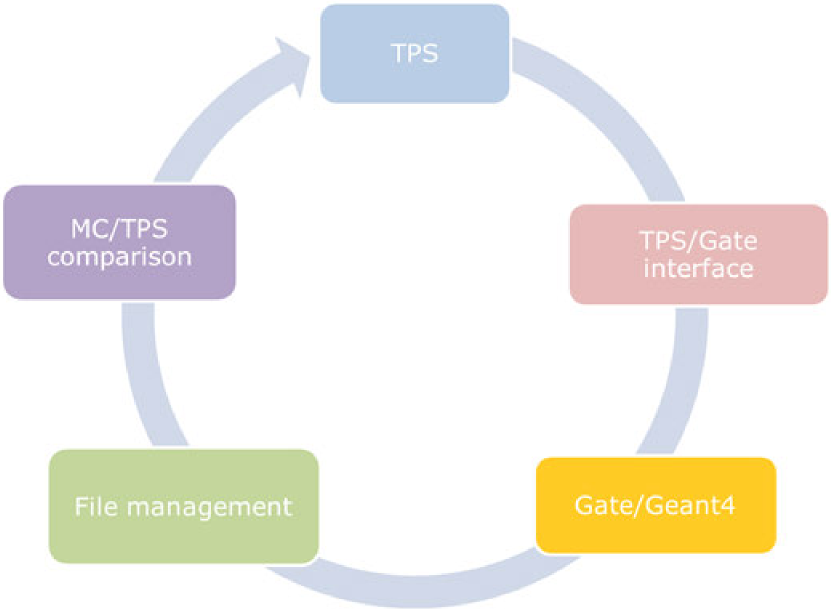

Figure 5.3: set of basic steps required for a full GATE recalculation of a treatment plan.

- RT STRUCTURE SET: it contains the description of all the target contours such as the GTV, the CTV and the PTV drawn on the CT but also all the important OARs;
- RT DOSE: it contains data related to the calculated dose distribution, generally computed as a 3D matrix, in the coordinate system of the CT image.

TPS/GATE interface level

During this step, it is performed a conversion of the exported DICOM file into a file format readable by GATE. The type of the file format required by GATE is a function of the DICOM type. For example, the DICOM RT PLAN is converted into an ASCII file while the DICOM RT IMAGE is converted into an mhd-image file.

GATE/Geant4 level

This step represents the MC recalculation. To properly arrange the MC simulation, a set of input is required by GATE. In particular, the physical characterization of the pencil beam (chapter 4) must be provided as input as well as the description of the treatment head and the CT calibration curves [168, 169].

File management level

At this level some post-processing on the GATE output file is needed according to the user needs. A typical option would be to convert the dose output files of GATE (mhd-image for example) into a new set of DICOM files.

MC/TPS comparison

This step represents the MC and the TPS comparison of the obtained results in terms, for example, of a 2D γ-index. At the end of the workflow, it might be useful for further evaluation and/or reporting to import the MC DICOM files directly in the TPS, as represented in the very last step of the figure 5.3.

The presented workflow applies to the PSQA procedure with few simplifications. Once the set of positions and dose values for each PinPoint are stored in a dedicated file to perform the measurement, the medical physicist can decide to reproduce the verification with the IDC and to begin with the first step of the workflow. In this case, the QA plan calculated at the TPS is exported in DICOM format containing all the necessary information to reproduce in GATE the PSQA for that specific clinical case.

For the purpose of a PSQA the DICOM RT IMAGE and the DICOM RT STRUCTURE SET can be ignored. The DICOM RT DOSE files are usually a set of two different types: BEAM and PLAN type. The BEAM type file contains the dose matrix of the single irradiation while the PLAN type is the dose calculated for the entire plan[1].

An automatized tool developed in house in the context of this PhD project is driving the user through each of the step of the workflow, taking care of converting the required information in a format that can be handled by the GATE TPS source [134]. Particularly, the tool exploits several routine available with the CLITK package[2] and performs a conversion from DICOM file to a format readable by GATE (ASCII file for instance). The converted output files provided by CLITK are provided in a specific format handled by GATE by dedicated functions in its source code and accessible to the user [134]. The tool automatically assigns most of the common MC parameters, according to the studies and the results presented in chapter 4. A fix number of primaries of 10^7 is selected. The simulations is then run on 10 different cores for a total of 10^8 primaries. The setup described in section 5.2.1 is reproduced. In particular, the water phantom is modeled as a water box placed at ISD-40cm i.e. considering the 34.2 cm air gap from the nozzle exit window to the water phantom surface. The geometry of the 3D block as well as of the PinPoint is omitted. A scoring grid of 2 mm voxel size is used. After the calculation of the MC-PSQA, the user can require a conversion of the GATE output file in DICOM

---

[1] A DICOM RT DOSE PLAN file might not correspond to the full clinical prescription, but only to a part of it, referred to as BEAM SET.

[2] https://www.creatis.insa-lyon.fr/rio/vv

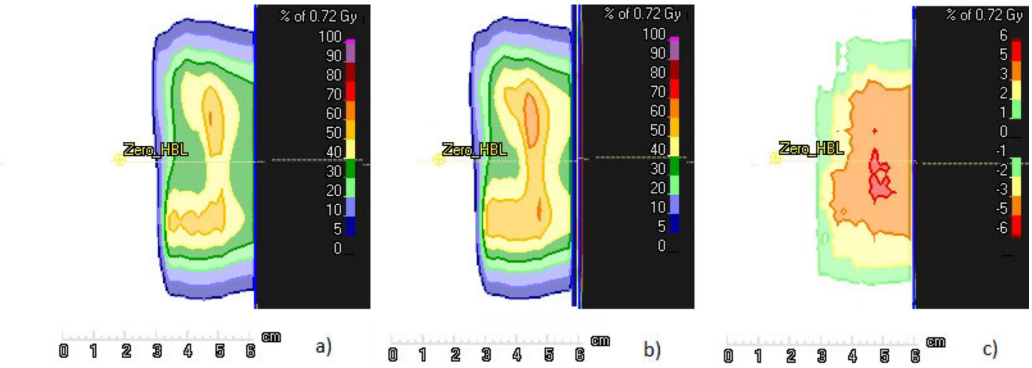

Figure 5.4: example of a comparison between TPS dose distribution (a) and a MC dose distribution (b). Difference between (a) and (b) is reported in (c). In order to emphasized the differences between MC and TPS calculation (pencil beam algorithm), a particular clinical case is chosen: shallow target where the use of a RaShi is required (maximum beam range of about 3 cm).

format. The difference in the new set of DICOM file prepared by the tool is the content of the DICOM RT DOSE. Indeed, the dose matrix containing initially TPS dose values is now substituted with the MC dose. A final comparison between the initial dose distribution predicted by the TPS and the one calculated by GATE can be executed directly at the TPS as shown in figure 5.4 or, alternatively, with an external software. Eventually, as dose measurements are available for TPS PSQA verification, the same data can be used for further evaluation of the GATE dose distribution.

5.2.3 Clinical case selection and evaluation of the GATE-PSQA results

The evaluation proposed in this study has a double purpose: on one hand to support the implementation of GATE towards more clinical cases; on the other hand, it serves as a validation of the presented workflow chain. For the evaluation of the PSQA plans recalculated by GATE, we selected three different clinical cases: a clival chordoma of the brain (CNS tumor), a carcinoma of the palate (para-nasal tumor) and a prostate carcinoma. The Planning Target Volume (PTV) for the CNS, the para-nasal and the prostate case has a size of 166.17, 150.31 and 302.16 cm^3, respectively. Depending on the beam angle chosen for irradiation, the location of the PTVs ranges between 3 cm (proximal) and 22 cm (distal) in depth. For the CNS case, the pencil beam algorithm v4.1 is selected for optimization. The MC algorithm v4.0 available in the TPS is selected for the para-nasal and prostate cases[3].

---

[3] At MedAustron, all the clinical plans are optimized before approval by the MC algorithm available in the TPS since RayStation version 6.0.

Clinical case	$\bar{\Delta}^{TPS} \pm SD(\bar{\Delta}^{TPS})$	$\bar{\Delta}^{GATE} \pm SD(\bar{\Delta}^{GATE})$
CNS	-0.5%±2%	0.2%±1.7%
Para-nasal	-0.6%±1.5%	-0.6%±1.5%
Prostate	0.8%±1.5%	-0.4%±1.2%
Para-nasal-RaShi	-1.6%±1.1%	-1.5%±1.1%

Table 5.1: analysis performed for the 4 cases to equation 4.5 for TPS and MC values, respectively.

As the PSQA is performed for each irradiation, every single field is simulated and compared to measured data. For the analysis of the results, we used a similar approach to the presented PSQA procedure for data analysis. The analysis performed for the simulations is described by the equations 4.5 and 4.6 presented in section 4.2.4. The same analysis is performed on the TPS calculation, with a different notation in the formulas 4.5 and 4.6 whenever the TPS dose values are used. It is important to remark the difference between the equations 5.1 and 5.2 to equations 4.5 and 4.6. Between the two pairs, the reference as well as the normalization is different. Indeed, the purpose of equations 5.1 and 5.2 is to validate the measurement against the TPS calculation. The normalization to the maximum planned dose serves to minimize high local deviations occurring in low dose regions, clinically not interesting. For consistency to the clinical approach presented in section 5.2.1 and to avoid not-significant outliers, the points with a dose gradient higher than 0.04 Gy/mm or with an expected dose lower than 0.1 Gy are excluded from the analysis.

A γ-index test with a pass-rate of 1mm/1% and 2mm/2% is performed to compare the local dose difference between GATE and the TPS dose distribution with suppressed dose below 1% for each beam. To assess any statistically significant deviation between TPS, GATE and measurements, the Wilcoxon paired signed rank test [172] with a significance level set at 5% is performed for each clinical case. The normality of each distribution is tested via the Shapiro-Wilk test [170, 171]. The valid data set consist of 219 dose measurement for the CNS case, 93 dose measurements for the prostate case and 97 dose measurements for the para-nasal case. In particular, for the para-nasal case, the RaShi was used for half of the irradiation. Therefore, this set of data is further divided into two sub-groups of 51 and 46 dose values with and without RaShi, respectively.

5.3 Results and discussion

In most of the analyzed cases, the comparison between measurements and GATE showed a very similar trend as the comparison between TPS and measured values (see figure 5.5). Overall, for all the analyzed cases, the GATE results match with the measured data as summarized in table 5.1 and table 5.2. Similar results have been

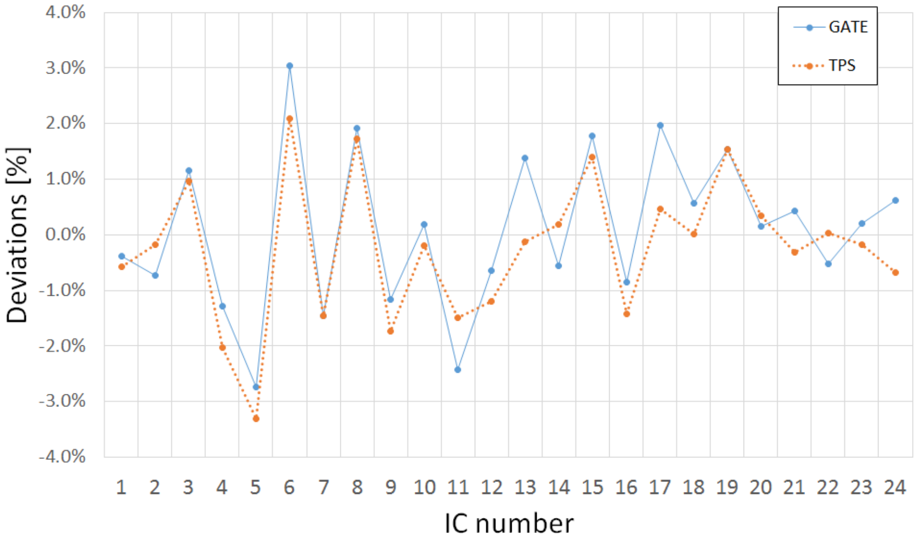

Figure 5.5: example of a comparison TPS-measurements and GATE-measurements for one of the irradiation of the CNS case showing how the independent system MC-based follow a very similar trend to the clinically used TPS.

Clinical case	$\bar{\Delta}^{TPS}_{ABS} \pm SD(\bar{\Delta}^{TPS}_{ABS})$	$\bar{\Delta}^{GATE}_{ABS} \pm SD(\bar{\Delta}^{GATE}_{ABS})$
CNS	1.4%±1.5%	1.1%±1.2%
Para-nasal	1.2%±1.0%	1.3%±1.0%
Prostate	1.1%±1.3%	1.0%±0.8%
Para-nasal-RaShi	1.6%±1.0%	1.6%±0.8%

Table 5.2: analysis performed for the 4 cases according to equation 4.6 for TPS and MC values, respectively.

obtained with the TPS, independently from the clinical case or the dose algorithm selected at the TPS. Maximum local deviation observed were found in the prostate case for TPS (8.7%) and in the CNS case for GATE (8.0%). Despite the filtering applied on the set of data in terms of dose gradient and low dose allowed, an outlier of about -15% was found in the CNS case for the TPS prediction. A similar situation was found for both dose engine in the para-nasal case. The outlier in the CNS case was considered not significant for two reasons: on one hand, this particular point correspond only to the 7.7% of the 1.34 Gy maximum dose calculated over the entire dose distribution predicted by the TPS for this particular beam. On the other hand, a high dose gradient region was found in the range of the considered point (from 0.038 up to 0.1 Gy/mm) which makes questionable the measured dose at that point. The outlier observed in the para-nasal case was found to be a similar combination of high dose gradient region and low dose values: about 10% of the maximum dose (1.77 Gy) in 0.039 Gy/mm. In order to avoid outliers due to combined effect of low dose values in the high gradient region, it could be useful the application of dynamic filters on the data set instead of absolute ones. For example a filter on the data points with dose values lower than 10% of the maximum dose, instead of an absolute filter (0.1 Gy in this case) can further avoid not significant outliers in the analysis of the deviations normalized at the measurement point. A different normalization, for example to the maximum of the measured values in a particular position, might also straiten this effect.

With respect to the irradiation when the RaShi is considered, a systematic deviation of -1.5% was found in the average in the GATE calculations. A similar deviation was observed in the calculation provided by the TPS. This offset was found to be independent from the particular dose gradient at the measurement point (see figure 5.6). The figure 5.6 shows the influence of the gradient on the magnitude of the local deviations observed for open beam measurements, with an evident spread starting around the 0.04 Gy/mm dose gradient value. On the contrary, no dependency was observed when the RaShi was considered. The agreement between the two different dose engines suggests an intrinsic limitation of the MC model which currently is not fully understood. According to the Wilcoxon paired signed rank test, this deviation is not considered statistically significant. However, to better understand this behavior it might help to increase the sample size i.e. to study further clinical cases, considering the influence of the beam incident, the size of the target and the distribution of the spot weight as a function of the energy.

The γ-index analysis performed on GATE and TPS distributions is summarized in table 5.3. Overall, a 85.7% and 98.1% pass-rate at 1mm/1% and 2mm/2% was found in average, respectively. The obtained results showed higher deviations comparing GATE and TPS in the prostate case when a finer pass-rate was used. This result may support the hypothesis that for small deep-sited target the GATE simulations might reproduce the behavior observed during the dosimetric validation presented in section 4.3.2 for the box10.

According to the Shapiro-Wilk test, the normality of the MC values Δ^{MC} and

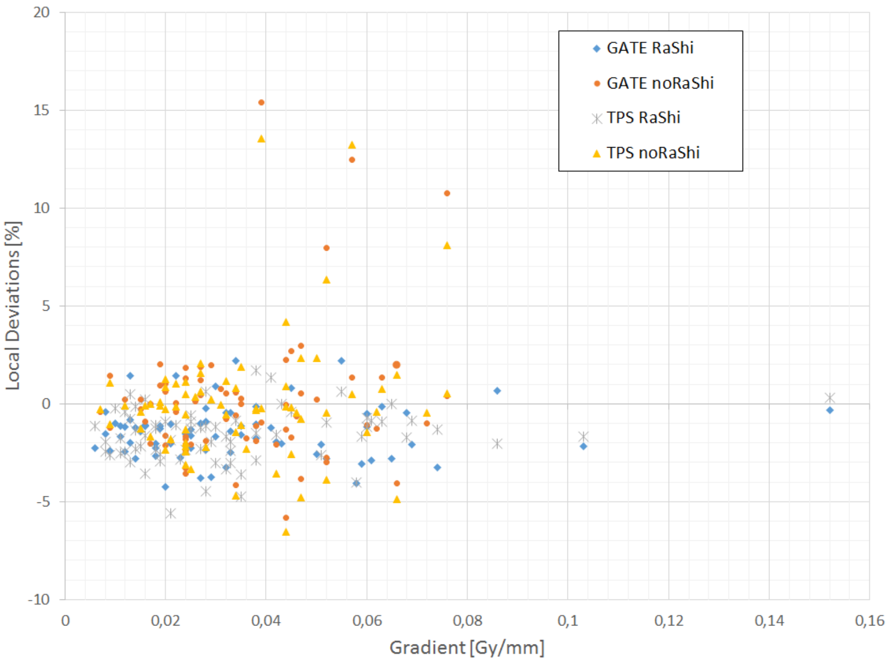

Figure 5.6: local deviations from measured data calculated by TPS and GATE as a function of the dose gradient at the measurement point. In this plot, the entire data set is considered (neither filtering based on the gradient value nor on the expected dose is applied).

TPS values Δ^{TPS} could not be guaranteed within the significance level of 5% (p-value<0.05) for every analyzed case. If the non-normality of the data is more obvious for the para-nasal due to the sample size, for the CNS and the prostate case is mostly linked to the presence of outliers as well as a right-skewness found in the distribution of the data set (see figure 5.7). The right-skewness behavior of the distributions might be attributed to hidden correlation between measured and calculated quantities. On the other hand, this behavior might also be attributed to a residual of the -2.7% re-scaling factor applied during the validation and commissioning processes. The Wilcoxon statistical test was used to assess statistically significant differences between every pair of distributions i.e. MC values and measured data, TPS values and measured data, TPS values and MC values. None of the analyzed cases failed the test (p-value always greater than significance level of 5%) meaning that the analyzed samples are statistically equivalent.

5.4 Conclusions

The PSQA technique as well as the PSQA equipment used at MedAustron have been presented. A MC-workflow concept was described in order to present the re-

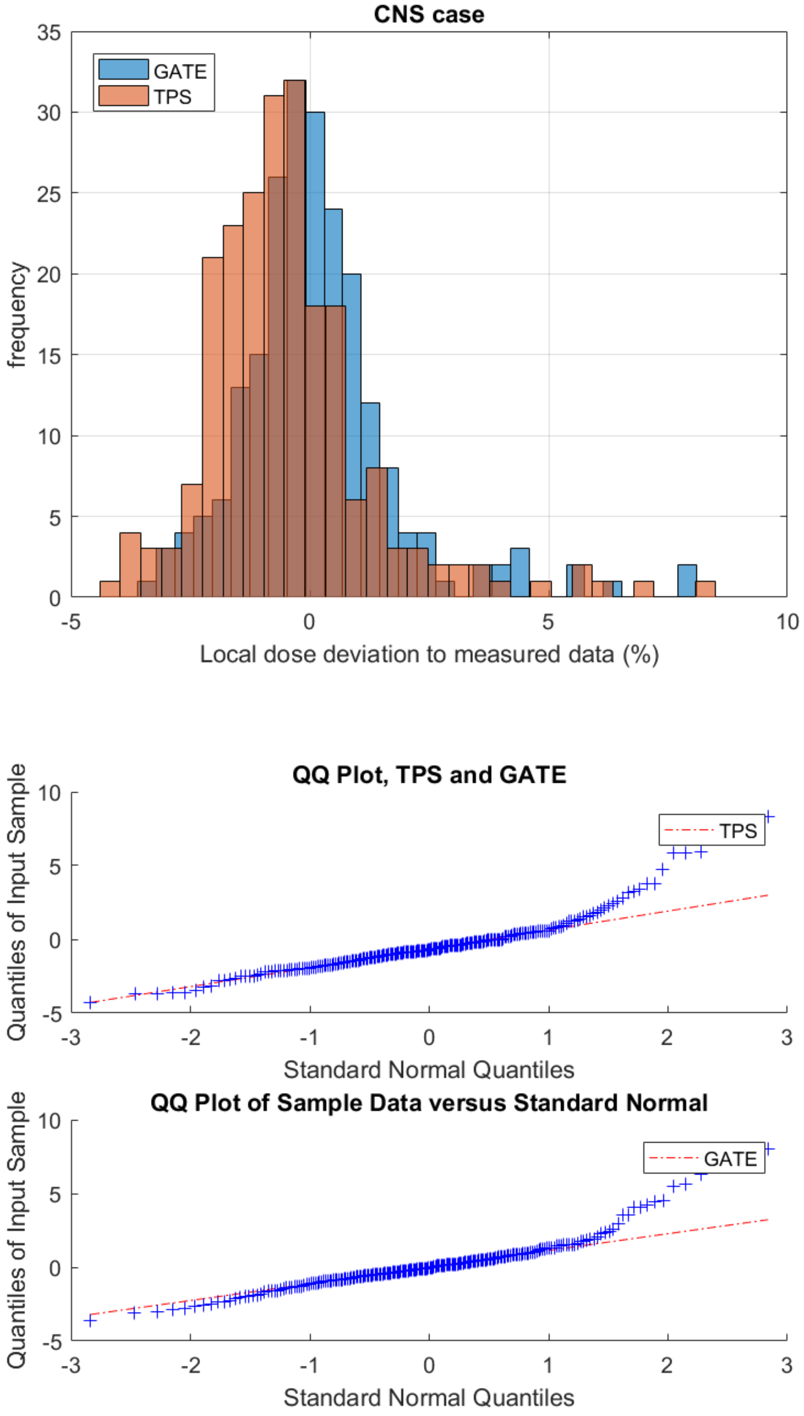

Figure 5.7: the skewness of the distribution of the data set is shown in the histograms plot (above) for Δ^{MC} and Δ^{TPS} values evaluated for the CNS case. To better display the slightly right-skewness for both TPS and MC data set, the Q-Q plot is also reported (below). For clarity purpose, the outlier of -14.7% found with TPS dose distribution is not reported in these graphs.

Clinical case		pass-rate 1mm/1%	pass-rate 2mm/2%
CNS	*min*	84.0%	97.8%
	max	93.2%	100.0%
	average	88.5%	99.0%
Prostate	*min*	66.7%	95.0%
	max	72.8%	99.5%
	average	70.7%	95.9%
Para-nasal	*min*	89.4%	97.6%
	max	92.5%	99.1%
	average	91.0%	98.4%
Para-nasal-RaShi	*min*	92.4%	99.0%
	max	93.4%	99.5%
	average	93.0%	99.2%

Table 5.3: γ-index analysis performed on each dose distribution calculated by the TPS and GATE.

calculation of a treatment plan via GATE calculation. The presented MC-workflow was successfully applied to the PSQA procedures which have been reproduced in GATE. Results have been compared to measured data as well as to TPS predictions. The local deviations between GATE and measured data follow in many cases the same trend of the deviations found for the TPS values. The impact of high dose gradient values must be carefully correlated to the obtained results, especially when measuring in low dose regions as it might lead to suspicious outliers. Overall, GATE and the TPS provided statistically equivalent results. A -1.5% deviation from measured data was found in average for both TPS and GATE when the RaShi was considered. Further clinical cases must be considered in future in order to increase the sample size of the data. In addition, new parameters such as the beam incident and the impact of irregular target can be inserted in the validation process of GATE as IDC.

CHAPTER 6

Conclusion

In this PhD, an overview of the proton therapy treatments was presented, with emphasis on the importance of Monte-Carlo simulation for independent dose calculation (IDC). Based on the MedAustron accelerator specifications, a detailed Monte-Carlo modeling of the physical properties for a proton pencil beam was proposed and evaluated. The presented beam model considers the full nozzle design, meaning that the source is described at the nozzle entrance. This choice, represents a significant difference with the current literature, where a modeling method from the nozzle exit was usually exploited.

The current clinical practice at MedAustron, explicitly required particular attention to the validation procedure in non-isocentric condition. The clinical treatments are routinely delivered moving the patient towards the nozzle, which is a rather uncommon clinical practice to reduce the lateral penumbra of the pencil beam. The non-isocentric setup increases the treatment complexity and is a unique feature of MedAustron. A 3D dosimetric validation under non-isocentric conditions with and without the use of a range shifter was therefore a mandatory requirement. The dosimetrical accuracy achieved by the beam model reached a maximum deviation of -0.2% in the SOBP to measured data for the non-isocentric regular shaped three-dimensional dose distribution with the use of a range shifter. The largest deviation of -1.2% was found at the proximal position for the largest cubic dose distribution.

Considering the nozzle design in the simulation inevitably lead to higher computational time (about 20%). On the other hand, the presented beam model ensures the clinical requirements of accuracy according to the MedAustron specifications and it allows the characterization of the spray as well as of the low dose penumbra as presented in details in a separate study called “Validation of electromagnetic and nuclear scattering models in GATE/Geant4 for proton therapy" [173].

The calibration of the beam model in absolute dose represents another key topic. Typically, absolute calibration of the delivery system is performed in number of particles and its interpretation in monitor units terms. In this work, we presented the implementation of the beam model calibration in reference condition using a newly developed formalism based on Dose-Area Product (DAP) measurements [131]. To our best knowledge, this was the first implementation of the DAP formalism in clinical practice. Noteworthy, this part of the presented work, was submitted to the Med. Phys. journal in a dedicate study called "A reference Monte Carlo beam model of the MedAustron proton horizontal fixed beam line using GATE/Geant4" [132].

The beam model developed in the framework of this PhD represents the core of the MC dose calculation tool that will be used at MedAustron as IDC for the proton horizontal beam line. After the beam model validation in 3D, the patient specific quality assurance setup was successfully reproduced for all the selected clinical cases within ±0.6% and up to -1.5% in case of range shifter. The presented results, fully validate the clinical workflow necessary for plan treatment recalculation with GATE.

At the current status of the project, a deep commissioning program of GATE considering more complex cases such as heterogeneous phantoms and the impact of oblique incidence of the beam irradiation represent a future prospective. Based on the presented work, it is underway to increase the clinical complexity to further support the use of GATE for direct treatment plan verification. Further, new possibilities for plan evaluation will be opened such as an accurate evaluation of the treatment delivery uncertainties [68]. In future, new versions of GATE will be available and different improvements of the current functionalities as well as new implementations clinically oriented are planned[1]. For instance, GATE will be capable to fully simulate a gantry irradiation at any beam incident angle, to consider the prompt-gamma analysis for in-vivo range verification and to provide studies in terms of intra- and inter-fractional movements during treatment, particularly suitable to GATE thanks to its capability of scoring over time.

In order to provide dose calculation in patient tissue, a deep validation of the CT calibration curves is necessary. Three different protocols of the CT calibration are currently implemented in GATE, depending on the clinical case (head, pelvis or pediatric patients). The calibration is validated during the commissioning phase of the TPS by measurements of the WET for different tissues. The same experimental conditions can be reproduced by GATE in order to validate the implementation of the CT calibration in the simulation. The MC dose calculation in the patient will be inserted within the clinical workflow of MedAustron in order to provide support to the medical physicist during clinical activities.

Last but not least, as dual facility, MedAustron is currently approaching its commissioning phase for carbon beams, which means that the beam model presented with this PhD would serve as reference for the upcoming modeling and validation

---

[1] http://www.opengatecollaboration.org/GateRTion

work of GATE for carbon treatments. In this case, new challenges will be faced. For instance, contrary to protons where the MCS scattering has a crucial impact, the physics list selection has to carefully evaluated for the simulations as it will affect the energy spectra at different depths and therefore, the typical fragmentation tail beyond the Bragg peak as well as the halo. For carbon simulations, an optimization of the simulation setting for carbon must also be performed to do not incur into computational deficiencies. Eventually, a deep verification post-irradiation is also possible with carbon treatments thanks to tissue activation and PET imaging analysis, perfectly compatible with GATE functionalities.

CHAPTER 7

Résumé en français

7.1 Introduction

En 2015, environ 90.5 millions de personnes souffraient d'un cancer ,et chaque année on dénombrait environ 14.1 millions de nouveaux cas de cancer[1] [1, 2]. Le cancer cause environ 8.8 millions de décès, ce qui correspond à 15.7% des décès [3]. Chez les enfants, la leucémie lymphoblastique aiguë et les tumeurs cérébrales sont les cancers les plus courants. Une exception est représentée par l'Afrique où le lymphome non hodgkinien survient plus souvent que les tumeurs cérébrales et en 2012, environ 165,000 enfants de moins de 15 ans ont reçu un diagnostic de cancer [2]. En Autriche, environ 39,000 personnes développent un cancer chaque année [4]. Même si les hommes sont légèrement plus touchés que les femmes, pour les deux sexes, les maladies tumorales malignes sont la deuxième cause de décès la plus fréquente, précédée par les maladies cardiovasculaires [4]. Selon les estimations actuelles, deux personnes sur cinq auront un jour ou l'autre un cancer au cours de leur vie [5]. Trois principales techniques de traitement du cancer sont couramment utilisées : la chirurgie, la chimiothérapie (traitement systémique) et la radiothérapie. Le choix de ces trois thérapies dépend de nombreux facteurs, par exemple la localisation de la tumeur, le stade de la maladie et l'anamnèse du patient. Dans la mesure du possible, une résection complète de la tumeur aboutit à un traitement curatif dans la plupart des cas, sans dommage importants pour les tissus sains. Cependant, la capacité des cellules malignes à se métastaser sur des sites adjacents conduit à des micro-métastases difficiles à détecter. Par conséquent, des traitements coadjuvants et adjuvants sont alors nécessaires pour augmenter la probabilité de contrôle de la

---

[1] les cancers de la peau autres que le mélanome ne sont pas pris en compte.

tumeur. D'autre part, le traitement systémique et la radiothérapie peuvent aussi parfois avoir un effet négatif en raison d'effets secondaires non négligeables [6]. De nouvelles techniques et méthodes contre le cancer sont constamment étudiées par la recherche moderne afin d'augmenter la probabilité de contrôle de la tumeur et de réduire les effets secondaires inévitables. A cet égard, la thérapie par rayonnement a joué un rôle important en tant qu'alternative valable depuis plus de 60 ans. Au cours de cette période, des améliorations techniques remarquables ainsi que des résultats cliniques ont été obtenus dans le domaine de la radiothérapie conventionnelle par faisceau de photon et la thérapie par faisceau d'ions lourds. Dans ce qui suit, quelques considérations générales sont présentées en guise d'introduction à ce manuscrit. Sauf indication contraire, les concepts donnés ne s'appliquent qu'à la proton thérapie.

7.1.1 Simulation de Monte Carlo en la proton thérapie

Avoir une technique supérieure et avancée pour le traitement du cancer, comme le proton thérapie, ne garantit pas un traitement réussi en soi. Les incertitudes inévitables liées au processus de planification du traitement et à l'administration de la dose sont hautement responsables de l'exactitude et de la précision que l'on peut atteindre. Un changement significatif de la probabilité de contrôle de la tumeur peut être induit par une variation de 7 à 10% de la dose au volume cible [46]. Par conséquent, il est essentiel d'évaluer que l'ensemble du système thérapeutique est capable d'administrer une dose à la région d'intérêt dans les 5 % de la dose prescrite [46].

La chaîne des processus qui mènent à un traitement réussi est généralement longue et complexe. Le déroulement du travail clinique comporte de nombreuses étapes comme l'immobilisation et la mise en place du patient, la délimitation du contour des organes à risque et des organes d'intérêt, l'imagerie diagnostique du patient et le mouvement intra-fractionnel des organes, pour ne citer que quelques exemples. Chacune des étapes représente une source potentielle d'erreur et parfois, la situation peut être encore plus complexe puisqu'une seule étape peut être composée de plusieurs sous-étapes.

En tant que partie intégrante du flux de travail clinique, un moteur de calcul de dose doit également répondre aux exigences de précision. En proton thérapie, et en particulier en proton thérapie par balayage, il existe essentiellement trois classes d'algorithmes de calcul de dose [8, 48]: *ray casting*, *pencil beam* et méthodes de Monte Carlo (MC). En général, chacun des algorithmes utilisés pour le calcul des doses traite d'approximations différentes à des niveaux différents. Une fois l'approximation introduite, elle entraîne inévitablement des incertitudes dont il faut tenir compte. Un point crucial dans les incertitudes d'un algorithme de calcul de dose est la façon dont il traite l'hétérogénéité des tissus du patient. Par exemple, l'algorithme de lancé de rayons considère comme élément le plus petit pour le calcul de la dose le pencil beam physique et, pour tenir compte de l'hétérogénéité dans la direction du champ, il met à l'échelle la Water Equivalent Depth (WED) de chaque point de calcul de la grille de dose [8, 48]. L'algorithme moderne du *pencil beam* introduit une amélioration de cette approche grâce à la technique du *sub-spot [49]*. Cependant, les incertitudes dosimétriques chez les patients peuvent encore être possibles en raison, par exemple, des implants marqueurs et des milieux très hétérogènes [50]. De nos jours, l'algorithme du pencil beam permet la représentation la plus pragmatique du transport de particules dans le milieu [8] et il est cliniquement utilisé dans la plupart des systèmes de planification du traitement (TPS) utilisés pour le calcul des doses. Néanmoins, des scénarios spécifiques pourraient conduire à une précision plus faible de la distribution de dose prévue et, par conséquent, une approche plus précise est nécessaire. Pour l'instant, seuls les algorithmes MC sont capables de fournir une alternative valable à ce problème grâce à son approche non-analytique. Malgré un temps de calcul plus long, un calcul MC peut mieux tenir compte des problèmes d'hétérogénéité des tissus du patient.

Les méthodes MC appliquées à la proton thérapie améliorent non seulement la précision du calcul de la dose, mais fournissent également des informations utiles qui ne peuvent être obtenues autrement. Une évaluation approfondie des incertitudes liées aux traitements cliniques [51, 52] est une étape cruciale vers une meilleure qualité de traitement. Par exemple, une analyse détaillée des incertitudes de l'intervalle pourrait entraîner une réduction de la marge de sécurité appliquée au cours du processus de planification et, par conséquent, une diminution des complications tissulaires normales [53]. Cependant, même les méthodes MC sont affectées par des incertitudes inévitables qui doivent être prises en compte.

Selon [53], les incertitudes typiques pour les calculs des MC peuvent être indépendantes du calcul de la dose, comme la configuration du patient ou la reproductibilité du faisceau, ou dépendent du calcul de la dose. En ce qui concerne les incertitudes dépendantes du calcul de la dose, deux contributions sont surtout abordées [53]: les définitions de la géométrie du patient basées sur la TDM et l'algorithme de dose lui-même. La première implique la calibration du scanner ainsi que la conversion de l'unité de Hounsfield (HU) en puissance d'arrêt relative ou en composition de matériau, tandis que la seconde implique principalement les incertitudes de sections efficaces ainsi que la mise en œuvre de modèles physiques [53].

7.1.2 A propos de ce projet

En décembre 2014, une collaboration internationale entre le laboratoire CREATIS du centre Léon Bérard à Lyon (France) et le centre d'hadronthérapie MedAustron à Wiener Neustadt (Autriche) est lancée. La collaboration vise à la mise en œuvre de la boîte à outils GATE au niveau clinique, conformément à la pratique clinique et aux spécifications de MedAustron. La possibilité d'établir un workflow clinique basé sur le recalcule par GATE est suggérée pour la première fois en 2011, lors d'un précédent projet de doctorat, où un cas clinique de traitement protonique a été reproduit dans GATE pour une installation basée sur un cyclotron [73]. Dans cette thèse, les concepts de base de proton thérapie (chapitre 2) sont abordés dans un premier temps. Dans le troisième chapitre, une description de l'installation d'ions légers MedAustron est fournie, avec un accent particulier sur le système d'émission du faisceau et le TPS. Une partie considérable du projet a été consacrée à la modélisation du faisceau du pencil beam à protons, dont il est question dans le quatrième chapitre. Dans le chapitre 5, les procédures utilisées à MedAustron pour la vérification du traitement des patients sont décrites afin de montrer une application clinique directe des simulations GATE à MedAustron. De plus, les plans de vérification du traitement des patients recalculés par GATE représentent une première application du système GATE en tant que *independent dose calculation* system (IDC) à MedAustron.

7.2 Concepts de base pour la proton thérapie

Dans ce chapitre, une introduction aux concepts physiques et biologiques de base de la proton thérapie est donnée, principalement en comparaison avec la radiothérapie conventionnelle. Les sections sont orientées respectivement vers la physique, la radiobiologie et la dosimétrie afin de donner au lecteur les éléments nécessaires à la compréhension de base du travail présenté.

7.2.1 Physique du *pencil beam* à protons

D'un point de vue de la physique classique, la description de l'interaction entre les particules implique deux paramètres fondamentaux : le paramètre d'impact b et le rayon atomique a (voir la figure 7.1). Pour simplifier, la relation réciproque entre a et b établit différent type d'interactions [80]:

- *soft collision* pour $b >> a$;
- *hard collision (*ou *knock-on)* pour $b \simeq a$;
- *nuclear interaction* pour $b << a$.

En cas de *soft collision*, tout le nuage électronique de l'atome cible interagit avec le champ de Coulomb de la particule incidente, provoquant une excitation ou, plus rarement, une ionisation de l'atome cible [80]. En cas de collision violente, un proton interagit avec les coquilles internes de l'atome cible (voir figure 7.1-(B)). Ce processus peut être suivi de nombreux processus différents tels que l'émission d'électrons énergétiques (δ-ray) ainsi que l'émission de rayons X caractéristiques et d'un électron Auger [80]. Une *hard collision* avec le noyau de l'atome cible est également possible (voir figure 7.1-(C)). Finalement, la condition $b << a$ indique surtout une nuclear interaction, c'est-à-dire une interaction avec le noyau de l'atome (voir figure 7.1-(D)). Chaque type de collision peut être classé comme collision *elastic* ou *non-elastic*, que l'énergie cinétique impliquée pendant le processus soit conservée ou non. En ce qui concerne les interactions nucléaires *non-elastic*, il est possible de faire la distinction de collisions dites inelastic, pour lesquelles le noyau final est

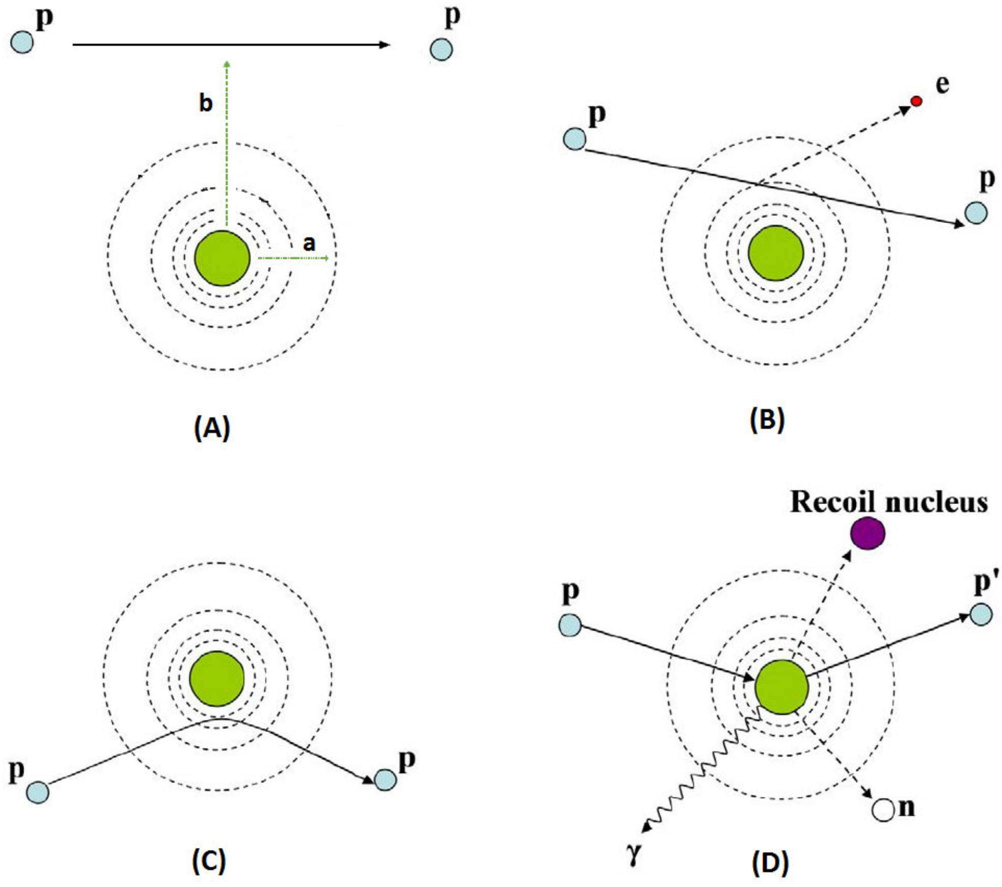

Figure 7.1: illustration des processus d'interaction des protons selon l'interprétation classique : (A) représentation d'une collision douce entre un proton incident et un atome cible où le paramètre d'impact b et le rayon atomique classique a ont été mis en évidence, (B) perte d'énergie par des interactions de Coulomb inélastiques pour une collision dure, (C) déviation de la trajectoire du proton par diffusion élastique de Coulomb répulsive avec noyau (collision dure), (D) élimination du proton primaire et création des particules secondaires par interaction nucléaire non élastique (p : proton, e : électron, n : neutron, γ: rayons gamma). Adapté de [50].

le même que le noyau bombardé [81]. Toutes les particularités et les avantages importants d'un traitement protonique par rapport à un traitement photonique, reposent sur les mécanismes physiques par lesquels un proton interagit avec un atome.

Le taux de perte d'énergie des particules chargées est défini comme le rapport entre dE et dx, où E est la perte d'énergie moyenne et x est la profondeur. La première théorie physiquemLe taux de perte d'énergie des particules chargées est défini comme le rapport entre dE et dx, où E est la perte d'énergie moyenne et x est la profondeur. La première théorie physiquement complète à décrire le linear stopping power (ou puissance d'arrêt linéaire) est attribuée à Bohr en 1915 [82]. Une formule précise décrivant la *stopping power* électronique et tenant compte des effets de mécanique quantique est attribuée à Bethe [84] et Bloch [85]:

$$\left(-\frac{dE}{dx}\right)_{el} = 2\pi r_e^2 m_e c^2 N_A \rho \frac{Z}{A}\frac{z^2}{\beta^2}\left[\ln\left(\frac{2m_e\gamma^2 v^2 W_{max}}{I^2}\right) - 2\beta^2 - 2\frac{C}{Z} - \delta\right] \tag{7.1}$$

où N_A est le nombre d'Avogadro, r_e est le rayon d'électron classique, m_e est la masse d'un électron, z est la charge du projectile, Z est le numéro atomique du matériau absorbant, A est le poids atomique du matériau absorbant et I est le potentiel moyen d'excitation du matériau absorbant. Dans l'équation 7.1 le matériau de l'absorbeur peut aussi fortement influencer le taux de perte d'énergie par la contribution de la densité massique. La forte dépendance de la densité du matériau ρ justifie l'utilisation plus pratique de la *mass stopping power*.

Dans la formule 7.1 sont également exprimés deux termes de correction importants: δ qui représente la correction de densité résultant du blindage des électrons éloignés par des électrons proches, ce qui entraîne généralement une réduction des pertes d'énergie aux énergies supérieures, et le terme $2C/Z$ qui représente la correction d'enveloppe, important uniquement pour les faibles énergies où la vitesse des particules est proche de celle des électrons atomiques [50]. Le terme W_{max} exprime l'énergie maximale transférée lors d'un seul choc ou d'un choc.

Les protons primaires traversent le milieu jusqu'à ce qu'ils se neutralisent complètement à la fin de leur trajet. La plage finale dépend uniquement de l'énergie initiale et du taux moyen de perte d'énergie dans le fluide. Il est donc possible d'exprimer le trajet moyen d'une particule chargée dans la matière par en intégrant l'équation 7.1. Les fluctuations statistiques de la perte d'énergie pour chaque particule incidente impliquent une dispersion dans la gamme des particules. Ce phénomène est à l'origine de ce que l'on appelle *range straggling*, qui provoque l'élargissement du pic de Bragg en fonction de la profondeur (voir figure 7.1).

D'un point de vue classique, un proton passant près du noyau atomique peut dévier sa trajectoire originale en raison des interactions élastiques de Coulomb. Selon la théorie de Molière [90], la *multiple Coulomb scattering* (MCS) peut être caractérisée comme une conséquence de plusieurs événements de diffusion avec une déviation de la direction de l'incident due à de petits angles hautement probables.

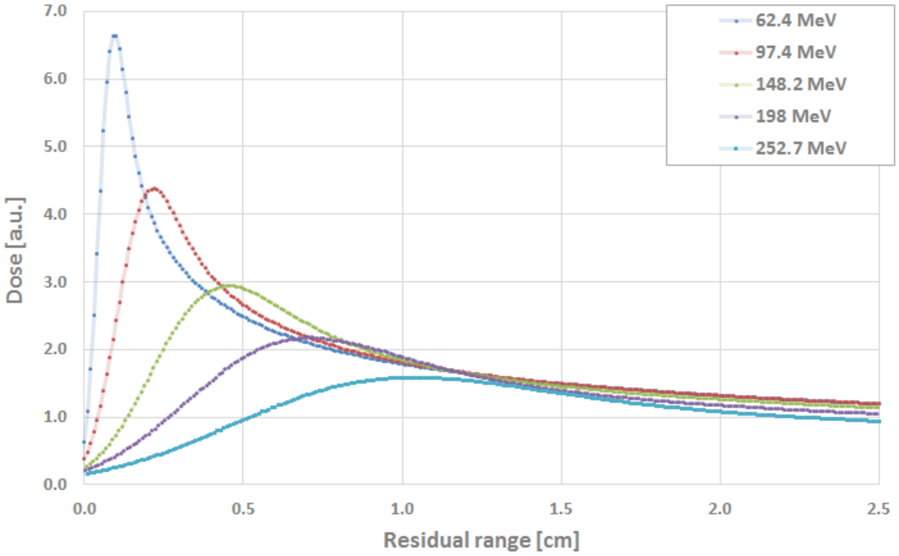

Figure 7.2: exemple de la *range straggling* pour les protons. Les dépôts d'énergie pour cinq énergies cliniques représentatives sont calculés dans l'eau par GATE/Geant4 [56, 57, 63, 64] et tracés en fonction de la plage résiduelle. On peut remarquer que l'élargissement de la largeur du pic de Bragg augmente en raison des phénomènes de *range straggling*.

Si l'on néglige la probabilité d'avoir des écarts élevés, on sait que la distribution due à la diffusion de petits angles (moins de 10°) est de forme presque gaussienne [91] avec une seule queue de diffusion (*core region* [92]). De grands événements de diffusion unique, bien que rares, provoquent la distorsion d'une distribution gaussienne à queue unique, caractérisant l'enveloppe externe du noyau, appelée *halo* [92] (voir figure 7.3). En ce qui concerne *lateral spread*, trois aspects remarquables sont importants:

- l'angle de diffusion augmente considérablement avec la profondeur;
- les faisceaux à faible énergie diffusent plus que les faisceaux à haute énergie;
- les ions plus lourds dispersent moins d'ions que les ions plus légers.

Dans la figure 7.4 sont illustrés les comportements cités.

7.3 Le centre d'hadronthérapie MedAustron

Le centre d'hadrontherapie MedAustron, construit à Wiener Neustadt (Autriche), a commencé ses opérations cliniques en décembre 2016. L'objectif de l'installation n'est pas seulement de traiter le cancer, mais aussi d'effectuer de la recherche de

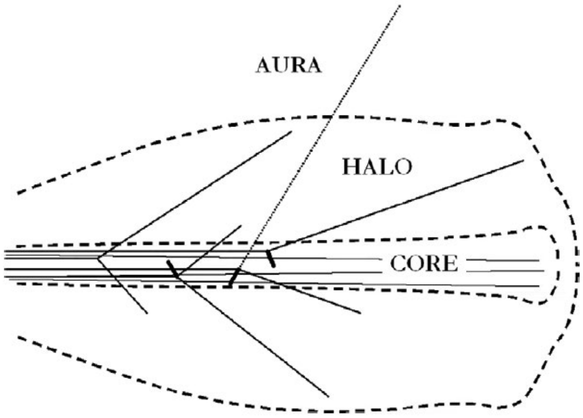

Figure 7.3: représentation des régions de dose pour un pencil beam à protons proposée dans [92].

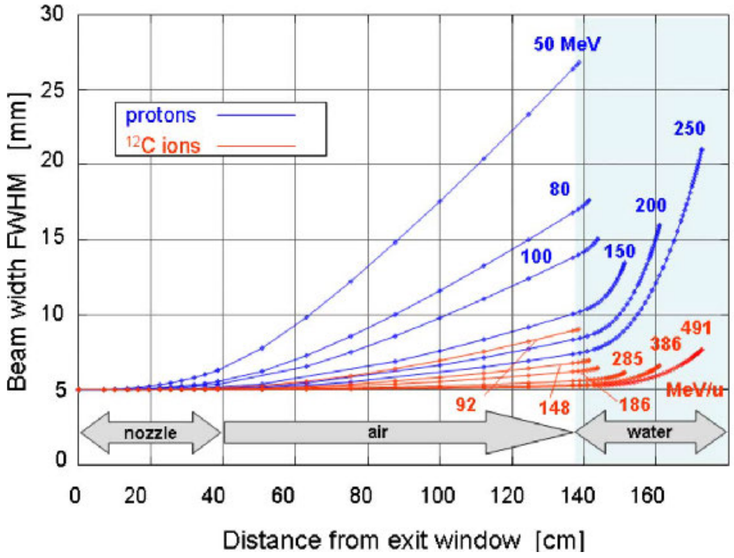

Figure 7.4: simulation d'un faisceau de protons et d'ions carbone à différentes énergies et à travers différents matériaux. La simulation est initialisée pour un FWHM fixe au niveau de la source et montre les différents comportements d'étalement latéral du faisceau en fonction de la profondeur [95].

pointe sur les thérapies par faisceaux d'ions légers. Le centre est conçu pour deux types de particules, ce qui signifie que l'irradiation par protons et par ions carbone est disponible cliniquement. En juillet 2018, environ 25 patients par jour ont été traités avec des protons pendant que des activités de mise en service (*commissioning*) du faisceau de carbone été menées en parallèle. Un total d'environ 1200 patients traités par an devrait être atteint lorsque le centre sera en pleine capacité clinique. [115].

Le projet MedAustron s'appuie sur l'expérience européenne d'autres installations d'hadronthérapie à deux types de particules. Au moment de la rédaction de ce manuscrit, seules quatre installations doubles sont actuellement en service en Europe: Heidelberg Ionenstrahl Therapiezentrum (HIT) (Allemagne), Marburg Ionenenstrahl Therapiezentrum (MIT) (Allemagne), Centro Nazionale di Adroterapia Oncologica (CNAO) à Pavie (Italie) et MedAustron. Ce chapitre donne un aperçu technique du dispositif présent à MedAustron.

Le MedAustron Particle Therapy System (MAPTS) est le système médical intégré dans l'ensemble de l'établissement. Il est composé de plusieurs sous-systèmes qui agissent indépendamment et de manière synchronisée. Une description détaillée du MAPTS n'entre pas dans le cadre du présent rapport, mais il convient de mentionner d'importants éléments tels que l'accélérateur de particules MedAustron (MAPTA), le système de contrôle de la dose (DDS) et le système d'alignement des patients (PAS). Dans ce rapport, l'accent est mis sur la partie distribution du faisceau. Le MAPTS délivre le faisceau au total dans quatre salles d'irradiation (IR). Trois salles (IR2, IR3, IR4) sont dédiées aux traitements des patients et une salle (IR1), à la recherche non clinique (NCR) et dispose d'un faisceau protons jusqu'à 800 MeV. Les protons et les ions carbones sont disponibles dans toutes les salles à l'exception de l'IR4 car elle est équipée d'un *gantry* pour faisceau protons uniquement. La salle IR3 est alimentée par une ligne de faisceau horizontale uniquement, tandis que l'IR2 dispose en plus d'une ligne de faisceau verticale.

Il convient de noter que le PAS a été développé dans le cadre d'une coopération entre MedAustron, Buck Engineering and Consulting GmbH à Reutlingen (Allemagne) et MedPhoton GmbH à Salzbourg (Autriche), et est installé dans chacune des IR. Le PAS se compose d'un robot monté au plafond équipé d'un système annulaire d'imagerie monté sur table composé d'une source de rayons X (60-120 kV) et d'un détecteur plan (voir figure7.5). Une grande variété de mouvements de la table est possible, jusqu'à 7 degrés de liberté. Une translation supplémentaire est disponible grâce à l'axe linéaire qui permet de déplacer le patient vers la tête de traitement, avec un débattement de robot réduit. Le système d'imagerie monté sur la table permet de corriger directement et avec finesse l'alignement du patient [116]. La technique de traitement non isocentrique est couramment utilisée à MedAustron et elle doit être exécutée avec soin car la précision du PPS peut être réduite en s'éloignant de l'isocentre. De plus, comme l'éloignement du patient de l'isocentre n'est pas une pratique clinique courante, il nécessite un commissioning supplémentaire. D'autre part, les traitements non isocentriques améliorent la

Figure 7.5: simulation d'un faisceau de protons et d'ions carbone à différentes énergies et à travers différents matériaux. La simulation est initialisée pour une FWHM fixe au niveau de la source et montre les différentes distributions latérales du faisceau en fonction de la profondeur [95].

précision dosimétrique si l'on utilise le *range shifter*.

7.3.1 Beam delivery système

Le système de délivrance du faisceau ou *Beam Devery System* (BDS) se compose de deux parties: un système basé sur le synchrotron inspiré de la conception du PIMMS [117] et la tête de traitement. Les traitements sont effectués à l'aide de la technique de balayage ponctuel quasi-discret, mise en œuvre pour l'émission dynamique du faisceau [75]. La tumeur est subdivisée en tranches (*slice*), c'est-à-dire en régions de volume tumoral irradiées par des particules de mêmes énergies (*energy layer*). Chaque tranche est ensuite balayée dans le plan transversal par rapport à la direction du faisceau. Chaque tranche est ensuite balayée au-dessus du plan transversal par rapport à la direction du faisceau.

Dans les salles de traitement cliniques, au totale 255 énergies sont disponibles entre 62.4 et 252.7 MeV (parcours dans l'eau compris entre 3 et 38 cm avec des pas de 1 mm jusqu'à 18.8 cm et de 2 mm au delà) [119]. Sur les 255 énergies disponibles, des sous-ensembles d'énergies espacées régulières ont été définis: 20 énergies 'majeures'

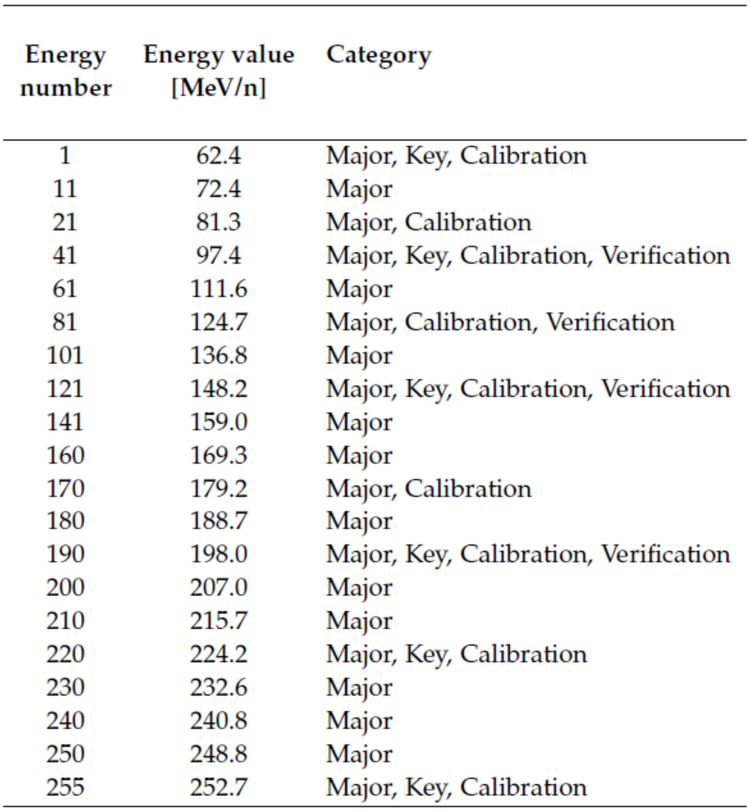

Energy number	Energy value [MeV/n]	Category
1	62.4	Major, Key, Calibration
11	72.4	Major
21	81.3	Major, Calibration
41	97.4	Major, Key, Calibration, Verification
61	111.6	Major
81	124.7	Major, Calibration, Verification
101	136.8	Major
121	148.2	Major, Key, Calibration, Verification
141	159.0	Major
160	169.3	Major
170	179.2	Major, Calibration
180	188.7	Major
190	198.0	Major, Key, Calibration, Verification
200	207.0	Major
210	215.7	Major
220	224.2	Major, Key, Calibration
230	232.6	Major
240	240.8	Major
250	248.8	Major
255	252.7	Major, Key, Calibration

Table 7.1: résumé des sous-catégories pour les énergies livrables par le BDS.

utilisées pour l'acceptante de l'accélérateur, l'acquisition des données de base et de modélisation du faisceau pour le TPS, 5 énergies 'clés' représentatives des 255 pour toute mesure rapide de données de base, 9 énergies 'd'étalonnage' utilisées pour la calibration du DDS et du TPS, et 4 énergies de vérification pour vérifier le modèle du faisceau avec un absorber . La liste des energies est résumée dans le tableau suivant 7.1.

Afin d'assurer la sécurité des patients et d'effectuer un diagnostic en ligne du faisceau de traitement, chacune des quatre lignes de faisceaux est équipée de deux systèmes de surveillance de la dose : le système de contrôle de la dose (DDS) et système de terminaison indépendant (ITS). Le DDS utilisé à MedAustron est basé sur la conception de celui de CNAO [120] et il contient plusieurs moniteurs de faisceau qui surveillent et contrôlent dynamiquement différents paramètres du faisceau tels que la position, la taille et le nombre de particules du spot de faisceau. Un schéma de l'ensemble de la conception de la tête de traitement est illustré sur la figure 7.6. Bien que l'ITS et le DDS soient deux systèmes complètement indépendants, le DDS est également divisé en deux parties indépendantes (Box), BOX1 et BOX2.

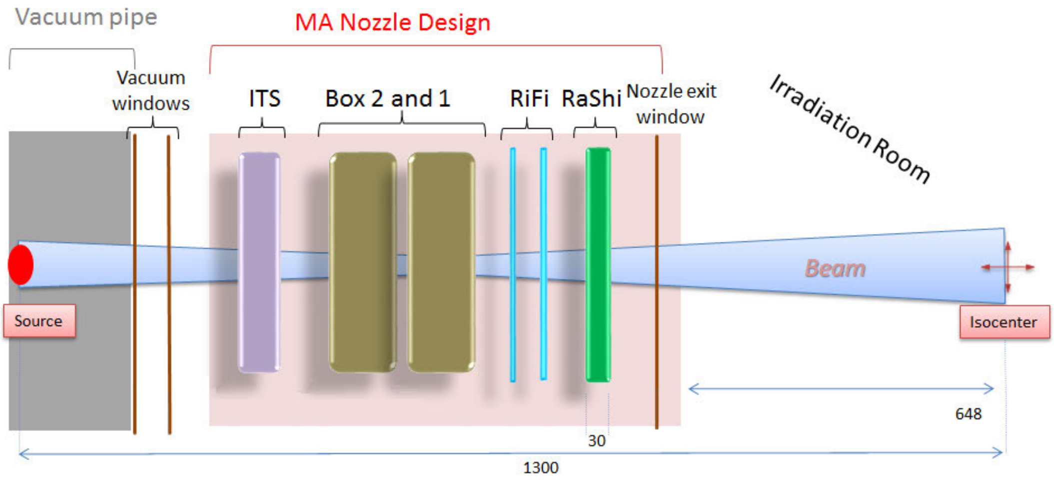

Figure 7.6: représentation schématique de la tête de traitement MedAustron (*nozzle*). Il contient une fenêtre à vide à double feuille, le système de terminaison indépendant (ITS), les deux boxes du système de contrôle de la dose (DDS) et la fenêtre de protection de la fin de la tête de traitement. Les éléments passifs, deux filtres d'ondulation (*ripple filters*) et un absorbeur (*range shifter*) sont également représentés.

En cas d'erreur mesurées par une des Box, par exemple des écarts importants de décompte de particules ou des erreurs de position du faisceau supérieures à 2.3 mm, le DDS déclenche le système de sécurité qui stoppe le traitement.

Des aimants spécifiques, appelés aimants de balayage, déplacent en continu le faisceau d'un point à l'autre sur chaque tranche (balayage quasi-discret) avec une vitesse qui dépend de l'énergie du faisceau (370 m/s au maximum pour les protons de 62.4 MeV) et avec une précision de 0.2mm généralement meilleure que 1 mm. Dès que la totalité de la tranche est irradiée, l'énergie du faisceau diminue afin de passer à la tranche proximale suivante. Contrairement à la technique passive où des compensateurs sont intercalés dans la tête de traiment pour diminuer l'énergie, la technique active évite d'exposer le patient à des doses indésirables dues au spectre secondaire produit dans les compensateurs.

Les éléments passifs tels que les filtres d'ondulation (*ripple filters*) et l'absorbeur (*range shifter*) sont directement intégrés dans la conception de la tête de traitement. Le *range shifter* est utilisé à la fois pour les ions carbones et pour les protons dans les cas où la cible est située à de très faibles profondeurs, non atteignable avec l'énergie minimale.

7.3.2 Systèmes de calcul de dose

Un système de planification du traitement (TPS) est couramment utilisé dans la pratique clinique pour calculer les différentes configurations de doses en fonction de contraintes spécifiques. Le TPS utilisé chez MedAustron est RayStation (RS) (RaySearch Laboratories, Stockholm, Suède), capable d'établir un plan de traitement protons et ions carbone par balayage actif (*pencil beam scanned* ou PBS). RS prend en charge différents models de calcul de la dose, mais deux en particulier présentent un intérêt pour la portée du présent rapport: l'algorithme pencil beam et le model de dose basé sur Monte-Carlo (MC). Le premier est largement utilisé dans le cadre du calcul de la dose par protons [49, 48, 94, 123, 124, 125, 126, 127, 128] tandis que le second est mis en œuvre par le laboratoire RaySearch pour offrir une approche plus précise à l'utilisateur, malgré un temps de calcul plus élevé [128].

Dans la méthode du *pencil beam*, la fluence de protons est subdivisée en un grand nombre de mini-faisceaux rapprochés, appelé *pencil beam* [128]. Les paramètres de l'espace de phase sont transportés le long de l'axe central de chacun des faisceaux de crayons, ce qui explique la perte d'énergie, le MCS et la diffusion nucléaire non élastique [128]. Le model de dose MC implémenté dans RS n'est supporté par aucune boîte à outils MC commune et simule le transport des particules à travers le milieu par la méthode dite *random hinge* [128]. Le transport prend en compte la perte d'énergie, les phénomènes de retard énergétique ou *straggling*, le MCS et l'interaction nucléaire non élastique d'une manière plus précise que l'algorithme *pencil beam*, d'où un temps de calcul plus élevé.

7.4 Caractérisation de la ligne fixe du faisceau de protons MedAustron

Pour l'émission du faisceau de protons, l'espace entre la fenêtre de sortie de la nozzle et le patient peut agrandir la pénombre latérale et réduire la précision de l'algorithme du faisceau de protons, surtout si l'on considère le *range shifter* (RaShi) [49, 130]. Une solution possible pour réduire l'espace dans la pratique clinique est de déplacer le patient vers la sortie de la nozzle. Les outils de simulation de Monte Carlo (MC) sont souvent utilisés pour le calcul indépendant des doses, car ils peuvent fournir des informations utiles qui ne peuvent être obtenues autrement [72, 133, 134, 135]. Cependant, tout moteur de calcul de dose indépendant doit être soigneusement caractérisé et validé avant sa mise en œuvre dans des applications cliniques. La caractérisation typique d'un faisceau de protons peut être effectuée sur la base de courbes de dose de profondeur mesurées, de cartes de spots mesurées à différents intervalles d'air et de mesures de dose en condition de référence [69, 124, 136]. Dans la littérature, différentes méthodes de modélisation du *pencil beam* à protons ont été proposées en fonction des types de code MC et des caractéristiques de la ligne de faisceau [72, 69, 136, 137, 138, 139]. Pour les systèmes à balayage actif, les simulations précises d'un *pencil beam* à protons nécessitent une connaissance approfondie des propriétés optiques du *pencil beam* car la corrélation entre la position des protons et la dispersion angulaire (émission du faisceau) ne peut être négligée a priori [72]. L'omission de la simulation de la géométrie de la nozzle permet une modélisation empirique du *pencil beam* avec une réduction supplémentaire en temps de calcul [136, 137, 139]. Néanmoins, cette approche nécessite des corrections supplémentaires [49, 140] pour tenir compte des particules primaires et secondaires diffusées simples à grand angle produites dans les composants des nozzles [74, 94, 136].

7.4.1 Mesures expérimentales

Le modèle de faisceau MC proposé est basé sur des fonctions analytiques avec des valeurs de paramètres dérivées de données de mesures expérimentales. Les données expérimentales utilisées pour la modélisation des faisceaux ont été acquises au cours des activités de mise en service de la physique médicale. Une partie de ces données consiste en des profils transversesacquis en termes de FWHM à sept intervalles d'air en utilisant le cristal scintillant Lynx (IBA-dosimétrie). Les positions de mesure seront désignées comme suit: ISD+20cm, ISD0, ISD-20cm, ISD-30cm, ISD-40cm, ISD-50cm et ISD-58cm où la surface ISocenter to Detector (ISD) avec valeur négative est vers la nozzle (entrefer réduit entre la nozzle et le patient). D'autres cartes ponctuelles ont été acquises à ISD0, ISD-30cm, ISD-40cm, ISD-50cm et ISD-58cm lorsque le RaShi était en place pour 4 énergies de vérification (97.4, 124.7, 148.2, 198 MeV). D'autres données consistent en des profils de dose en profondeur acquis dans l'eau à l'isocentre à l'aide du fantôme d'eau MP3-PL (PTW, Freiburg) avec la chambre de pic de Bragg TM 34070 (diamètre des électrodes de 81,6 ± 0,2 mm). De plus, le MP3-PL a été aligné à ISD-50cm lorsque les mesures utilisant le RaShi ont été acquises pour les 4 énergies de vérification. En ce qui concerne la calibration des chambres moniteurs de faisceau en condition de référence, la dose absorbée dans l'eau a été mesurée en une seule couche uniforme de 12x12 cm 2 pour 9 énergies d'étalonnage (62.4, 81.3, 97.4, 124.7, 148.2, 179.2, 198, 224.2 et 252.7 MeV) en utilisant le protocole IAEA TRS-398. Des mesures tridimensionnelles de distribution de dose de forme cubique ont été effectuées dans l'eau en utilisant 24 chambres d'ionisation TM 31015 (type PinPoint avec volume de mesure 0.03 cm^3 et rayon 1.49 mm, PTW, Freiburg) caractérisées en faisceau de protons. Les 24 PinPoints ont été montées dans un support (bloc 3D) fixé au mécanisme mobile du fantôme d'eau MP3-PL, permettant une vérification quasi tridimensionnelle de la distribution des doses délivrées. Les boîtes Box6(0,0,6), box8(0,0,15) et box10(0,0,25) ont été délivrées à l'isocentre où la boîte de notationN(0,0,Z) représente une distribution de dose cubique avec une longueur latérale de N cm et son centre placé à la profondeur équivalente en eau Z. Une quatrième box, la box6(0,0,5) a été délivrée pour des conditions non isocentriques (ISD-50cm) utilisant un RaShi.

7.4.2 Méthode de modélisation et validation

GATE v7.2 avec Geant4 v10.02 ont été utilisés. L'énergie d'excitation moyenne de l'eau Iw a été réglée à 78 eV. Pour la modélisation de l'optique du faisceau et le des simulations de dose en profondeur. Le constructeur physique QBBC_EMZ a été sélectionné. Les paramètres optiques du faisceau ont été adaptés de façon itérative pour minimiser (jusqu'à 0.2 mm dans la mesure du possible) les différences entre la FWHM mesurée et la FWHM simulée. La tolérance de 1 mm en écart absolu et de 10% en termes relatifs a été prise en compte pour les cinq énergies clés (62.4, 97.4, 148.2, 198, 252.7 MeV), selon la pratique clinique à MedAustron. Finalement, les paramètres du faisceau (taille du spot, divergence du faisceau et émittence du faisceau) ont été décrits sur toute la gamme d'énergie clinique par un ajustement polynomial du nième ordre aux cinq énergies clés, avec n de 1 à 8 en fonction du paramètre spécifique. Au total, 280 évaluations des différences résiduelles ont été effectuées à cette étape de l'étude en termes absolus et relatifs. La même évaluation des différences résiduelles a été effectuée sur 4 énergies de vérification (97.4, 124.7, 148.2 et 198 MeV) avec RaShi à 5 entrefer. Les propriétés énergétiques ont été estimées par une procédure itérative pour faire correspondre les simulations MC avec les mesures en termes de parcours physique (R80) et de largeur de pic de Bragg à 80%. (BPW80). D'autres paramètres ont été évalués : parcours clinique (R90) et parcours pratique (Rp) définie comme étant le niveau de dose de 90% et de 10%, respectivement, dans la partie distale d'un profil de dose en profondeur. Pour étalonner un modèle de faisceau MC en dose absolue est d'établir la relation entre le nombre de particules N et le produit dose surface (Dose Area Product DAP) délivrées dans des conditions de référence:

$$N = \frac{DAP_W^A(z_{ref})}{d_W(S_{el}^{\rho}, \Phi_z^A) \cdot A} \tag{7.2}$$

Le numérateur de l'équation 7.2 est le DAP déterminé expérimentalement dans l'eau à la profondeur de référence z_{ref} sur la surface A. En général, le terme $d_W(S_{el}^{\rho}, \Phi_z^A)$ représente la "*mean stopping power*" par proton incident évalué par un moteur dose quelconque et il est caractérisé comme suit:

$$d_W(S_{el}^{\rho}, \Phi_z^A) \cdot A = \frac{\sum_i \int (S_{el,i}/\rho)_W \Phi_{E,i}^A(z_{ref}) dE}{n} \tag{7.3}$$

$(S_{el,i}/\rho)_W$ dans cette expression est le pouvoir d'arrêt électronique de masse de l'eau pour les espèces ioniques i et $\Phi_{E,i}^A(z_{ref})$ est le différentiel de fluence en énergie de cette espèce ionique à la profondeur de référence z_{ref}. Le point clé de cette approche est de calculer par une simulation MC dédiée le terme $d_W(S_{rel}, \Phi_z^A)$ pour un nombre connu de protons n, comme décrit par l'équation 7.2. Par conséquent, un seul pencil beam a été simulé et marqué dans un volume cylindrique de 7 cm de rayon, suffisamment grand pour englober toutes les particules chargées du champ de rayonnement sur toute la gamme d'énergie clinique.

Une validation finale a été réalisée en termes de distribution de dose 3D dans l'eau pour les quatre cubes de dose 3D de dimensions différentes. Les écarts de dose locaux par rapport aux mesures ont été calculés pour différentes positions du support 3D selon les formules suivantes:

$$\bar{\Delta} = \frac{1}{N}\sum_{i}^{N}\frac{(D_i^{calc} - D_i^{meas})}{D_i^{meas}} \qquad \bar{\Delta}_{ABS} = \frac{1}{N}\sum_{i}^{N}\frac{|D_i^{calc} - D_i^{meas}|}{D_i^{meas}} \tag{7.4}$$

où K est le nombre de PinPoints utilisés pour les mesures, D_i^{meas} est la dose mesurée pour la chambre i et D_i^{calc} est la dose calculée par le MC. Pour l'évaluation de $\bar{\Delta}$ et $\bar{\Delta}_{ABS}$ le support 3D a été placé dans une région de dose supérieure à 95% de la dose prescrite (région cible). Dans la mesure du possible, une évaluation supplémentaire a été effectuée pour la région du plateau (région proximale), où un niveau de dose compris entre 60% et 95% de la dose a été atteint. Les valeurs de dose mesurées par des chambres situées là où le gradient de dose est supérieure à 0.04 Gy/mm ont été exclues de l'analyse en raison des incertitudes de mesures.

7.4.3 Résultats et discussion

Les paramètres optimaux du modèle de faisceau optique ont permis d'obtenir un taux de réussite de 99% pour l'exigence clinique de 1 mm/10%. Comme prévu, les écarts les plus importants de 1.8 mm (7.2 %) et de 1.7 mm (6.9 %) ont été obtenus pour 62.4 MeV à ISD+20 cm dans les plans vertical et horizontal, respectivement. En fait, la précision du modèle de diffusion multiple de Coulomb est principalement à l'origine de l'accord dans FWHM car la diffusion est l'effet prédominant pour cette énergie et cette position. D'autre part, cette combinaison d'énergie et de position n'est pas cliniquement pertinente en protonthérapie. Si l'on considère un RaShi, un écart systématique par rapport à la taille du spot mesuré a été observé (voir figure 7.7).

En ce qui concerne les profils de dose en profondeur dans l'eau pour la configuration à faisceau ouvert, pour toutes les énergies analysées, la simulation MC a reproduit avec précision la forme des profils de dose en profondeur mesurés dans l'eau (voir figure 7.8-(a)). Les intégrales normalisées au premier point de mesure sont toujours comprises dans les limites de 1% (voir figure 7.8-(b)). On a constaté que les écarts se situaient toujours à moins de 0.2 mm, comme l'indique la figure 7.8-(c). Les écarts absolus dans BPW80 étaient en moyenne de 0.1 mm, ce qui correspond à un écart relatif d'environ 3% (voir figure 7.8-(d)).L'écart absolu maximal observé était de 0.3 mm (6%) à 169.3 MeV. Écarts de R80, R90 et Rp pour les profils de dose en profondeur dans l'eau à ISD-50cm avec RaShi n'ont jamais dépassé 0.35 mm, tandis que les écarts moyens sur la dose intégrée ainsi que les les différences moyennes entre les pics et les plateaux étaient inférieures à 0.4%.

Les différences entre nos données calculées de "puissance d'arrêt moyenne" et de puissance d'arrêt de l'ICRU pour des protons ayant la même plage de projection que R80 à la profondeur de mesure z_{ref} ont atteint 10.4% pour un faisceau mono-énergétique, avec un comportement dépendant de l'énergie attendu. En effet, les données de puissance d'arrêt de l'ICRU sont fournies pour les faisceaux mono-énergétiques, tandis que la "puissance d'arrêt moyenne" doit tenir compte de la

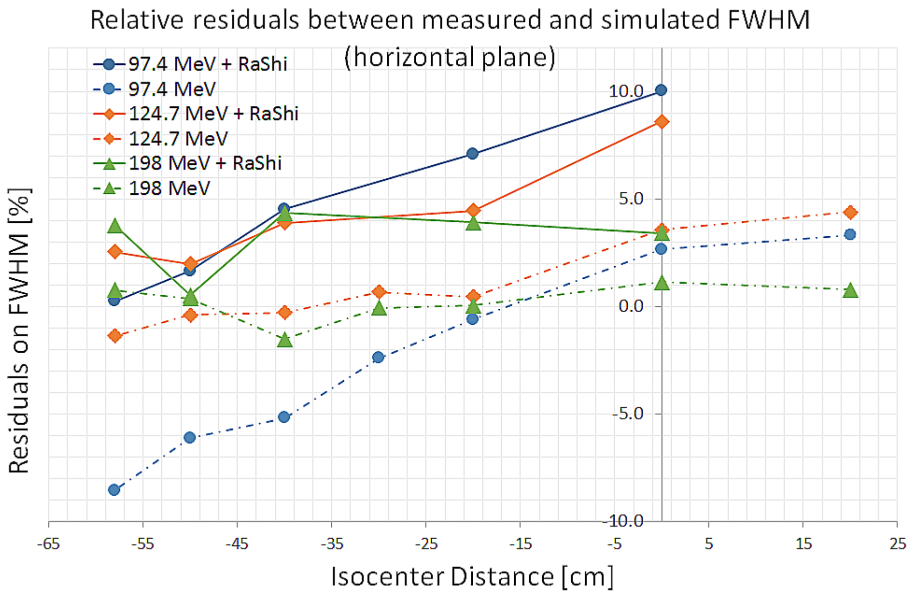

Figure 7.7: FWHM accord en termes relatifs entre les valeurs simulées et les valeurs mesurées avec et sans RaShi pour le plan horizontal. Par souci de clarté, seules trois énergies représentatives sont indiquées. Des résultats similaires ont été obtenus pour le plan vertical.

perte de protons primaires ainsi que des secondaires nucléaires à la profondeur de mesure qui est obtenue par simulation MC. L'accord avec le profil de dose transversale mesuré était généralement meilleur que 0.4 mm. Le FS50 et le LP80-20 se sont mis d'accord en moyenne de 0.4 mm et -0.1 mm, respectivement. Pour le FS50, un écart maximal de -1.0 mm (-11.4% en termes relatifs) a été observé pour la cible la moins profonde (niveau de dose de 95% entre 3 et 8 cm) lorsque le RaShi était utilisés. Les écarts pour R80 et R90, initialement trouvés jamais supérieurs à 0.2 mm, augmentent jusqu'à 0.2 mm à 0.5 mm et 0.7 mm respectivement lorsqu'un RaShi a été utilisé. Un écart de 1.3 mm a été constaté dans l'évaluation du MOD90 sur toutes les boîtes, avec une déviation maximale de 2.1 mm pour la cible la plus profonde (niveau de dose de 95% entre 22 et 30 cm). Le DP80-20 était de -0.3 mm en moyenne avec une déviation maximale de -0.6 mm. L'évaluation en termes de paramètres distaux et latéraux est résumée dans le tableau suivant 7.2.

Après une correction systématique de la calibration en dose absolue du système de -2.7%, l'écart le plus important était de -1.2% à la position proximale de la box10 (voir figure 7.9).

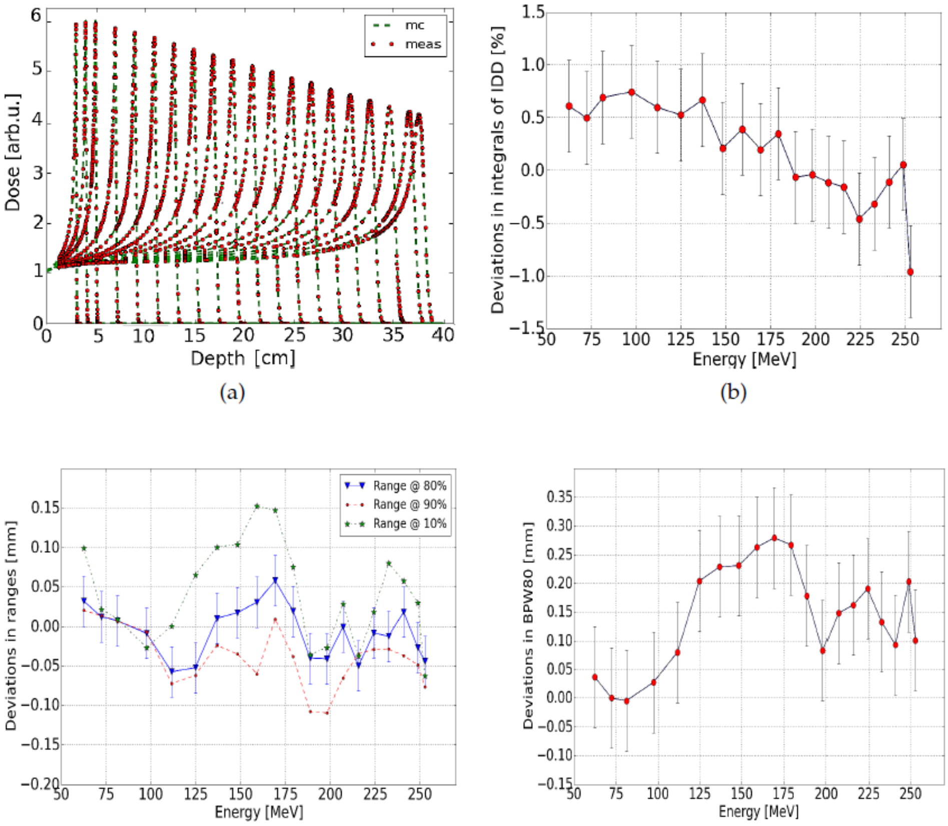

(a) (b)

(c) (d)

Figure 7.8: Dans la figure 7.8-(a), les profils de dose en profondeur simulés dans l'eau comparés aux profils mesurés pour 20 les énergies sont montrées. Pour cette comparaison, les valeurs d'énergie déposées dans le volume cylindrique représentant la chambre du pic de Bragg d'un rayon de 4.08 cm a été utilisée. Dans la figure 7.8-(b), écarts relatifs entre les doses intégrales simulées et mesurées sont indiquées. Dans la figure 7.8-(c), écarts absolus entre les plages simulées et mesurées sont indiquées alors que dans la figure 7.8-(d), les écarts absolus de Des valeurs de largeur de pic de Bragg à un niveau de dose de 80% sont rapportes. Les barres d'erreur correspondent toujours à l'indication écart type. Par souci de clarté, dans la figure 7.8-(c), les barres d'erreur ne sont rapportées que pour un seul ensemble.

Box type	FS50 [mm]	LP80-20- [mm]	LP80-20+ [mm]
Box6(0,0,6)	0.3 (0.4%)	-1.0 (-11.4%)	0.0 (0.1%)
Box8(0,0,15)	0.3 (0.3%)	-0.2 (-2.4%)	-0.2 (-2.0%)
Box10(0,0,25)	0.1 (0.1%)	0.3 (1.1%)	0.2 (2.1%)
Box6(0,0,5) ISD-50cm+RaShi	1.0 (1.2%)	-0.4 (10.3%)	0.2 (-2.4%)

Box type	R80 [mm] (%)	R90 [mm] (%)	Rp [mm] (%)	MOD90 [mm] (%)	DP80-20 [mm] (%)
Box6(0,0,6)	0.0 (0.0%)	0.1 (0.0%)	-0.7 (-0.7%)	-1.0 (-1.5%)	-0.6 (-24.7%)
Box8(0,0,15)	0.0 (0.0%)	0.0 (0.0%)	-0.4 (-0.2%)	1.3 (1.4%)	-0.5 (-14.0%)
Box10(0,0,25)	-0.1 (0.0%)	-0.2 (-0.1%)	-0.4 (-0.1%)	2.1 (1.7%)	-0.5 (-9.0%)
Box6(0,0,5) ISD-50cm+RaShi	0.5 (0.6%)	0.7 (0.9%)	-0.2 (-0.2%)	0.8 (1.3%)	-0.5 (-16.0%)

Table 7.2: déviations dans l'eau pour les distributions de dose 3D analysées en termes de paramètres transversaux (ci-dessus) et de paramètres distaux (ci-dessous) en termes absolus et relatifs. Le LP80-20- et le LP80-20+ se réfèrent au LP80-20 évalué pour de chaque côtédu centre du profil de dose transversal.

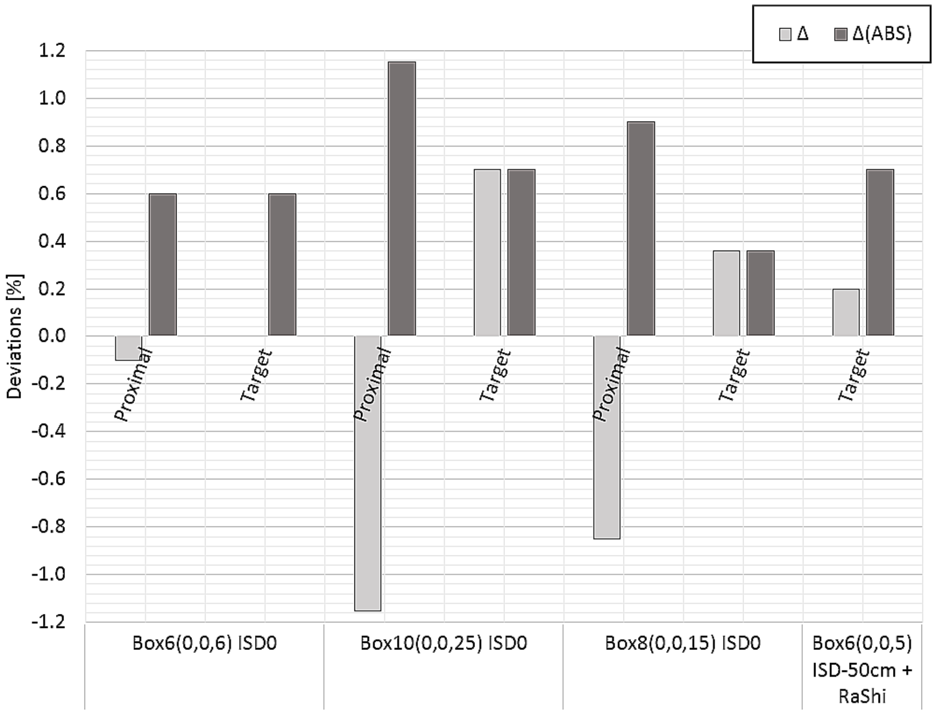

Figure 7.9: Écarts de dose locaux selon les èquations 7.4 après redimensionnement de -2.7 %.

La précision du modèle de faisceau n'a pas été affectée par les différents intervalles d'air ou l'utilisation du RaShi, qui sont connu pour être des situations complexes pour les algorithmes classiques de type *pencil beam*. Un écart maximal de -0.2% a été constaté dans le SOBP pour la box6 non isocentrique avec RaShi. Tous les cas tridimensionnels analysés sont illustrés dans les figures 7.10 et 7.11.

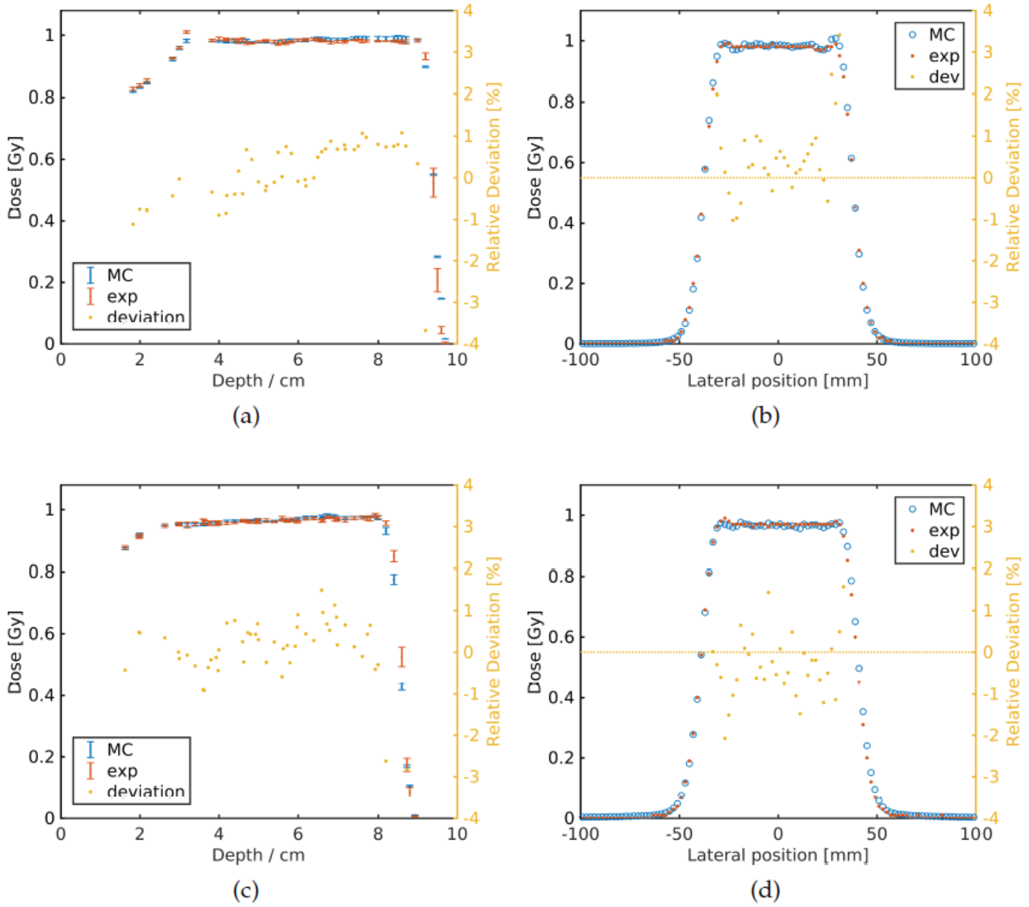

Figure 7.10: Profils de dose longitudinaux (a) et transversaux (b) pour les profils de dose Box6(0,0,6) et longitudinaux (c) et transversaux (d) pour le Box6(0,0,5) placés à la ISD-50cm avec RaShi comparé aux données mesurées.

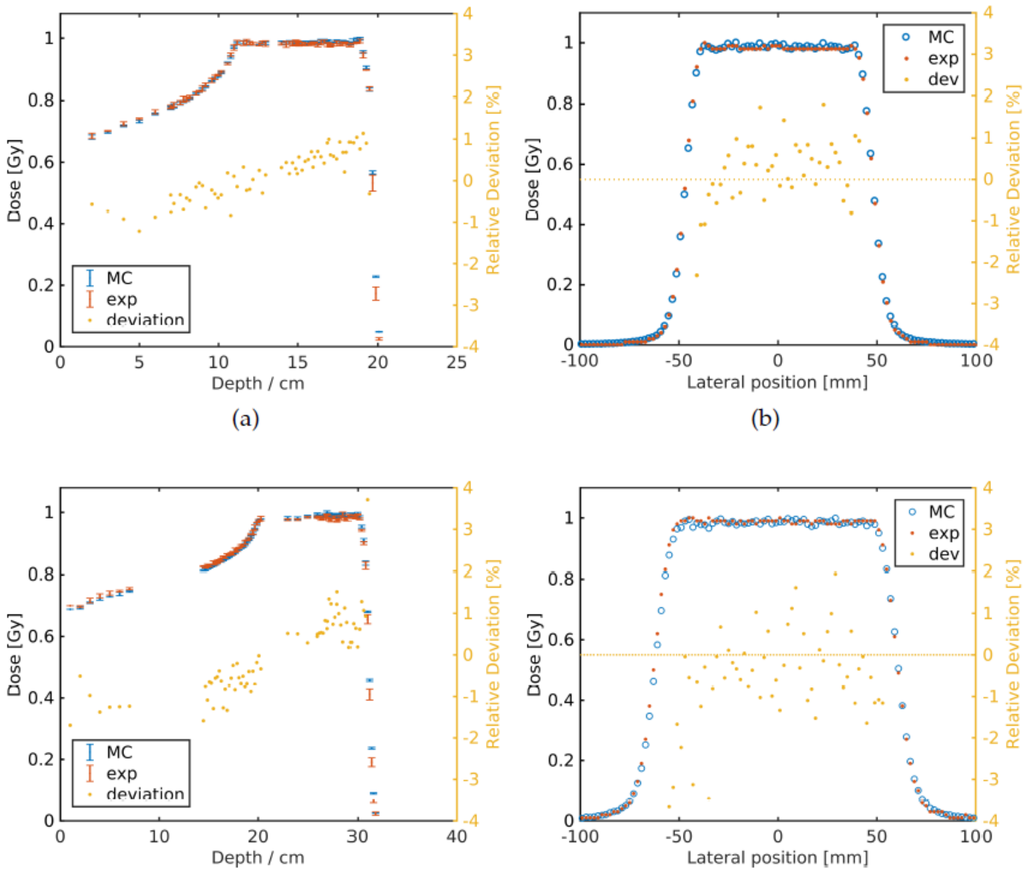

(a) (b)

(c) (d)

Figure 7.11: Profils de dose longitudinaux (a) et transversaux (b) pour les profils de dose Box8(0,0,15) et longitudinaux (c) et transversaux (d) pour le Box10(0,0,25) comparativement aux données mesurées.

7.5 Vers la mise en œuvre de GATE pour le calcul de dose indépendant

La caractérisation des propriétés physiques du faisceau de protons représente la toute première étape vers la mise en œuvre d'un ≪ *independent dose calculation tool* ≫ (IDC). Après validation, il est important d'aller vers plus de cas cliniques, afin de repérer les capacités et les limites du modèle proposé dans un contexte plus clinique. En fin de compte, l'IDC doit être correctement intégré dans le flux de travail clinique. Par exemple, l'IDC devrait être interfacé avec le système de planification de traitement (TPS) afin de pouvoir échanger facilement toutes les informations nécessaires sur les patients en termes de fichiers DICOM. A cet égard, le flux de travail (workflow) entre le TPS utilisé cliniquement et le moteur de calcul de dose

GATE MC basé sur Geant4 est présenté dans ce chapitre. Un aperçu de l'assurance de la qualité spécifique au patient (PSQA) effectuée à MedAustron est d'abord présenté. De nombreux détails concernant la spécification dosimétrique et/ou la calibration des détecteurs sont présentés dans [151, 144]. Les détails concernant la mise en service de l'équipement sont disponibles dans [143].Actuellement, malgré le temps de faisceau nécessaire pour la vérification directe des plans de traitement, le protocole PSQA est la seule possibilité de vérifier que le traitement prévu peut être délivré dans les tolérances cliniques. Toutefois, les mesures PSQA effectuées dans l'eau ne peuvent fournir aucune donnée concernant l'exactitude de la dose dans le patient. À cet égard, les PSQA peut être considérée comme un modèle simplifié de l'état clinique. L'implémentation d'un IDC dans le flux de travail clinique nécessite une validation minutieuse de chaque étape qui caractérise le flux de travail déjà mentionné. Un IDC correctement mis en œuvre doit être en mesure de fournir une estimation de dose avec au moins la même précision que celle offerte par le TPS. A MedAustron, le bloc détecteur 3D PTW équipé de 24 PinPoint est implémenté pour PSQA selon l'expérience partagée de GSI, HIT et CNAO [151, 165].

7.5.1 Le concept de « workflow »

Le concept du flux de travail utilisé pour reproduire la vérification PSQA avec GATE est représenté dans la figure 7.12.

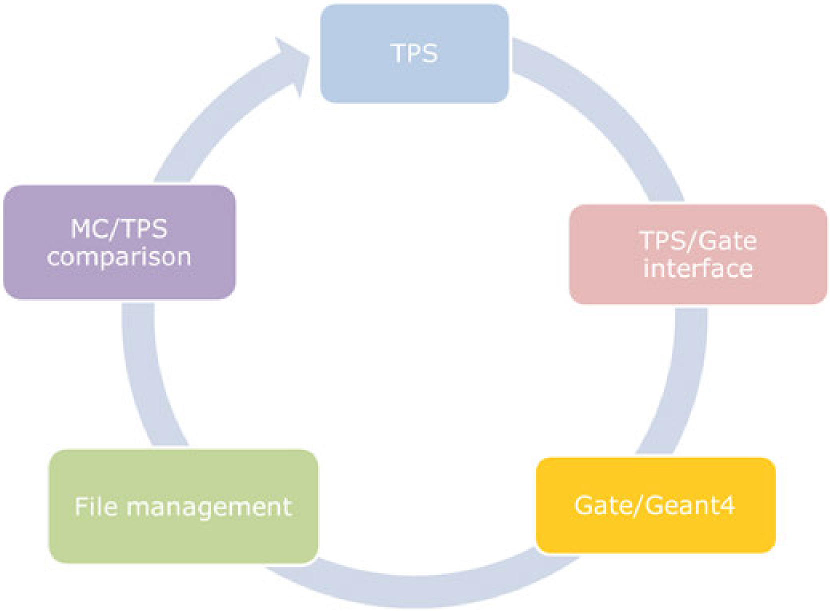

Figure 7.12: un ensemble d'étapes de base nécessaires au calcul complet d'un plan de traitement à l'aide de GATE.

Clinical case	$\bar{\Delta}^{TPS}_{ABS} \pm s_m(\bar{\Delta}^{TPS}_{ABS})$	$\bar{\Delta}^{MC}_{ABS} \pm s_m(\bar{\Delta}^{MC}_{ABS})$
CNS	1.4%±1.5%	1.1%±1.2%
Para-nasal	1.2%±1.0%	1.3%±1.0%
Prostate	1.1%±1.3%	1.0%±0.8%
Para-nasal-RaShi	1.6%±1.0%	1.6%±0.8%

Clinical case	$\bar{\Delta}^{TPS} \pm s_m(\bar{\Delta}^{TPS})$	$\bar{\Delta}^{MC} \pm s_m(\bar{\Delta}^{MC})$
CNS	-0.5%±2%	0.2%±1.7%
Para-nasal	-0.6%±1.5%	-0.6%±1.5%
Prostate	0.8%±1.5%	-0.4%±1.2%
Para-nasal-RaShi	-1.6%±1.1%	-1.5%±1.1%

Table 7.3: effectuée pour les 4 cas pour les valeurs TPS et MC, respectivement.

Le flux de travail de la figure 7.12 est une description de haut niveau. Chaque étape du workflow s'appuie sur plusieurs sous-processus qui sont caractérisés et mis en œuvre à MedAustron dans le cadre de cette thèse.

Le concept de workflow s'applique à la procédure PSQA. Une fois que l'ensemble des positions et des valeurs de dose pour chaque PinPoint est stocké dans un fichier dédié pour effectuer la mesure, le physicien médical peut décider de reproduire la vérification avec l'IDC et de commencer par la première étape du workflow. Dans ce cas, le plan d'AQ calculé au TPS est exporté au format DICOM contenant toutes les informations nécessaires pour reproduire dans GATE le PSQA pour ce cas clinique spécifique. Un *tool* automatisé développé en interne dans le cadre de ce projet de thèse guide l'utilisateur à chaque étape du workflow, en prenant soin de convertir les informations requises dans un format qui peut être traité par la source GATE TPS [134]. En particulier, l'outil exploite plusieurs routines disponibles avec le package CLITK et effectuer une conversion du fichier DICOM en un format lisible par GATE (fichier ASCII par exemple). Les fichiers de sortie convertis par CLITK sont fournis dans un format spécifique géré par GATE.

7.5.2 Résultats et discussion

Dans l'ensemble, pour tous les cas analysés, les résultats de GATE correspondent aux données mesurées et résumées dans le tableau 7.3. Dans la plupart des cas analysés, la tendance des mesures TPS et des mesures GATE était très similaire.. Des résultats similaires ont été obtenus avec le TPS, indépendamment du cas clinique ou de l'algorithme de dose choisi au TPS. L'écart local maximal de dose a été observé dans le cas de la prostate pour le TPS (8,7%) et dans le cas du SNC pour GATE (8,0%). Malgré le filtrage appliqué à l'ensemble des données en termes de gradient

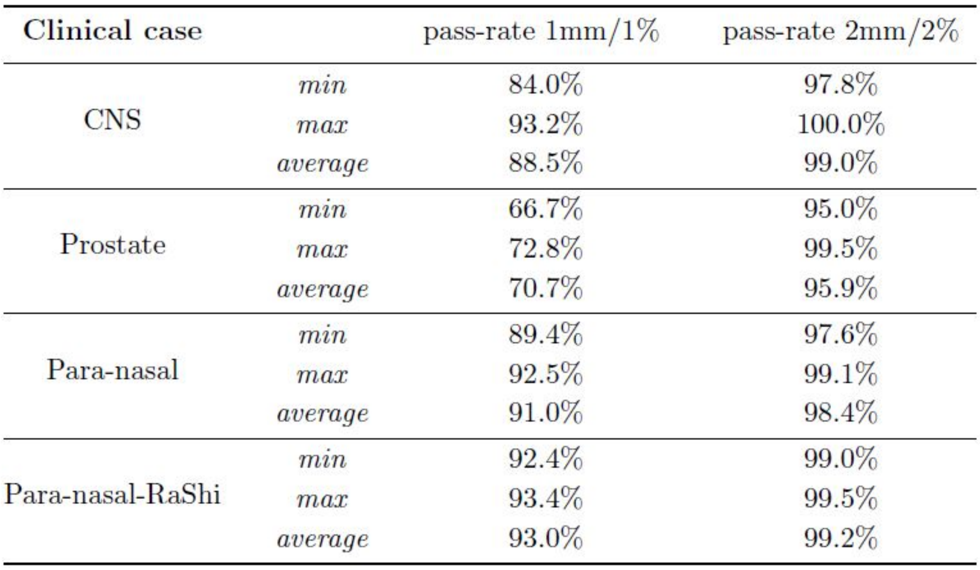

Clinical case		pass-rate 1mm/1%	pass-rate 2mm/2%
CNS	*min*	84.0%	97.8%
	max	93.2%	100.0%
	average	88.5%	99.0%
Prostate	*min*	66.7%	95.0%
	max	72.8%	99.5%
	average	70.7%	95.9%
Para-nasal	*min*	89.4%	97.6%
	max	92.5%	99.1%
	average	91.0%	98.4%
Para-nasal-RaShi	*min*	92.4%	99.0%
	max	93.4%	99.5%
	average	93.0%	99.2%

Table 7.4: l'analyse γ-*index* effectuée pour chaque distribution de dose calculée par le TPS et GATE.

de dose et de faible dose permise, une valeur aberrante (outlier) d'environ -14% a été trouvée dans le cas du SNC pour la prévision du TPS. Une situation similaire a été constatée pour les deux moteurs de dose dans le cas du traitement para-nasal.

L'analyse de l'indice gamma (γ-index) effectuée sur les distributions GATE et TPS est résumée dans le tableau 7.4. Dans l'ensemble, un taux de réussite de 85.7% et 98.1% à 1 mm/1% et 2 mm/2%, respectivement, a été obtenu. Les résultats obtenus ont montré des écarts plus élevés en comparant le GATE et le TPS dans le cas de la prostata.

7.6 Conclusion

Cette thèse de doctorat présente un aperçu des traitements de protonthérapie, en mettant l'accent sur l'importance de la simulation de Monte-Carlo pour le calcul indépendant de la dose (IDC). Sur base des spécifications de l'accélérateur de MedAustron, une modélisation Monte-Carlo détaillée des propriétés physiques du faisceau de protons a été proposée et évaluée. Le modèle de faisceau présenté tient compte de la conception de la nozzle complète, ce qui signifie que la source est décrite à l'entrée de la *nozzle*. Ce choix, représente une différence significative avec la littérature actuelle, où une méthode de modélisation à partir de la sortie de la nozzle est généralement exploitée.

La pratique clinique actuelle de MedAustron exigeait qu'une attention particulière soit accordée à la validation dans des traitements pour desconditions non isocentriques, ce qui est une pratique clinique plutôt rare. La configuration non isocentrique augmente la complexité du traitement et est une caractéristique unique de MedAustron. La précision dosimétrique obtenue par le modèle de faisceau a atteint un écart maximal de -0.2% dans le SOBP par rapport aux données mesurées pour la boîte non isocentrique6 avec RaShi, tandis que l'écart maximal de -1.2% a été observé à la position proximale de la box10.

La calibration du modèle de faisceau en dose absolue représente un autre sujet clé. Dans ce travail, nous présentons la mise en œuvre de la calibration du modèle de faisceau en condition de référence à l'aide d'un formalisme nouvellement développé basé sur les mesures du produit dose-surface (DAP). A notre connaissance, il s'agit de la première mise en œuvre du formalisme DAP dans la pratique clinique.

Ce travail a été soumise pour publication dans une étude dédiée intitulée "A reference Monte Carlo beam model of the MedAustron proton horizontal fixed beam line using GATE/Geant4". En l'état actuel du projet, un programme de vérification de GATE prenant en compte des cas plus complexes tels que les fantômes hétérogènes et l'impact de l'incidence oblique de l'irradiation du faisceau représente une perspective future.

Enfin et surtout, pour entrer dans la routine clinique, une validation approfondie des courbes de calibration du scanner est nécessaire. Il s'agit de la dernière étape pour permettre le calcul complet du plan de MC qui sera inséré dans le flux de travail clinique de MedAustron. A cet égard, un nouveau projet a récemment été démarré à MedAustron, en utilisant comme point de départ l'analyse et les résultats obtenus pendant ce doctorat.

Acronyms

- BPw: Bragg Peak width
- CAXDD: Central Axis Depth Dose
- CNAO: Centro Nazionale di Adroterapia Oncologica
- CSDA: Continuos Slowing-Down Approxiamtion
- DDS: Dose Delivery System
- DP: Distal Penumbra
- DSB: Duble Strand Breaks
- FS: Field Size
- FWHM: Full Width at Half Maximum
- GSI: Gesellschaft für Schwerionenforschung
- HEBT: High Enegry Beam Trasport
- HIT: Heidelberg Ionenstrahl Therapy
- HU: Hounsfield Unit
- IDC: Independent Dose Calculation
- IDD: Integrated Depth Dose
- IMRT: Intense Modulated Radio-Therapy
- IR: Irradiation Room
- LEBT: Low Energy Beam Trasport
- LET: Linear Energy Transfer
- LIBT: Light Ion Beam Therapy
- LP: Lateral Penumbra
- MAPTA: MedAustron Particle Therapy Accelerator
- MAPTS: MedAustron Partcle Therapy System
- MAPTS: MedAustron Particle Therapy System
- MC: Monte Carlo
- MCS: Multiple Columb Scattering

- MEBT: Medium Energy Beam Trasport
- MIT: Marburg Ionenstrahl Therapy
- NCR: Non Clinical Research
- OAR: Organ At Risk
- OER: Oxigen Enhancement Ratio
- OIS: Oncology Information System
- PAS: Patient Alignment System
- PBP: Pristine Bragg Peak
- PSQA: Patient Specific Quality Assurance
- PSR: Patient Study Record
- RBE: Relative Biological Effectiveness
- RTSS: Radiotherapy System
- RX: range at the X% dose level in the distal fall-off of a depth dose profile
- SAD: Source to Axis Distance
- SOBP: Spread Out Bragg Peak
- SSB: Single Strand Breaks
- TFL: Treatment Field Lenght
- TOED: Treatement Operation Editor
- TPS: Treatment Planning System
- VOI: Volume Of Interest
- WEPL: Water Equivalent Path Length

Acknowledgments

I would like to thank all the people which have taken part, directly or indirectly, at this four-year project. In particular, I would like to express my sincere gratitude to my supervisor Dr. Loïc Grevillot. Without his precious contribution, none of this would have been possible. A special thank to Dr. David Sarrut, whom continuously advised the project with his experience. I would also like to express my gratitude to every MedAustron colleague, especially to the whole Medical Physics group. I could not wish a better mixture of expertise and colleges.

Bibliography

[1] Vos, T., Allen, C., Arora, M., Barber, R. M., Bhutta, Z. A., Brown, A., ... and Coggeshall, M. (2016). Global, regional, and national incidence, prevalence, and years lived with disability for 310 diseases and injuries, 1990–2015: a systematic analysis for the Global Burden of Disease Study 2015. *The Lancet*, 388(10053), 1545-1602.

[2] World Cancer Report 2014. *World Health Organization.* (2014). ISBN 9283204298.

[3] Wang, H., Naghavi, M., Allen, C., Barber, R. M., Carter, A., Casey, D. C., ... and Dandona, L. (2016). Global, regional, and national life expectancy, all-cause mortality, and cause-specific mortality for 249 causes of death, 1980–2015: a systematic analysis for the Global Burden of Disease Study 2015. *The Lancet*, 388(10053), 1459-1544.

[4] ”Statistik Austria: Die informationsmanager”. https://www.statistik.at. Retrieved 2017-10-26.

[5] World Health Organization: WHO. Management of Substance Abuse Unit. Global status report on alcohol and health, 2014.

[6] Cho, Y. S., and Ryu, K. H. (2014, May). Predictive pattern analysis using SOM in medical data sets for medical treatment service. *In Computational Intelligence in Bioinformatics and Computational Biology, 2014 IEEE Conference on* (pp. 1-5). IEEE.

[7] Moyers, M. F., and Vatnitsky, S. M. (2012). Practical implementation of light ion beam treatments. *Medical Physics Publishing.*

[8] Paganetti, H. (Ed.). (2016). Proton therapy physics. *CRC press.*

[9] Wilson, R. R. (1946). Radiological use of fast protons. *Radiology*, 47(5), 487-491.

[10] Bragg, W. H., and Kleeman, R. (1905). XXXIX. On the α particles of radium, and their loss of range in passing through various atoms and molecules. *The London, Edinburgh, and Dublin Philosophical Magazine and Journal of Science*, 10(57), 318-340.

[11] Lawrence, J. H. (1957). Proton irradiation of the pituitary. *Cancer*, 10(4), 795-798.

[12] Larsson, B., Leksell, L., Rexed, B., and Sourander, P. (1959). Effect of high energy protons on the spinal cord. *Acta radiologica*, 51(1), 52-64.

[13] Larsson, B. (1961). Pre-therapeutic physical experiments with high energy protons. *The British journal of radiology*, 34(399), 143-151.

[14] Falkmer, S., Fors, B., Larsson, B., Lindell, A., Naeslund, J., and Sténson, S. (1962). Pilot study on proton irradiation of human carcinoma. *Acta Radiologica*, 58(1), 33-51.

[15] Larsson, B., Leksell, L., and Rexed, B. (1963). The use of high energy protons for cerebral surgery in man. *Acta Chirurgica Scandinavica* (Sweden), 125.

[16] Kjellberg, R. N., Sweet, W. H., Preston, W. M., and Koehler, A. M. (1962). The Bragg peak of a proton beam in intracranial therapy of tumors. *Transactions of the American Neurological Association* (US), 87.

[17] Kjellberg, R. N., Koehler, A. M., Preston, W. M., and Sweet, W. H. (1962). Stereotaxic instrument for use with the Bragg peak of a proton beam. *Stereotactic and Functional Neurosurgery*, 22(3-5), 183-189.

[18] Koehler, A. M., Schneider, R. J., and Sisterson, J. M. (1977). Flattening of proton dose distributions for large-field radiotherapy. *Medical Physics*, 4(4), 297-301.

[19] Gragoudas, E. S., Goitein, M., Verhey, L., Munzenreider, J., Urie, M., Suit, H., and Koehler, A. (1982). Proton beam irradiation of uveal melanomas: results of $5\frac{1}{2}$-year study. *Archives of ophthalmology*, 100(6), 928-934.

[20] Wilson, R. (2017). A brief history of the Harvard University cyclotrons.

[21] Jermann, M. (2015). Particle therapy statistics in 2014. *International Journal of Particle Therapy*, 2(1), 50-54.

[22] Dzhelepov, V. P., Komarov, V. I., and Savchenko, O. V. (1969). Development of a proton beam synchrocyclotron with energy from 100 to 200MeV for medico-biological research. *Meditsinskaia radiologiia*, 14(4), 54-58.

[23] Khoroshkov, V. S., Barabash, L. Z., Barkhudarian, A. V., Gol'din, L. L., Lomanov, M. F., Pliashkevich, L. N., and Onosovskiĭ, K. K. (1969). A proton beam accelerator ITEF for radiation therapy. *Meditsinskaia radiologiia*, 14(4), 58-62.

[24] Chuvilo, I.V., Goldin, L.L., Khoroshkov, V.S., Blokhin, S.E., Breyev, V.M., Vorontsov, I.A., Ermolayev, V.V., Kleinbock, Y.L., Lomakin, M.I., Lomanov, M.F. and Medved, V.Y., (1984). ITEP synchrotron proton beam in radiotherapy. *International Journal of Radiation Oncology• Biology• Physics*, 10(2), 185-195.

[25] Kanai, T., Kawachi, K., Kumamoto, Y., Ogawa, H., Yamada, T., Matsuzawa, H., and Inada, T. (1980). Spot scanning system for proton radiotherapy. *Medical physics*, 7(4), 365-369.

[26] ”PTCOG: Particle Therapy Co-Operative Group”. Ptcog.web.psi.ch. Retrieved 2017-09-03.

[27] Newhauser, W. D., and Zhang, R. (2015). The physics of proton therapy. *Physics in Medicine & Biology*, 60(8), R155.

[28] Weber, D.C., Wang, H., Cozzi, L., Dipasquale, G., Khan, H.G., Ratib, O., Rouzaud, M., Vees, H., Zaidi, H. and Miralbell, R., (2009). RapidArc, intensity modulated photon and proton techniques for recurrent prostate cancer in previously irradiated patients: a treatment planning comparison study. *Radiation Oncology*, 4(1), 34.

[29] Georg, D., Hopfgartner, J., Gòra, J., Kuess, P., Kragl, G., Berger, D., Hegazy, N., Goldner, G. and Georg, P., (2014). Dosimetric considerations to determine the optimal technique for localized prostate cancer among external photon, proton, or carbon-ion therapy and high-dose-rate or low-dose-rate brachytherapy. *International Journal of Radiation Oncology• Biology• Physics*, 88(3), 715-722.

[30] Blakely, E. A., and Chang, P. Y. (2004). Late effects from hadron therapy. *Radiotherapy and Oncology*, 73, S134-S140.

[31] Athar, B. S., Bednarz, B., Seco, J., Hancox, C., and Paganetti, H. (2010). Comparison of out-of-field photon doses in 6 MV IMRT and neutron doses in proton therapy for adult and pediatric patients. *Physics in Medicine & Biology*, 55(10), 2879.

[32] Yock, T. I., and Tarbell, N. J. (2004). Technology insight: Proton beam radiotherapy for treatment in pediatric brain tumors. *Nature Reviews Clinical Oncology*, 1(2), 97.

[33] Loeffler, J. S., and Durante, M. (2013). Charged particle therapy—optimization, challenges and future directions. *Nature reviews Clinical oncology*, 10(7), 411.

[34] van de Water, T. A., Lomax, A. J., Bijl, H. P., de Jong, M. E., Schilstra, C., Hug, E. B., and Langendijk, J. A. (2011). Potential benefits of scanned intensity-modulated proton therapy versus advanced photon therapy with regard to sparing of the salivary glands in oropharyngeal cancer. *International Journal of Radiation Oncology* Biology* Physics*, 79(4), 1216-1224.

[35] Chan, A. W., and Liebsch, N. J. (2008). Proton radiation therapy for head and neck cancer. *Journal of surgical oncology*, 97(8), 697-700.

[36] Lundkvist, J., Ekman, M., Ericsson, S. R., Jönsson, B., and Glimelius, B. (2005). Proton therapy of cancer: potential clinical advantages and cost-effectiveness. *Acta oncologica*, 44(8), 850-861.

[37] Orecchia, R., Krengli, M., Jereczek-Fossa, B. A., Franzetti, S., and Gerard, J. P. (2004). Clinical and research validity of hadrontherapy with ion beams. *Critical reviews in oncology/hematology*, 51(2), 81-90.

[38] Ramona, M., Ulrike, M., Robert, J., Richard, P., Christian, V., Helmut, E., Kristine, K., Josef, H., Brigitte, H., Robert, H. and Tomas-Henrik, K.A. (2004). Epidemiological aspects of hadron therapy: a prospective nationwide study of the Austrian project MedAustron and the Austrian Society of Radiooncology (OEGRO). *Radiotherapy and Oncology*, 73, S24-S28.

[39] Baron, M. H., Pommier, P., Favrel, V., Truc, G., Balosso, J., and Rochat, J. (2004). A “one-day survey”: as a reliable estimation of the potential recruitment for proton-and carbon-ion therapy in France. *Radiotherapy and Oncology*, 73, S15-S17.

[40] Fuss, M., Poljanc, K., Miller, D. W., Archambeau, J. O., Slater, J. M., Slater, J. D., and Hug, E. B. (2000). Normal tissue complication probability (NTCP) calculations as a means to compare proton and photon plans and evaluation of clinical appropriateness of calculated values. *International journal of cancer*, 90(6), 351-358.

[41] Fuss, M., Hug, E. B., Schaefer, R. A., Nevinny-Stickel, M., Miller, D. W., Slater, J. M., and Slater, J. D. (1999). Proton radiation therapy (PRT) for pediatric optic pathway gliomas: comparison with 3D planned conventional photons and a standard photon technique. *International Journal of Radiation Oncology• Biology• Physics*, 45(5), 1117-1126.

[42] Peeters, A., Grutters, J.P., Pijls-Johannesma, M., Reimoser, S., De Ruysscher, D., Severens, J.L., Joore, M.A. and Lambin, P. (2010). How costly is particle therapy? Cost analysis of external beam radiotherapy with carbon-ions, protons and photons. *Radiotherapy and oncology*, 95(1), 45-53.

[43] Lodge, M., Pijls-Johannesma, M., Stirk, L., Munro, A. J., De Ruysscher, D., and Jefferson, T. (2007). A systematic literature review of the clinical and cost-effectiveness of hadron therapy in cancer. *Radiotherapy and Oncology*, 83(2), 110-122.

[44] Konski, A., Speier, W., Hanlon, A., Beck, J. R., and Pollack, A. (2007). Is Proton Beam Therapy Cost Effective in the Treatment of Adenocarcinoma of the. *Journal of Clinical Oncology*, 25(24), 3603-3608.

[45] Goitein, M., and Jermann, M. (2003). The relative costs of proton and X-ray radiation therapy. *Clinical Oncology*, 15(1), S37-S50.

[46] International Commission of Radiation Units. International Commission on Radiation Units and Measurements: Stopping Power and ranges for protons and alpha particles. Report 24. 1976

[47] Cantone, M.C., Ciocca, M., Dionisi, F., Fossati, P., Lorentini, S., Krengli, M., Molinelli, S., Orecchia, R., Schwarz, M., Veronese, I. and Vitolo, V. (2013). Application of failure mode and effects analysis to treatment planning in scanned proton beam radiotherapy. *Radiation Oncology*, 8(1), 127.

[48] Schaffner, B., Pedroni, E., and Lomax, A. (1999). Dose calculation models for proton treatment planning using a dynamic beam delivery system: an attempt to include density heterogeneity effects in the analytical dose calculation. *Physics in Medicine & Biology*, 44(1), 27.

[49] Soukup, M., Fippel, M., and Alber, M. (2005). A pencil beam algorithm for intensity modulated proton therapy derived from Monte Carlo simulations. *Physics in Medicine & Biology*, 50(21), 5089.

[50] Newhauser, W., Fontenot, J., Zheng, Y., Polf, J., Titt, U., Koch, N., Zhang, X. and Mohan, R. (2007). Monte Carlo simulations for configuring and testing an analytical proton dose-calculation algorithm. *Physics in Medicine & Biology*, 52(15), 4569.

[51] Lomax, A. J. (2008). Intensity modulated proton therapy and its sensitivity to treatment uncertainties 1: the potential effects of calculational uncertainties. *Physics in Medicine & Biology*, 53(4), 1027.

[52] Lomax, A. J. (2008). Intensity modulated proton therapy and its sensitivity to treatment uncertainties 2: the potential effects of inter-fraction and inter-field motions. *Physics in Medicine & Biology*, 53(4), 1043.

[53] Paganetti, H. (2012). Range uncertainties in proton therapy and the role of Monte Carlo simulations. *Physics in Medicine & Biology*, 57(11), R99.

[54] Böhlen, T.T., Cerutti, F., Chin, M.P.W., Fassò, A., Ferrari, A., Ortega, P.G., Mairani, A., Sala, P.R., Smirnov, G. and Vlachoudis, V. (2014). The FLUKA code: developments and challenges for high energy and medical applications. *Nuclear data sheets*, 120, 211-214.

[55] Ferrari, A., Sala, P. R., Fasso, A., and Ranft, J. (2005). FLUKA: A multi-particle transport code (Program version 2005) (No. INFN-TC-05-11).

[56] Agostinelli, S., Allison, J., Amako, K.A., Apostolakis, J., Araujo, H., Arce, P., Asai, M., Axen, D., Banerjee, S., Barrand, G.2. and Behner, F. (2003). GEANT4—a simulation toolkit. Nuclear instruments and methods in physics research section A: Accelerators, Spectrometers, Detectors and Associated Equipment, 506(3), 250-303.

[57] Allison, J., Amako, K., Apostolakis, J.E.A., Araujo, H.A.A.H., Dubois, P.A., Asai, M.A.A.M., Barrand, G.A.B.G., Capra, R.A.C.R., Chauvie, S.A.C.S., Chytracek, R.A.C.R. and Cirrone, G.A.P. (2006). Geant4 developments and applications. *IEEE Transactions on nuclear science*, 53(1), 270-278.

[58] Iwase, H., Niita, K., and Nakamura, T. (2002). Development of general-purpose particle and heavy ion transport Monte Carlo code. *Journal of Nuclear Science and Technology*, 39(11), 1142-1151.

[59] Pelowitz, D.B., Durkee, J.W., Elson, J.S., Fensin, M.L., Hendricks, J.S., James, M.R., Johns, R.C., Mc Kinney, F.W., Mashnik, S.G., Waters, L.S. and Wilcox, T.A. (2011). MCNPX 2.7 E extensions (No. LA-UR-11-01502; LA-UR-11-1502). Los Alamos National Laboratory (LANL).

[60] Waters, L. S. (2002). MCNPX user's manual. Los Alamos National Laboratory.

[61] Testa, M., Schümann, J., Lu, H. M., Shin, J., Faddegon, B., Perl, J., and Paganetti, H. (2013). Experimental validation of the TOPAS Monte Carlo system for passive scattering proton therapy. *Medical physics*, 40(12).

[62] Perl, J., Shin, J., Schümann, J., Faddegon, B., and Paganetti, H. (2012). TOPAS: An innovative proton Monte Carlo platform for research and clinical applications. *Medical physics*, 39(11), 6818-6837.

[63] Sarrut, D., Bardiès, M., Boussion, N., Freud, N., Jan, S., Létang, J.M., Loudos, G., Maigne, L., Marcatili, S., Mauxion, T. and Papadimitroulas, P. (2014). A review of the use and potential of the GATE Monte Carlo simulation code for radiation therapy and dosimetry applications. *Medical physics*, 41(6Part1).

[64] Jan, S., Benoit, D., Becheva, E., Carlier, T., Cassol, F., Descourt, P., Frisson, T., Grevillot, L., Guigues, L., Maigne, L. and Morel, C. (2011). GATE V6: a major enhancement of the GATE simulation platform enabling modelling of CT and radiotherapy. *Physics in Medicine & Biology*, 56(4), 881.

[65] Fippel, M., and Soukup, M. (2004). A Monte Carlo dose calculation algorithm for proton therapy. *Medical physics*, 31(8), 2263-2273.

[66] Mairani, A., Böhlen, T.T., Schiavi, A., Tessonnier, T., Molinelli, S., Brons, S., Battistoni, G., Parodi, K. and Patera, V. (2013). A Monte Carlo-based treatment planning tool for proton therapy. *Physics in Medicine & Biology*, 58(8), 2471.

[67] Böhlen, T.T., Bauer, J., Dosanjh, M., Ferrari, A., Haberer, T., Parodi, K., Patera, V. and Mairani, A. (2013). A Monte Carlo-based treatment-planning tool for ion beam therapy. *Journal of radiation research*, 54(suppl_1), i77-i81.

[68] Molinelli, S., Mairani, A., Mirandola, A., Freixas, G.V., Tessonnier, T., Giordanengo, S., Parodi, K., Ciocca, M. and Orecchia, R. (2013). Dosimetric accuracy assessment of a treatment plan verification system for scanned proton beam radiotherapy: one-year experimental results and Monte Carlo analysis of the involved uncertainties. *Physics in Medicine & Biology*, 58(11), 3837.

[69] Parodi, K., Mairani, A., Brons, S., Hasch, B.G., Sommerer, F., Naumann, J., Jäkel, O., Haberer, T. and Debus, J. (2012). Monte Carlo simulations to support start-up and treatment planning of scanned proton and carbon ion therapy at a synchrotron-based facility. *Physics in Medicine & Biology*, 57(12), 3759.

[70] Souris, K., Lee, J. A., and Sterpin, E. (2016). Fast multipurpose Monte Carlo simulation for proton therapy using multi-and many-core CPU architectures. *Medical physics*, 43(4), 1700-1712.

[71] Schiavi, A., Senzacqua, M., Pioli, S., Mairani, A., Magro, G., Molinelli, S., Ciocca, M., Battistoni, G. and Patera, V., (2017). Fred: a GPU-accelerated fast-Monte Carlo code for rapid treatment plan recalculation in ion beam therapy. *Physics in Medicine & Biology*, 62(18), 7482.

[72] Paganetti, H., Jiang, H., Parodi, K., Slopsema, R., and Engelsman, M. (2008). Clinical implementation of full Monte Carlo dose calculation in proton beam therapy. *Physics in Medicine & Biology*, 53(17), 4825.

[73] Grevillot, L. (2011). Monte Carlo simulation of active scanning proton therapy system with Gate/Geant4: Towards a better patient dose quality assurance (Doctoral dissertation, INSA de Lyon).

[74] Sawakuchi, G.O., Zhu, X.R., Poenisch, F., Suzuki, K., Ciangaru, G., Titt, U., Anand, A., Mohan, R., Gillin, M.T. and Sahoo, N., (2010). Experimental characterization of the low-dose envelope of spot scanning proton beams. *Physics in Medicine & Biology*, 55(12), 3467.

[75] International Commission on Radiation Units and Measurements. (2007). Prescribing, recording, and reporting proton-beam herapy. ICRU Report 78.

[76] Moyers, M. F., Coutrakon, G. B., Ghebremedhin, A., Shahnazi, K., Koss, P., and Sanders, E. (2007). Calibration of a proton beam energy monitor. *Medical physics*, 34(6Part1), 1952-1966.

[77] International Atomic Energy Agency. (2001). Absorbed Dose Determination in External Beam Radiotherapy: An International Code of Practice for Dosimetry Based on Standards of Absorbed Dose to Water. IAEA-TRS 398

[78] International Commission on Radiation Units and Measurements. (1994). Stopping powers and ranges for protons and alpha particles. ICRU Report 49.

[79] Medaustron report DCO22_50233_1401091. Medical Physics terminologies for parameters associated with dose distributions of light ion beams V2.0 (2016-07-01)

[80] Attix, F. H. (2008). Introduction to radiological physics and radiation dosimetry. John Wiley & Sons.

[81] International Commission on Radiation Units and Measurements. (2000). Nuclear Data for Neutron and Proton Radiotherapy and for Radiation Protection. ICRU report 63.

[82] Bohr, N. (1913). II. On the theory of the decrease of velocity of moving electrified particles on passing through matter. *The London, Edinburgh, and Dublin Philosophical Magazine and Journal of Science*, 25(145), 10-31.

[83] ”NIST: National Institute of Standards and Technology”. physics.nist.gov/PhysRefData/Star/Text/PSTAR.html. Retrieved at 2018-06-27

[84] Bethe, H. (1930). Zur theorie des durchgangs schneller korpuskularstrahlen durch materie. *Annalen der Physik*, 397(3), 325-400.

[85] Bloch, F. (1933). Zur bremsung rasch bewegter teilchen beim durchgang durch materie. *Annalen der Physik*, 408(3), 285-320.

[86] Barkas, W. H., Dyer, J. N., and Heckman, H. H. (1963). Resolution of the $\Sigma-$-mass anomaly. *Physical Review Letters*, 11(1), 26.

[87] Betz, H. D. (1972). Charge states and charge-changing cross sections of fast heavy ions penetrating through gaseous and solid media. *Reviews of Modern Physics*, 44(3), 465.

[88] Linz, U., and Alonso, J. (2007). What will it take for laser driven proton accelerators to be applied to tumor therapy?. *Physical Review Special Topics-Accelerators and Beams*, 10(9), 094801.

[89] Janni, J. F. (1982). Energy loss, range, path length, time-of-flight, straggling, multiple scattering, and nuclear interaction probability: In two parts. Part 1. For 63 compounds Part 2. For elements $1\leq Z\leq 92$. *Atomic data and nuclear data tables*, 27(4-5), 341-529.

[90] Moliere, G. (1948). Theory of the scattering of fast charged particles. 2. Repeated and multiple scattering. Z. Naturforsch., 3, 78-97.

[91] Gottschalk, B., Koehler, A. M., Schneider, R. J., Sisterson, J. M., and Wagner, M. S. (1993). Multiple Coulomb scattering of 160 MeV protons. *Nuclear Instruments and Methods in Physics Research Section B: Beam Interactions with Materials and Atoms*, 74(4), 467-490.

[92] Gottschalk, B., Cascio, E. W., Daartz, J., and Wagner, M. S. (2015). On the nuclear halo of a proton pencil beam stopping in water. *Physics in Medicine & Biology*, 60(14), 5627.

[93] Highland, V. L. (1975). Some practical remarks on multiple scattering. *Nuclear Instruments and Methods*, 129(2), 497-499.

[94] Pedroni, E., Scheib, S., Böhringer, T., Coray, A., Grossmann, M., Lin, S., and Lomax, A. (2005). Experimental characterization and physical modelling of the dose distribution of scanned proton pencil beams. *Physics in Medicine & Biology*, 50(3), 541.

[95] Schardt, D., Elsässer, T., and Schulz-Ertner, D. (2010). Heavy-ion tumor therapy: Physical and radiobiological benefits. *Reviews of modern physics*, 82(1), 383.

[96] Grassberger, C., and Paganetti, H. (2011). Elevated LET components in clinical proton beams. *Physics in Medicine & Biology*, 56(20), 6677.

[97] International Atomic Energy Agency. (2008). Relative Biological Effectiveness in Ion Beam Therapy. IAEA-TRS 461

[98] Andreo, P. (2009). On the clinical spatial resolution achievable with protons and heavier charged particle radiotherapy beams. *Physics in Medicine & Biology*, 54(11), N205.

[99] Amaldi, U., and Kraft, G. (2005). Radiotherapy with beams of carbon ions. Reports on progress in physics, 68(8), 1861.

[100] Coggle, J. E., and Bistolfi, F. (1998). Effetti biologici delle radiazioni. Minerva medica.

[101] International Commission on Radiation Units and Measurements. (1999). Recording and Reporting Photon Beam Therapy (Suppl. to ICRU Report 50), ICRU Report 62.

[102] Barendsen, G. W. (1968). Responses of cultured cells, tumors, and normal tissues to radiations of different linear energy transfer. *Health Research Organization* TNO, Rijswijk, Netherlands.

[103] Paganetti, H. (2014). Relative biological effectiveness (RBE) values for proton beam therapy. Variations as a function of biological endpoint, dose, and linear energy transfer. *Physics in Medicine & Biology*, 59(22), R419.

[104] International Atomic Energy Agency. (2006). Dose Reporting in Ion Beam Therapy. IAEA TECDOC-1560.

[105] Scholz, M., Kellerer, A. M., Kraft-Weyrather, W., and Kraft, G. (1997). Computation of cell survival in heavy ion beams for therapy. *Radiation and environmental biophysics*, 36(1), 59-66.

[106] Friedrich, T., Scholz, U., Elsässer, T., Durante, M., and Scholz, M. (2012). Calculation of the biological effects of ion beams based on the microscopic spatial damage distribution pattern. *International journal of radiation biology*, 88(1-2), 103-107.

[107] Elsässer, T., Weyrather, W.K., Friedrich, T., Durante, M., Iancu, G., Krämer, M., Kragl, G., Brons, S., Winter, M., Weber, K.J. and Scholz, M. (2010). Quantification of the relative biological effectiveness for ion beam radiotherapy: direct experimental comparison of proton and carbon ion beams and a novel approach for treatment planning. *International Journal of Radiation Oncology• Biology• Physics*, 78(4), 1177-1183.

[108] Elsässer, T., and Scholz, M. (2007). Cluster effects within the local effect model. *Radiation research*, 167(3), 319-329.

[109] Scholz, M. (2003). Effects of ion radiation on cells and tissues. In Radiation effects on polymers for biological use (pp. 95-155). Springer, Berlin, Heidelberg.

[110] Karger, C. P., and Peschke, P. (2017). RBE and related modeling in carbon-ion therapy. *Physics in Medicine & Biology*, 63(1), 01TR02.

[111] Vatnitsky, S. M., Siebers, J. V., & Miller, D. W. (1996). kQ factors for ionization chamber dosimetry in clinical proton beams. *Medical physics*, 23(1), 25-31.

[112] Medin, J. (2010). Implementation of water calorimetry in a 180 MeV scanned pulsed proton beam including an experimental determination of kQ for a Farmer chamber. *Physics in Medicine & Biology*, 55(12), 3287.

[113] Spencer, L. V., and Attix, F. H. (1955). A theory of cavity ionization. *Radiation Research*, 3(3), 239-254.

[114] Palmans, H., and Verhaegen, F. (2000). On the effective point of measurement of cylindrical ionization chambers for proton beams and other heavy charged particle beams. *Physics in Medicine & Biology*, 45(8), L20.

[115] Stock, M., Georg, P., Mayer, R., Böhlen, T. T., and Vatnitsky, S. (2015). Development of clinical programs for carbon ion beam therapy at MedAustron. *International Journal of Particle Therapy*, 2(3), 474-477.

[116] Nairz, O., Winter, M., Heeg, P., and Jäkel, O. (2013). Accuracy of robotic patient positioners used in ion beam therapy. *Radiation Oncology*, 8(1), 124.

[117] Bryant, P.J., Borri, G., Crescenti, M., Badano, L., Maier, A.T., Weisser, L., Reimoser, S., Pavlovic, M., Knaus, P., Pullia, M. and Benedikt, M. (2000). Proton-Ion Medical Machine Study (PIMMS), 2 (No. CERN-PS-2000-007-DR).

[118] Durante, M., and Loeffler, J. S. (2010). Charged particles in radiation oncology. *Nature reviews Clinical oncology*, 7(1), 37.

[119] Stock, M., Georg, D., Ableitinger, A., Zechner, A., Utz, A., Mumot, M., Kragl, G., Hopfgartner, J., Gora, J., Böhlen, T. and Grevillot, L. (2017). The technological basis for adaptive ion beam therapy at MedAustron: Status and outlook. *Zeitschrift für Medizinische Physik*.

[120] Giordanengo, S., Garella, M.A., Marchetto, F., Bourhaleb, F., Ciocca, M., Mirandola, A., Monaco, V., Hosseini, M.A., Peroni, C., Sacchi, R. and Cirio, R. (2015). The CNAO dose delivery system for modulated scanning ion beam radiotherapy. *Medical Physics*, 42(1), 263-275.

[121] Giordanengo, S., Donetti, M., Garella, M.A., Marchetto, F., Alampi, G., Ansarinejad, A., Monaco, V., Mucchi, M., Pecka, I.A., Peroni, C. and Sacchi, R. (2013). Design and characterization of the beam monitor detectors of the Italian National Center of Oncological Hadron-therapy (CNAO). *Nuclear Instruments and Methods in Physics Research Section A: Accelerators, Spectrometers, Detectors and Associated Equipment*, 698, 202-207.

[122] Grevillot, L., Stock, M., & Vatnitsky, S. (2015). Evaluation of beam delivery and ripple filter design for non-isocentric proton and carbon ion therapy. *Physics in Medicine & Biology*, 60(20), 7985.

[123] Deasy, J. O. (1998). A proton dose calculation algorithm for conformal therapy simulations based on Moliere's theory of lateral deflections. *Medical physics*, 25(4), 476-483.

[124] Clasie, B., Depauw, N., Fransen, M., Gomà, C., Panahandeh, H.R., Seco, J., Flanz, J.B. and Kooy, H.M. (2012). Golden beam data for proton pencil-beam scanning. *Physics in Medicine & Biology*, 57(5), 1147.

[125] Hollmark, M., Uhrdin, J., Belkić, D., Gudowska, I., and Brahme, A. (2004). Influence of multiple scattering and energy loss straggling on the absorbed dose distributions of therapeutic light ion beams: I. Analytical pencil beam model. *Physics in Medicine & Biology*, 49(14), 3247.

[126] Petti, P. L. (1992). Differential-pencil-beam dose calculations for charged particles. *Medical physics*, 19(1), 137-149.

[127] Schaffner, B. (2008). Proton dose calculation based on in-air fluence measurements. *Physics in Medicine & Biology*, 53(6), 1545.

[128] RayStation Manual: RSL-D-RS-6.0-REF-EN-1.0-2016-12-22

[129] Eyges, L. (1948). Multiple scattering with energy loss. *Physical Review*, 74(10), 1534.

[130] Saini, J., Maes, D., Egan, A., Bowen, S.R., St James, S., Janson, M., Wong, T. and Bloch, C. (2017). Dosimetric evaluation of a commercial proton spot scanning Monte-Carlo dose algorithm: comparisons against measurements and simulations. *Physics in Medicine & Biology*, 62(19), 7659.

[131] Palmans, H., and Vatnitsky, S. M. (2016). Beam monitor calibration in scanned light-ion beams. *Medical physics*, 43(11), 5835-5847.

[132] Elia, A., Sarrut, D., Carlino, A., Bohlen, T.T., Fuchs, H., Palmans, H., Resch, A., Letellier, V., Osorio, J., Dreind, R., Stock, M., and Grevillot, L. (2018). A reference Monte Carlo beam model of the MedAustron proton horizontal xed beam line using GATE/Geant4. Submitted to Medical Physics on July 2018.

[133] Tourovsky, A., Lomax, A. J., Schneider, U., and Pedroni, E. (2005). Monte Carlo dose calculations for spot scanned proton therapy. *Physics in Medicine & Biology*, 50(5), 971.

[134] Grevillot, L., Bertrand, D., Dessy, F., Freud, N., and Sarrut, D. (2012). GATE as a GEANT4-based Monte Carlo platform for the evaluation of proton pencil beam scanning treatment plans. *Physics in Medicine & Biology*, 57(13), 4223.

[135] Magro, G., Molinelli, S., Mairani, A., Mirandola, A., Panizza, D., Russo, S., Ferrari, A., Valvo, F., Fossati, P. and Ciocca, M. (2015). Dosimetric accuracy of a treatment planning system for actively scanned proton beams and small target volumes: Monte Carlo and experimental validation. *Physics in Medicine & Biology*, 60(17), 6865.

[136] Grassberger, C., Lomax, A., and Paganetti, H. (2014). Characterizing a proton beam scanning system for Monte Carlo dose calculation in patients. *Physics in Medicine & Biology*, 60(2), 633.

[137] Grevillot, L., Bertrand, D., Dessy, F., Freud, N., and Sarrut, D. (2011). A Monte Carlo pencil beam scanning model for proton treatment plan simulation using GATE/GEANT4. *Physics in Medicine & Biology*, 56(16), 5203.

[138] Testa, M., Schümann, J., Lu, H. M., Shin, J., Faddegon, B., Perl, J., and Paganetti, H. (2013). Experimental validation of the TOPAS Monte Carlo system for passive scattering proton therapy. *Medical physics*, 40(12).

[139] Fracchiolla, F., Lorentini, S., Widesott, L., and Schwarz, M. (2015). Characterization and validation of a Monte Carlo code for independent dose calculation in proton therapy treatments with pencil beam scanning. *Physics in Medicine & Biology*, 60(21), 8601.

[140] Schwaab, J., Brons, S., Fieres, J., and Parodi, K. (2011). Experimental characterization of lateral profiles of scanned proton and carbon ion pencil beams for improved beam models in ion therapy treatment planning. *Physics in Medicine & Biology*, 56(24), 7813.

[141] Paganetti, H. (2006). Monte Carlo calculations for absolute dosimetry to determine machine outputs for proton therapy fields. *Physics in Medicine & Biology*, 51(11), 2801.

[142] Mirandola, A., Molinelli, S., Vilches Freixas, G., Mairani, A., Gallio, E., Panizza, D., Russo, S., Ciocca, M., Donetti, M., Magro, G. and Giordanengo, S.

(2015). Dosimetric commissioning and quality assurance of scanned ion beams at the Italian National Center for Oncological Hadrontherapy. Medical physics, 42(9), 5287-5300.

[143] Grevillot, L., Stock, M., Palmans, H., Osorio Moreno, J., Letellier, V., Dreindl, R., Elia, A., Fuchs, H., Carlino, A. and Vatnitsky, S. (2018). Implementation of dosimetry equipment and phantoms at the MedAustron light ion beam therapy facility. *Medical physics*, 45(1), 352-369.

[144] Carlino, A., Stock, M., Zagler, N., Marrale, M., Osorio, J., Vatnitsky, S., and Palmans, H. (2018). Characterization of PTW-31015 PinPoint ionization chambers in photon and proton beams. Physics in medicine and biology.

[145] Python Software Foundation. Python Language Reference, version 2.7. Available at http://www.python.org

[146] Brun, R., and Rademakers, F. (1997). ROOT—an object oriented data analysis framework. Nuclear Instruments and Methods in Physics Research Section A: Accelerators, Spectrometers, Detectors and Associated Equipment, 389(1-2), 81-86.

[147] Jarlskog, C. Z., and Paganetti, H. (2008). Physics settings for using the Geant4 toolkit in proton therapy. IEEE Transactions on nuclear science, 55(3), 1018-1025.

[148] Hall, D. C., Makarova, A., Paganetti, H., and Gottschalk, B. (2015). Validation of nuclear models in Geant4 using the dose distribution of a 177 MeV proton pencil beam. *Physics in Medicine & Biology*, 61(1), N1.

[149] Grevillot, L., Frisson, T., Zahra, N., Bertrand, D., Stichelbaut, F., Freud, N., and Sarrut, D. (2010). Optimization of GEANT4 settings for proton pencil beam scanning simulations using GATE. *Nuclear Instruments and Methods in Physics Research Section B: Beam interactions with materials and atoms*, 268(20), 3295-3305.

[150] Kurosu, K., Takashina, M., Koizumi, M., Das, I. J., and Moskvin, V. P. (2014). Optimization of GATE and PHITS Monte Carlo code parameters for uniform scanning proton beam based on simulation with FLUKA general-purpose code. *Nuclear Instruments and Methods in Physics Research Section B: Beam Interactions with Materials and Atoms*, 336, 45-54.

[151] Carlino, A. (2017). Implementation of advanced methodologies in the commissioning of a light ion beam therapy facility (Doctoral dissertation, PhD thesis, Department of Physics and Chemistry University of Palermo, Italy).

[152] Ivantchenko, A. V., Ivanchenko, V. N., Molina, J. M. Q., and Incerti, S. L. (2012). Geant4 hadronic physics for space radiation environment. *International journal of radiation biology*, 88(1-2), 171-175.

[153] Ivanchenko, V. N., Kadri, O., Maire, M., and Urban, L. (2010). Geant4 models for simulation of multiple scattering. In Journal of Physics: Conference Series (Vol. 219, No. 3, p. 032045). IOP Publishing.

[154] Urban, L. (2002). Multiple scattering model in Geant4 (No. CERN-OPEN-2002-070).

[155] Fuchs, H., Vatnitsky, S., Stock, M., Georg, D., and Grevillot, L. (2017). Evaluation of GATE/Geant4 multiple Coulomb scattering algorithms for a 160 MeV proton beam. *Nuclear Instruments and Methods in Physics Research Section B: Beam Interactions with Materials and Atoms*, 410, 122-126.

[156] International Commission on Radiation Units and Measurements. (2014). Key data for ionizing-radiation dosimetry: measurement standards and applications. ICRU Report 90.

[157] Laitano, R. F., and Rosetti, M. (2000). Proton stopping powers averaged over beam energy spectra. *Physics in Medicine & Biology*, 45(10), 3025.

[158] Gomà, C., Andreo, P., and Sempau, J. (2016). Monte Carlo calculation of beam quality correction factors in proton beams using detailed simulation of ionization chambers. *Physics in Medicine & Biology*, 61(6), 2389.

[159] International Commission on Radiation Units and Measurements. (2010). Prescribing, recording, and reporting photon-beam intensity-modulated radiation therapy (IMRT). ICRU report 83

[160] Arjomandy, B., Sahoo, N., Ciangaru, G., Zhu, R., Song, X., and Gillin, M. (2010). Verification of patient-specific dose distributions in proton therapy using a commercial two-dimensional ion chamber array. *Medical physics*, 37(11), 5831-5837.

[161] Ciangaru, G., Yang, J. N., Oliver, P. J., Bues, M., Zhu, M., Nakagawa, F., Hitoshi, C., Shin, N., Hirofumi, Y., Mosumi, U., and Smith, A. R. (2007). Verification procedure for isocentric alignment of proton beams. Journal of applied clinical medical physics, 8(4), 65-75.

[162] S.Safai, S.Lin and E.Pedroni Development of an inorganic scintillating mixture for proton beam verication dosimetry *Phys. Med. Biol.* 49, 463755 (2004);

[163] L.Zhao and I.J.Das Gafchromic EBT lm dosimetry in proton beams, *Phys. Med. Biol.* 55 N291301 (2010);

[164] Zhu, X. R., Poenisch, F., Song, X., Johnson, J. L., Ciangaru, G., Taylor, M. B., Ming, F.L., Craig, M., Bijan, A., Andrew, K.L., Seungtaek, C., Quynh, nhu N., Michael, T.G., Narayan, S. and Choi, S. (2011). Patient-specific quality assurance for prostate cancer patients receiving spot scanning proton therapy

using single-field uniform dose. *International Journal of Radiation Oncology* Biology* Physics*, 81(2), 552-559.;

[165] Karger, C. P., Jäkel, O., Hartmann, G. H., and Heeg, P. (1999). A system for three-dimensional dosimetric verification of treatment plans in intensity-modulated radiotherapy with heavy ions. *Medical physics*, 26(10), 2125-2132.

[166] Medaustron report. MP QA Operating Procedure Document: Dosimetrical patient specific plan verification for HBL with protons, issued 13.06.2018.

[167] User Manual PinPoint Chambers Type 31014 - 0.015 cm^3 and Type 31015 - 0.030 cm^3 PinPoint 3D Chamber Type 31016 - 0.016 cm^3 D730.131.00/05 en 2008-10 Chr/Sa

[168] Schneider, U., Pedroni, E., and Lomax, A. (1996). The calibration of CT Hounsfield units for radiotherapy treatment planning. *Physics in Medicine & Biology*, 41(1), 111.

[169] Schneider, W., Bortfeld, T., and Schlegel, W. (2000). Correlation between CT numbers and tissue parameters needed for Monte Carlo simulations of clinical dose distributions. *Physics in Medicine & Biology*, 45(2), 459.

[170] Royston, P. (1992). Approximating the Shapiro-Wilk W-Test for non-normality. Statistics and Computing, 2(3), 117-119.

[171] Royston, P. (1993). A toolkit for testing for non-normality in complete and censored samples. The statistician, 37-43.

[172] Wilcoxon, F. (1945). Individual comparisons by ranking methods. Biometrics bulletin, 1(6), 80-83.

[173] Resch, A.F., Elia, A., Fuchs, H., Carlino, A., Palmans, H., Stock, M., Georg, D. and Grevillot L. (2018). Validation of electromagnetic and nuclear scattering models in GATE/Geant4 for proton therapy. Submitted to PMB on July 2018.

Département FEDORA – INSA Lyon - Ecoles Doctorales – Quinquennal 2016-2020

SIGLE	ECOLE DOCTORALE	NOM ET COORDONNEES DU RESPONSABLE
CHIMIE	**CHIMIE DE LYON** **http://www.edchimie-lyon.fr** Sec : Renée EL MELHEM Bat Blaise Pascal 3^e etage secretariat@edchimie-lyon.fr Insa : R. GOURDON	M. Stéphane DANIELE Institut de Recherches sur la Catalyse et l'Environnement de Lyon IRCELYON-UMR 5256 Équipe CDFA 2 avenue Albert Einstein 69626 Villeurbanne cedex directeur@edchimie-lyon.fr
E.E.A.	**ELECTRONIQUE, ELECTROTECHNIQUE, AUTOMATIQUE** **http://edeea.ec-lyon.fr** Sec : M.C. HAVGOUDOUKIAN Ecole-Doctorale.eea@ec-lyon.fr	M. Gérard SCORLETTI Ecole Centrale de Lyon 36 avenue Guy de Collongue 69134 ECULLY Tél : 04.72.18 60.97 Fax : 04 78 43 37 17 Gerard.scorletti@ec-lyon.fr
E2M2	**EVOLUTION, ECOSYSTEME, MICROBIOLOGIE, MODELISATION** **http://e2m2.universite-lyon.fr** Sec : Sylvie ROBERJOT Bât Atrium - UCB Lyon 1 04.72.44.83.62 Insa : H. CHARLES secretariat.e2m2@univ-lyon1.fr	M. Fabrice CORDEY CNRS UMR 5276 Lab. de géologie de Lyon Université Claude Bernard Lyon 1 Bât Géode 2 rue Raphaël Dubois 69622 VILLEURBANNE Cédex Tél : 06.07.53.89.13 cordey@ univ-lyon1.fr
EDISS	**INTERDISCIPLINAIRE SCIENCES-SANTE** **http://www.ediss-lyon.fr** Sec : Sylvie ROBERJOT Bât Atrium - UCB Lyon 1 04.72.44.83.62 Insa : M. LAGARDE secretariat.ediss@univ-lyon1.fr	Mme Emmanuelle CANET-SOULAS INSERM U1060, CarMeN lab, Univ. Lyon 1 Bâtiment IMBL 11 avenue Jean Capelle INSA de Lyon 696621 Villeurbanne Tél : 04.72.68.49.09 Fax :04 72 68 49 16 Emmanuelle.canet@univ-lyon1.fr
INFOMATHS	**INFORMATIQUE ET MATHEMATIQUES** **http://infomaths.univ-lyon1.fr** Sec :Renée EL MELHEM Bat Blaise Pascal 3^e etage infomaths@univ-lyon1.fr	Mme Sylvie CALABRETTO LIRIS – INSA de Lyon Bat Blaise Pascal 7 avenue Jean Capelle 69622 VILLEURBANNE Cedex Tél : 04.72. 43. 80. 46 Fax 04 72 43 16 87 Sylvie.calabretto@insa-lyon.fr
Matériaux	**MATERIAUX DE LYON** **http://ed34.universite-lyon.fr** Sec : M. LABOUNE PM : 71.70 –Fax : 87.12 Bat. Direction Ed.materiaux@insa-lyon.fr	M. Jean-Yves BUFFIERE INSA de Lyon MATEIS Bâtiment Saint Exupéry 7 avenue Jean Capelle 69621 VILLEURBANNE Cedex Tél : 04.72.43 71.70 Fax 04 72 43 85 28 jean-yves.buffiere@insa-lyon.fr
MEGA	**MECANIQUE, ENERGETIQUE, GENIE CIVIL, ACOUSTIQUE** **http://mega.universite-lyon.fr** Sec : M. LABOUNE PM : 71.70 –Fax : 87.12 Bat. Direction mega@insa-lyon.fr	M. Philippe BOISSE INSA de Lyon Laboratoire LAMCOS Bâtiment Jacquard 25 bis avenue Jean Capelle 69621 VILLEURBANNE Cedex Tél : 04.72 .43.71.70 Fax : 04 72 43 72 37 Philippe.boisse@insa-lyon.fr
ScSo	**ScSo*** **http://recherche.univ-lyon2.fr/scso/** Sec : Viviane POLSINELLI Brigitte DUBOIS Insa : J.Y. TOUSSAINT Tél : 04 78 69 72 76 viviane.polsinelli@univ-lyon2.fr	M. Christian MONTES Université Lyon 2 86 rue Pasteur 69365 LYON Cedex 07 Christian.montes@univ-lyon2.fr

*ScSo : Histoire, Géographie, Aménagement, Urbanisme, Archéologie, Science politique, Sociologie, Anthropologie

FOLIO ADMINISTRATIF

THESE DE L'UNIVERSITE DE LYON OPEREE AU SEIN DE L'INSA LYON

NOM : Elia
DATE de SOUTENANCE : 08/01/2019
(avec précision du nom de jeune fille, le cas échéant)

Prénoms : Alessio

TITRE : Characterization of the GATE Monte Carlo platform for non-isocentric treatments and patient specific treatment plan verification at MedAustron

NATURE : Doctorat
Numéro d'ordre : 2019LYSEI002

Ecole doctorale : N° 160 : ÉLECTRONIQUE, ÉLECTROTECHNIQUE, AUTOMATIQUE

Spécialité : Ingénierie pour le vivant

RESUME : The goal of this PhD is to develop and validate an independent dose calculation method in order to support the intense commissioning work of a Light Ion Beam Therapy (LIBT) facility, and to validate the Treatment Planning System (TPS) dose calculation. The work focuses on proton therapy treatments and is held as a collaboration between the CREATIS laboratory (Lyon, France) and the MedAustron Ion Therapy Center (Wiener Neustadt, Austria).
In this study, the parametrization of the proton pencil beam follows the recommendations provided in Grevillot et al. (2011), but including a full nozzle description. Special care is taken to model the pencil beam properties in non-isocentric conditions, including the use of a Range Shifter (RaShi). In addition, the presented model is calibrated in absolute dose based on a newly formalism in dose-area-product presented in Palmans and Vatnitsky (2016). Eventually, a detailed validation is performed in water, for three-dimensional regular-shaped dose distributions.
The pencil beam optics model reached an accuracy within the clinical requirement of 1mm/10%. Ranges are reproduced within 0.2 and 0.35 mm (max deviation) without and with range shifter, respectively. The dose difference in reference conditions is within 0.5%. The 3D dose delivery validation in water was within 1.2% at maximum. The agreement of distal and longitudinal parameters is mostly better than 1 mm.
The obtained results will be used as a reference for the future clinical implementation of the MedAustron independent dose calculation system. As an example of the potential clinical outcome of the presented work, the patient specific quality assurance measurements performed in water have been successfully reproduced within the clinical requirement of 5% accuracy for a few patients.

MOTS-CLÉS : Monte Carlo, GATE, Proton Therapy, Treatment Verification, Independent Dose Calculation

Laboratoire (s) de recherche : Creatis, IPNL

Directeur de thèse: David Sarrut, Loïc Grevillot

Président de jury :

Composition du jury :

Dietmar Georg, Anders Ahnesjö, Denis Dauvergne, Silvia Molinelli, Carmen Villagrasa